arXiv:hep-ex/0501029 v1 12 Jan 2005

Search for CPT Violation with the FOCUS Experiment and Measurement of Λ_b lifetime in the decay $\Lambda_b \to J/\psi\Lambda$ with the DØ Experiment

Abaz Kryemadhi

Submitted to the faculty of the Graduate School

in partial fulfillment of the requirements

for the degree

Doctor of Philosophy

in the Department of Physics,

Indiana University

December, 2004

Accepted by the Graduate Faculty, Indiana University, in partial fulfillment of the requirements of the degree of Doctor of Philosophy.

Doctoral Committee

Professor Rick Van Kooten
(Chairman)

Professor Alan Kostelecký

Professor Harold Ogren

December 7, 2004

Professor Steven Gottlieb

Copyright © 2005

Abaz Kryemadhi

ALL RIGHTS RESERVED

To God: Who created so much beauty in the universe for us to study.

"The heavens declare the glory of God; the skies proclaim the work of his hands".
Psalm 19:1

Acknowledgments

First of all, my deepest gratitude goes to my advisors, Dr. Rick Van Kooten and Dr. Rob Gardner. Throughout the years of my Ph.D. study, they were always willing to mentor, encourage, and support me. Their expertise and enthusiasm in the field of high energy physics, as well as their unique insightful way of approaching problems, are among the most valuable resources for me.

I would like to thank Dr. Alan Kostelecký for his explanations of the CPT and Lorentz Violation framework and also for his comments and suggestions during the process of publishing the CPT paper, which has been used in this thesis.

I would like to thank Dr. Fred Luehring for his suggestions when I have been at crossroads in my career and his help with some computer software. Along the same lines I would like to thank Thom Sulanke for his help at solving a lot of technical questions.

I would like to thank people from the FOCUS Collaboration, in particular Jim Wiss, Gianluigi Boca, Topher Cowfield, John Link, Eric Vaandering, Kevin Stenson and Harry Cheung for their continual help with any question that I had, and also for their input on making the first part of this thesis possible.

I would like to thank people from the B-Physics group at DØ in particular Vivek Jain, Brad Abbott, Rick Jessik, Guenadi Borisov, Andrei Nomerotski, Sergey Burdin for their continual help with any question that I had, and also for their input on making the second part of this thesis possible.

I would like to thank friends in the Physics Department, Maciej Swat, Prabudha Chakraboty, Jundong Huang and Chunhui Luo for the great physics discussions we have had and also for their friendship.

Finally I would like to thank my beautiful fiancée Ilse Friberg and my parents Avni and Fatmire Kryemadhi for their encouragement and support in the process of making this thesis happen, they have been happy for my achievements and patient with my frustrations.

Abstract

This dissertation describes two different projects from two different experiments. We have performed a search for CPT violation in neutral charm meson oscillations using data from the FOCUS Experiment. While flavor mixing in the charm sector is predicted to be small in the Standard Model, it is still possible to investigate CPT violation through a study of the proper time dependence of a CPT asymmetry in right-sign decay rates for $D^0 \to K^-\pi^+$ and $\bar{D}^0 \to K^+\pi^-$. This asymmetry is related to the CPT violating complex parameter ξ and the mixing parameters x and y: $A_{CPT} \propto \mathrm{Re}\,\xi\, y - \mathrm{Im}\,\xi\, x$. We determine a 95% confidence level limit of $-0.0068 < \mathrm{Re}\,\xi\, y - \mathrm{Im}\,\xi\, x < 0.0234$. Within the framework of the Standard Model Extension incorporating general CPT violation, we also find 95% confidence level limits for the expressions involving coefficients of Lorentz violation of $(-2.8 < N(x,y,\delta)(\Delta a_0 + 0.6\,\Delta a_Z) < 4.8) \times 10^{-16}$ GeV, $(-7.0 < N(x,y,\delta)\Delta a_X < 3.8) \times 10^{-16}$ GeV, and $(-7.0 < N(x,y,\delta)\Delta a_Y < 3.8) \times 10^{-16}$ GeV, where $N(x,y,\delta)$ is a normalization factor that incorporates mixing parameters x, y and the doubly Cabibbo suppressed to Cabibbo favored relative strong phase δ.

We also present measurements of the Λ_b^0 lifetime in the exclusive decay channel $\Lambda_b^0 \to J/\psi\Lambda$ with $J/\psi \to \mu^+\mu^-$ and $\Lambda \to p\pi^-$, the B^0 lifetime in the decay $B_d^0 \to J/\psi K_S^0$ with $J/\psi \to \mu^+\mu^-$ and $K_S^0 \to \pi^+\pi^-$, and the ratio of these lifetimes. The analysis is based on approximately 225 pb^{-1} of data recorded with the DØ detector in $p\bar{p}$ collisions at $\sqrt{s} = 1.96$ TeV. The Λ_b^0 lifetime is determined to be $\tau(\Lambda_b^0) = 1.36 \pm 0.30$ (stat) $\pm$ 0.07(syst) ps, the B^0 lifetime $\tau(B_d) = 1.43 \pm 0.12$ (stat) ± 0.04 (syst) ps, and the ratio $\frac{\tau(\Lambda_b)}{\tau(B_d)} = 0.95 \pm 0.22 \pm 0.05$.

In contrast with previous measurements using semileptonic decays, this is the first determination of the Λ_b^0 lifetime based on a fully reconstructed decay channel.

Contents

Acknowledgments **v**

Abstract **vii**

1 The Standard Model of Particle Physics **1**

1.1 The Fundamental Particles 2

1.2 The Fundamental Forces 2

1.3 Lagrangians 5

2 CPT Formalism **7**

2.1 Mixing Formalism 7

2.2 Proper Time Asymmetry 10

2.3 Double Cabbibo Suppressed Interference 13

2.4 Lorentz Violating Parameters 16

2.5 Sidereal Time 17

2.6 Previous Searches 18

3 The E831/FOCUS Experiment at Fermilab **20**

3.1 Physics Overview 20

3.2 The Accelerator 22

3.3 The Photon Beam 24

3.4 The Spectrometer 26

3.4.1 Tracking 28

3.4.2 Particle Identification 33

3.4.3 Triggers 36

3.5 Data Collection 37

4 Data Analysis **38**

4.1 Analysis Aproach 38

4.2 Analysis Cuts 38

4.3 Results for the Asymmetry 43

4.4 Results for Coefficients of Lorentz Violation 45

4.5 Monte Carlo 48

4.6 Systematic Uncertainties 49

5 Conclusions **52**

6 Introduction to Λ_b^0 **55**

7 Theory Predictions **59**

7.1 Spectator Model 59

7.2 Present Findings 59

7.3 Formalism 61

8 The DØ Detector for Run II **64**

8.1 The DØ Coordinate System 64

8.2 The Run II Accelerator Upgrade 66

8.3 Silicon Microvertex Tracker (SMT) 67

8.4 Outer Tracker: Central Scintillating Fiber Tracker (CFT) 71

8.5 Calorimeters and Preshower Detectors 73

8.6 Muon Systems 75

8.6.1 Central Muon System Drift Chambers 81

8.6.2 Central Muon System Scintillation Counters 83

8.6.3 Forward Muon System Drift Tubes 85

8.6.4 Forward Muon System Scintillation Counters 86

8.6.5 Shielding 87

8.7 Trigger 87

8.7.1 Trigger Level-1 88

8.7.2 Trigger Level-2 90

8.7.3 Trigger Level-3 92

8.7.4 B Triggers with DØ 93

8.8 Data Acquisition 94

9 Establishing the Λ_b^0 Signal **95**

9.1 Data and Monte Carlo Event Samples 95

9.1.1 Dimuon data sample 95

9.1.2 Primary vertex reconstruction 96

9.1.3 Secondary vertex reconstruction 96

9.1.4 Λ_b^0 Candidate Selection 97

9.1.5 Monte Carlo event samples 111

9.1.6 MC Signal $\Lambda_b^0 \to J/\psi\Lambda$ 111

9.2 B_d^0 Event Selections 112

10 Λ_b^0 and B_d Lifetime Measurement **123**

10.1 Proper Decay Length 123

10.1.1 Proper Decay Time Distributions 123

10.2 Fitting Procedure for Λ_b^0 124

10.3 Fitting Procedure for B_d 127

10.4 Systematic Errors for Λ_b and B_d Lifetime 129

11 Discussion and Conclusion **135**

11.1 Summary on Establishing the Λ_b^0 Signal 135

11.2 Summary of Preliminary Lifetimes 135

A Further Details on Systematics Error Determination **137**

References **141**

List of Tables

1.1 Properties of the quarks 3

1.2 Properties of the leptons 3

1.3 Properties of the gauge bosons 4

3.1 Properties of the three FOCUS Čerenkov detectors 34

4.1 Summary of Yields 42

4.2 Contributions to the systematic uncertainty. 51

10.1 Unbinned maximum likelihood fitting results for the Λ_b^0 signal. 126

10.2 Unbinned maximum likelihood fitting results for the B_d^0 signal. 128

10.3 Summary of systematic uncertainties in the measurement of $c\tau$ for Λ_b^0 and B_d and their ratio. The total uncertainties are also given combining the individual uncertainties in quadrature. 130

List of Figures

2.1 (a) Proper time decay probabilities for D^0 decay, right-sign (solid) and wrong-sign (dashed) and (b) A_{CPT} with Re $\xi = 5\%$, Im $\xi = 5\%$. (c) A_{CPT} with Re $\xi = 0$, Im $\xi = 5\%$. (d) A_{CPT} with Re $\xi = 5\%$, Im $\xi = 0$. 13

3.1 The FOCUS D meson signal in three different final states 21

3.2 A schematic of the layout of the Fermilab accelerator complex 23

3.3 Generating the high energy photon beam used by FOCUS 25

3.4 The FOCUS spectrometer 27

3.5 A rough sketch of the different PWC views 30

4.1 Invariant mass distribution for the sum of D^0 and $\overline{D}^0$ right-sign decay candidates. 40

4.2 Invariant mass of (a) $D^0 \to K^-\pi^+$ and (b) $\bar{D}^0 \to K^+\pi^-$ for data (points) fitted with a Gaussian signal and quadratic background (solid line). The vertical dashed lines indicate the signal region, and the vertical dotted lines indicate the sideband region. 41

4.3 (Left) z position of the primary vertex of D's for $runnumber > 9750$ and (right) z position of D's secondary vertices for $runnumber > 9750$. The dashed line is to guide the eye. 42

4.4 Background subtracted reduced proper time distributions for D^0 and $\bar{D}^0$. . 43

4.5 $\frac{S}{B}$ in bins of reduced proper time for $\bar{D}^0$ (left) and D^0 (right). 44

4.6 (a) The ratio of the corrections, and (b) A_{CPT} as a function of reduced proper time. The data points represent the A_{CPT} as given in Eq. 4.1 and the solid line represent the fit given in functional form by Eq. 2.22: (c) $\mathrm{Re}\,\xi$ as a function of Greenwich Mean Sidereal Time (GMST). 46

4.7 $f(t')$ corrections and their ratio for D^0 and $\bar{D}^0$. 49

4.8 Asymmetry in Monte Carlo fitted with Eq. 2.22 50

6.1 World averages of b hadron lifetimes compared to older theoretical predictions (yellow or dark grey bands). 56

6.2 World averages of b hadron lifetimes compared to more recent theoretical predictions (yellow or dark grey bands). 57

6.3 Feynman diagram for the decay $\Lambda_b^0 \to J/\psi\Lambda$. 58

8.1 Elevation view of the upgraded DØ detector. 65

8.2 DØ silicon detector. The figure shows the configuration of the 6 barrel modules, the 12 "F-disks", and the 4 "H-disks". 69

8.3 DØ's scintillating fiber tracker. 72

8.4 One quarter $r-z$ view of the end of the DØ trackers and the start of the EC, indicating the Central Preshower, the Level-0 detector, the solenoid magnet and calorimeter cryostats, and the Forward Preshower detector. The Forward Preshower detector is shown in detail in the inset. 76

8.5 Half $r-z$ view of the DØ muon subdetector. 78

8.6 Illustration of the DØ muon subdetector components. 79

8.7 Layout of PDTs and MDTs. 80

8.8 Geometry of a PDT cell. 82

8.9 DØ forward muon mini-drift tube (MDT) plane. The octant boundaries are shown. 85

8.10 Two DØ forward muon pixel octants. 86

8.11 Design of the DØ trigger system. 89

8.12 Simplified data flow in Level-3/DAQ for DØ Run II. 94

9.1 Invariant mass distribution of the $(\mu^+\mu^-)$ system for all the events. The signal is described by a double Gaussian function and the background by a second order polynomial. The signal mean is 3070.0 ± 0.1 MeV and the fitted widths are $\sigma_1 = 55 \pm 1$ MeV and $\sigma_2 = 100 \pm 1$ MeV. 100

9.2 Invariant mass distribution of the $(\mu^+\mu^-)$ system for all the events containing a Λ candidate. The signal is described by a double Gaussian function and the background by a second order polynomial. The signal mean is 3069 ± 1 MeV and the fitted widths from double Gaussian function are $\sigma_1 = 52 \pm 1$ MeV and $\sigma_2 = 91 \pm 5$ MeV. 101

9.3 Invariant mass distribution of the (p, π) system for all the events containing a J/ψ candidate. The signal is described by a double Gaussian function and the background by a second order polynomial. The signal mean is 1115.3 ± 0.1 MeV and the fitted widths are $\sigma_1 = 4.6 \pm 0.1$ MeV and $\sigma_2 = 2.0 \pm 0.1$ MeV for a double Gaussian function. 102

9.4 Invariant mass distribution of the $(J/\psi, \Lambda)$ system for all Λ_b^0 candidates. The signal is described by a Gaussian function and the background by a constant plus an exponential function. 103

9.5 Top: decay length distribution; and bottom: decay length significance distribution for data. 104

9.6 Invariant mass distribution of the $(J/\psi, \Lambda)$ system for all Λ_b^0 candidates plus the requirement $L_{xy} > 0.01$ cm. The signal is described by a Gaussian function and the background by a constant plus an exponential function. . . 104

9.7 Invariant mass distribution of the $(J/\psi, \Lambda)$ system for all Λ_b^0 candidates plus the requirement $L_{xy} > 0.02$ cm. The signal is described by a Gaussian function and the background by a constant plus an exponential function. . . 105

9.8 Invariant mass distribution of the $(J/\psi, \Lambda)$ system for all Λ_b^0 candidates plus the requirement $L_{xy} > 0.03$ cm. ehe signal is described by a Gaussian function and the background by a constant plus an exponential function. 105

9.9 Invariant mass distribution of the $(J/\psi, \Lambda)$ system for all Λ_b^0 candidates plus the requirement $L_{xy}/\sigma(L_{xy}) > 2$. The signal is described by a Gaussian function and the background by a constant plus an exponential function. . . 106

9.10 Invariant mass distribution of the $(J/\psi, \Lambda)$ system for all Λ_b^0 candidates plus the requirement $L_{xy}/\sigma(L_{xy}) > 4$. The signal is described by a Gaussian function and the background by a constant plus an exponential function. . . 107

9.11 Invariant mass distribution of the $(J/\psi, \Lambda)$ system for all Λ_b^0 candidates plus the requirement $c\tau > 370$ μm. The signal is described by a Gaussian function and the background by a constant plus an exponential function. 108

9.12 Invariant mass distribution of the $(J/\psi, \Lambda)$ system for all Λ_b^0 candidates plus the requirement $c\tau > 740$ μm. The signal is described by a Gaussian function and the background by a constant plus an exponential function. 109

9.13 Invariant mass distribution of the $(J/\psi, \Lambda)$ system for all Λ_b^0 candidates plus the requirement $c\tau > 1000$ μm. The signal is described by a Gaussian function and the background by a constant plus an exponential function. 110

9.14 Invariant mass distribution of Λ_b^0 candidates in MC simulated events. A double Gaussian function was used to model the signal, and a constant plus an exponential function was used for the background. 115

9.15 Top: decay length distribution; bottom: decay length significance distribution for MC simulated events. 116

9.16 Invariant mass distribution of the $(\pi^+\pi^-)$ system for all the events with a J/ψ candidate. The signal is described by a double Gaussian function and the background by a second order polynomial. The signal mean is 493.5±0.1 MeV and the fitted widths are $\sigma_1 = 5.9 \pm 0.1$ MeV and $\sigma_2 = 11.7 \pm 0.1$ MeV. . . 117

9.17 Invariant mass distribution of the $(J/\psi, K_S^0)$ system for all B_d^0 candidates. The signal is described by a Gaussian function and the background by a second order polynomial. 118

9.18 Invariant mass distribution of the $(J/\psi, K_S^0)$ system for all B_d^0 candidates plus the requirement $L_{xy} > 0.01$ cm. The signal is described by a Gaussian function and the background by a second order polynomial. 119

9.19 Invariant mass distribution of the $(J/\psi, K_S^0)$ system for all B_d^0 candidates plus the requirement $L_{xy} > 0.02$ cm. The signal is described by a Gaussian function and the background by a second order polynomial. 119

9.20 Invariant mass distribution of the $(J/\psi, K_S^0)$ system for all B_d^0 candidates plus the requirement $L_{xy} > 0.03$ cm. The signal is described by a Gaussian function and the background by a second order polynomial. 120

9.21 Invariant mass distribution of the $(J/\psi, K_S^0)$ system for all B_d^0 candidates plus the requirement $L_{xy}/\sigma(L_{xy}) > 2$. The signal is described by a Gaussian function and the background by a second order polynomial. 120

9.22 Invariant mass distribution of the $(J/\psi, K_S^0)$ system for all B_b^0 candidates plus the requirement $L_{xy}/\sigma(L_{xy}) > 4$. The signal is described by a Gaussian function and the background by a second order polynomial. 121

9.23 Invariant mass distribution of the $(J/\psi, K_S^0)$ system for all B_d^0 candidates plus the requirement $c\tau > 460$ μm. The signal is described by a Gaussian function and the background by a second order polynomial. 121

9.24 Invariant mass distribution of the $(J/\psi, K_S^0)$ system for all B_d^0 candidates plus the requirement $c\tau > 920$ μm. The signal is described by a Gaussian function and the background by a second order polynomial. 122

9.25 Invariant mass distribution of the $(J/\psi, K_S^0)$ system for all B_d^0 candidates plus the requirement $c\tau > 1320$ μm. The signal is described by a Gaussian function and the background by a second order polynomial. 122

10.1 The proper lifetime distribution in three mass bands (see text). 124

10.2 Invariant mass distribution of the $(J/\psi, \Lambda)$ system for all Λ_b^0 candidates without any lifetime cuts. The signal is described by a Gaussian function and the background by a second order polynomial. 131

10.3 The proper decay length, $c\tau$, of the Λ_b^0 candidates. The curves show: the signal contribution, dotted (green); the background, dashed (red); and total, solid (black). 132

10.4 The proper decay length, $c\tau$, of the sidebands. 132

10.5 Invariant mass distribution of the $(J/\psi, K_S)$ system for all B_d candidates without lifetime cuts. The signal is described by a Gaussian function and the background by a second order polynomial. 133

10.6 The proper decay length, $c\tau$, of the B_d candidates. The curves show: the signal contribution, dotted (green); the background, dashed (red); and total, solid (black). 134

A.1 Re ξ for different MC absorption models. The order of each point from left to right is 1) uncorrected 2) standard FOCUS (baseline): 3) baseline and byproducts 4) baseline and charm absorption zero 5) baseline, charm absorption zero and byproducts, 6) baseline, $\sigma(\bar{D}^0) = 1/2 \times \sigma(\pi^+) = 11.5mb$ and $\sigma(D^0) = 1/2 \times \sigma(\pi^-) = 13mb$, 7) baseline and $\sigma(D^0) = 3/2 \times \sigma(\bar{D}^0)$, 8) baseline and $\sigma(D^0) = 3 \times \sigma(\bar{D}^0)$ (a). Different split samples (b). 138

A.2 Stability of $Re\xi$ for (a) different fit variants and (b) cut variants ($\frac{L}{\sigma}$,Kaonicity) 139

Chapter 1

The Standard Model of Particle Physics

The Standard Model [1] is the currently accepted theory of the fundamental particles and their interactions. It has proven to be a successful theory. Even precision measurements have found no deviations so far from its predictions, with the exception of the neutrino masses [2]. However a number of problems remain, The Standard Model makes no room for including gravity and has the unattractive feature of 18 free parameters or 21 when incorporating massive neutrinos. And we have not measured all the parameters to the same precision. Also we have yet to discover the Higgs which is the cornerstone of the Standard Model. This short chapter will simply list its main components.

Within the Standard Model, there are two broad categories of particles. The fundamental fermions (fermions are particles with fractional spin) are considered to be the matter, the stuff of the universe. For example, the quarks in the protons and neutrons in an atomic nucleus and the electrons surrounding it belong to this category. The fundamental bosons (bosons are particles with integer spin), on the other hand, are responsible for the forces between the matter particles. For example, the quarks in protons and neutrons of the nucleus are held together by gluons and electrons are bound to the nucleus by the exchange of "virtual" photons.

The interactions between matter particles take place through the exchange of the fundamental bosons. These interactions are described by the Lagrangian of the Standard Model, leading to equations that specify rules for calculating quantities such as the probabilities for certain reactions to occur, referred to as cross sections.

1.1 The Fundamental Particles

According to the Standard Model, there are 24 fundamental matter particles (see Tables 1.1 and 1.2) – six quarks (the up, down, strange, charm, bottom and top quarks) coming in three different colors [3] and six leptons (the electron, muon, tau, and a neutrino) [29]. All of the elements of the periodic table can be built from combinations of only three of these 24: the up quark, the down quark, and the electron. An oxygen atom, for example, has eight electrons surrounding a nucleus of eight protons and eight neutrons. Protons are built from two up quarks and one down quark; and neutrons are two down quarks and one up quark.

Because of the strength of the forces between them (the strong force), quarks are confined to exist in composites. A combination of a quark and an antiquark is a meson (e.g., a pion or kaon), and a combination of three quarks is a baryon (e.g., a proton or neutron). Mesons and baryons are collectively termed hadrons. While the vast majority of the matter we encounter in everyday life consists only of up and down quarks, the other four quarks are equally as fundamental. The essential difference is only in their greater masses.

The lepton category of the fundamental particles consists of three negatively charged particles, of which the electron is prototypical, and their three very weakly interacting neutral partners, the neutrinos. The muon and tau differ from the electron only in mass. Neutrinos are only emitted during weak processes and only interact weakly, and are therefore extraordinarily difficult to detect. All of these fundamental fermions have anti-matter partners.

1.2 The Fundamental Forces

The fundamental particles interact through four different forces. Probably the most familiar of the forces is gravity, the force of attraction between massive bodies. However due to the smallness of the masses of the fundamental particles, the force of gravity between

Table 1.1: Properties of the quarks.

Name	Symbol	Charge
Up Quark	u	$+2/3$
Down Quark	d	$-1/3$
Strange Quark	s	$-1/3$
Charm Quark	c	$+2/3$
Bottom Quark	b	$-1/3$
Top Quark	t	$+2/3$

Table 1.2: Properties of the leptons.

Name	Symbol	Mass	Charge
Electron	e	$0.511\,\mathrm{MeV}/c^2$	-1
Muon	μ	$105.6\,\mathrm{MeV}/c^2$	-1
Tau	τ	$1.777\,\mathrm{GeV}/c^2$	-1
Electron Neutrino	ν_e	$< 3\,\mathrm{eV}/c^2$	0
Muon Neutrino	ν_μ	$< 0.17\,\mathrm{MeV}/c^2$	0
Tau Neutrino	ν_τ	$< 18\,\mathrm{MeV}/c^2$	0

Table 1.3: Properties of the gauge bosons.

Name	Symbol	Mass	Charge
Photon	γ	0	0
W Boson	$W^{\pm}$	$80.4\,\mathrm{GeV}/c^2$	± 1
Z Boson	Z^0	$91.19\,\mathrm{GeV}/c^2$	0
Gluon	g	0	0

any of them is negligible. It is hoped that gravity will someday be described by a theory unifying it to the other three forces, but the Standard Model does not incorporate the gravitational force. The forces of the Standard Model are all described by the exchange of force-carrying particles, the gauge bosons (see Table 1.3).

Electromagnetism is the force responsible for the repulsion between like charges, the attraction between unlike charges, the deflection of charged particles in magnetic fields, etc. In the Standard Model, the force is due to the exchange of "virtual" photons, which interact with any charged body. In addition, in Quantum Electrodynamics (QED), the Standard Model theory of electromagnetism, photons can convert to electrons and positrons, an electron can emit a photon, electrons and positrons can annihilate into photons, etc.

The strong force acts only on quarks, and is due to the exchange of gluons. Similiar to the electric charge for electromagnetism, the strong force proceeds through a charge of its own, the "color" charge. But unlike electromagnetism, where the photon has no electric charge of its own, gluons do carry color charge, allowing them to interact among themselves and thus creating a much more complex situation. The strong force binds quarks tightly into hadrons, so tightly that the quarks never appear unbound. The Standard Model theory of the strong force is Quantum Chromodynamics (QCD).

Finally, the weak force affects all of the fundamental particles. It is carried by the $W^{\pm}$ and Z^0 bosons. Nuclear beta decay is the most familiar example of this force, where one of the down quarks of a neutron converts to an up quark by emitting a W^-, which subsequently decays to an electron and an electron antineutrino. The Standard Model theory of the weak

force and QED are united into a single theory, the electroweak theory [4], by introducing a Higgs Boson. The search for the Higgs Boson, the last of the Standard Model particles to be experimentally undiscovered, is one of the major efforts of contemporary high energy physics.

1.3 Lagrangians

The mathematical structure of the Standard Model is contained in a series of Lagrangians.

$$\mathcal{L}_{SM} = \mathcal{L}_{QED} + \mathcal{L}_{QCD} + \mathcal{L}_{Weak}. \tag{1.1}$$

For example, the QED Lagrangian can be written as:

$$\mathcal{L}_{QED} = \overline{\psi}(i\gamma^{\mu}\partial_{\mu} - qA_{\mu}\gamma^{\mu} - m)\psi - \frac{1}{4}F_{\mu\nu}F^{\mu\nu}, \tag{1.2}$$

where

$$F^{\mu\nu} \equiv \partial^{\mu}A^{\nu} - \partial^{\nu}A^{\mu}. \tag{1.3}$$

Here, ψ represents a particle with charge q, and A_{μ} represents the photonic vector field. The first term describes the kinetic energy of the particle, and together with the mass term, they constitue the Lagrangian density of a free particle. The second term describes the interaction of the particle with the electromagnetic field. The last term describes the free electromagnetic field.

Part I

Chapter 2

CPT Formalism

The combined symmetry of charge conjugation (C), parity (P), and time reversal (T) is believed to be respected by all local, point-like, Lorentz covariant field theories, such as the Standard Model we outlined in Chapter 1. However, extensions to the Standard Model based on string theories do not necessarily require CPT invariance, and observable effects at low-energies may be within reach of experiments studying flavor oscillations [5]. A parametrization [6] in which CPT and T violating parameters appear has been developed, which allows experimental investigation in many physical systems including atomic systems, Penning traps, and neutral meson systems [7]. Using this parameterization we present the first experimental search for CPT violation in the charm meson system.

2.1 Mixing Formalism

Before we introduce CPT formalism, we want to outline mixing formalism, since much of the notation from standard mixing in charm mesons is used there.

Assuming CP conservation in the charm meson system, the CP eigenstates of the neutral D meson can be written as,

$$|D_1\rangle = \frac{1}{\sqrt{2}}\left(|D^0\rangle + |\overline{D^0}\rangle\right), \qquad \text{and} \qquad |D_2\rangle = \frac{1}{\sqrt{2}}\left(|D^0\rangle - |\overline{D^0}\rangle\right). \tag{2.1}$$

If we define $CP|D^0\rangle = |\overline{D^0}\rangle$, it then follows that $|D_1\rangle$ is a CP-even state and $|D_2\rangle$ is CP-odd.

The time evolution of the $|D_1\rangle$ and $|D_2\rangle$ states is given by

$$|D_i(t)\rangle = e^{-i(M_i - i\frac{\Gamma_i}{2})t}|D_i(0)\rangle, \tag{2.2}$$

where M_i and Γ_i are the mass and the width for state i. Rearranging Eq. 2.1, we find in terms of D_1 and D_2, that a pure D^0 state produced at time $t = 0$ is

$$|D^0(t=0)\rangle = \frac{1}{\sqrt{2}}\left(|D_1\rangle + |D_2\rangle\right). \tag{2.3}$$

We obtain the time evolution of D^0 by plugging in the time evolution of the D_1 and D_2 states as given by Equation 2.2:

$$|D^0(t)\rangle = \frac{1}{\sqrt{2}}\left(e^{-i(M_1 - i\frac{\Gamma_1}{2})t}|D_1(0)\rangle + e^{-i(M_2 - i\frac{\Gamma_2}{2})t}|D_2(0)\rangle\right). \tag{2.4}$$

This can be expressed in terms of the $|D^0\rangle$ and $|\overline{D^0}\rangle$ by using the relations in the Equations 2.1 and combining like terms:

$$|D^0(t)\rangle = \frac{1}{2}\left(A_+|D^0\rangle + A_-|\overline{D^0}\rangle\right), \tag{2.5}$$

with

$$A_\pm = e^{-i(M_1 - i\frac{\Gamma_1}{2})t} \pm e^{-i(M_2 - i\frac{\Gamma_2}{2})t}. \tag{2.6}$$

The terms $A_\pm$ can be arranged in more convenient forms by using the definitions:

$$\Gamma = \frac{\Gamma_1 + \Gamma_2}{2}, \quad M = \frac{M_1 + M_2}{2}, \quad x = \frac{-(M_1 - M_2)}{\Gamma}, \text{ and } \; y = \frac{\Gamma_1 - \Gamma_2}{2\Gamma}. \tag{2.7}$$

The expressions for $A_\pm$ with these definitions are

$$A_+ = 2e^{-(iM + \frac{\Gamma}{2})t}\cosh\left[(y + ix)\frac{\Gamma t}{2}\right] \tag{2.8}$$

and

$$A_- = -2e^{-(iM + \frac{\Gamma}{2})t}\sinh\left[(y + ix)\frac{\Gamma t}{2}\right]. \tag{2.9}$$

Now we pose the question: what is the probability of an originally pure D^0 state to decay to $K^+\pi^-$? Define $\langle f|$ as the vector representing the final state $K^+\pi^-$. The amplitude for this decay process is:

$$\langle f|D^0(t)\rangle = \\ e^{-(iM+\frac{\Gamma}{2})t}\left\{\cosh\left[(y+ix)\frac{\Gamma t}{2}\right]\langle f|D^0\rangle - \sinh\left[(y+ix)\frac{\Gamma t}{2}\right]\langle f|\overline{D^0}\rangle\right\}, \tag{2.10}$$

where $\langle f|D^0\rangle$ is the Double Cabbibo Suppressed (DCS) decay amplitude and $\langle f|\overline{D^0}\rangle$ is the Cabbibo Favored (CF) amplitude. The DCS to CF amplitude ratio is written as

$$\frac{\langle f|D^0\rangle}{\langle f|\overline{D^0}\rangle} = -\sqrt{R_{DCS}}e^{-i\delta}, \tag{2.11}$$

where R_{DCS} is the DCS to CF branching ratio and δ is a strong force phase between DCS and CF amplitudes. Plugging this in and approximating the hyperbolic functions with the first term of their Taylor series expansions we obtain

$$\langle f|D^0(t)\rangle = e^{-(iM+\frac{\Gamma}{2})t}\langle f|\overline{D^0}\rangle\left[-\sqrt{R_{DCS}}e^{-i\delta} - (y+ix)\frac{\Gamma t}{2}\right]. \tag{2.12}$$

Finally the probability is the absolute value square of the amplitude:

$$|\langle f|D^0(t)\rangle|^2 = \\ e^{-\Gamma t}|\langle f|\overline{D^0}\rangle|^2\left[R_{DCS} + \sqrt{R_{DCS}}(y\cos\delta - x\sin\delta)\Gamma t + (\frac{x^2+y^2}{4})\Gamma^2 t^2\right]. \tag{2.13}$$

We use the soft pion from the decay $D^{*+} \to D^0\pi^+$ to tag the flavor of the D at production, and the kaon charge in the decay $D^0 \to K^-\pi^+$ to tag the D flavor at the time of decay. Right-sign signal (RS) is obtained by requring that the soft pion charge is equal the opposite of kaon charge. Wrong-sign signal (WS) is obtained by requring that the soft pion charge is equal the kaon charge. Define a quantity $R(t)$, which is the time-dependent rate for the WS process relative to CF (RS) branching fraction or

$$R(t) = \frac{|\langle f|D^0(t)\rangle|^2}{|\langle f|\overline{D^0}\rangle|^2}, \tag{2.14}$$

and define the parameters x' and y' that are related to the mixing parameters, x and y, by a strong phase rotation:

$$x' = x\cos\delta + y\sin\delta, \qquad y' = y\cos\delta - x\sin\delta. \tag{2.15}$$

Redefine t in units of D^0 lifetime (where $\Gamma t = t/\tau_{D^0}$) to obtain an expression for the lifetime evolution of the decay $D^0 \to K^+\pi^-$:

$$R(t) = \left[R_{DCS} + \sqrt{R_{DCS}}y't + (\frac{x'^2 + y'^2}{4})t^2\right]e^{-t/\tau_{D^0}}. \tag{2.16}$$

The first term in Eq. 2.16 is a pure DCS decay amplitude, the second term is the interference of DCS and mixing, and the third term is a pure mixing term.

2.2 Proper Time Asymmetry

The time evolution of a neutral-meson state is governed by a 2×2 effective Hamiltonian matrix Λ in the Schrödinger equation. For a complex 2×2 matrix, it is possible to write the two diagonal elements as the sum and difference of two complex numbers. It is also possible to write the off-diagonal elements as the product and ratio of two complex numbers. Using these two facts, which ultimately permit the clean representation of T and CPT-violating quantities, a general expression for Λ can be taken as [6]:

$$\Lambda = \frac{1}{2}\Delta\lambda \begin{pmatrix} U + \xi & VW^{-1} \\ VW & U - \xi \end{pmatrix}, \tag{2.17}$$

where the parameters U, V, W, and ξ are complex. The requirements that the trace of the matrix is $tr\Lambda = \lambda$ and that the determinant is $det\Lambda = \lambda_1\lambda_2$ impose the identifications $U = \lambda/\Delta\lambda$, $V = \sqrt{1-\xi^2}$ on the complex parameters U and V. The free parameters in Eq. 2.17 are therefore W and ξ. These can be regarded as four independent real quantities: $W = we^{i\omega}$, and $\xi = \mathrm{Re}\,\xi + i\mathrm{Im}\,\xi$. One of these four real numbers, the argument ω, is arbitrary and physically irrelevant. The other three are physical. The modulus of W

controls T violation with $w = 1$ if and only if T is preserved. The two remaining real numbers, $\mathrm{Re}\,\xi$ and $\mathrm{Im}\,\xi$, control CPT violation and both are zero if and only if CPT is preserved. The quantities w and ξ can be expressed in terms of the components of Λ as $w = \sqrt{|\Lambda_{21}/\Lambda_{12}|}$, $\xi = \Delta\Lambda/\Delta\lambda$, where $\Delta\Lambda = \Lambda_{11} - \Lambda_{22}$ and $\Delta\lambda$ is the difference in the eigenvalues. $\lambda_1 = M_1 - \frac{1}{2}i\Gamma_1$, $\lambda_2 = M_2 - \frac{1}{2}i\Gamma_2$ and $\Delta\lambda = \Gamma(x - i\,y)$. ξ is phenomenologically introduced and therefore independent of the model. Indirect CPT violation occurs if and only if the difference of diagonal elements of Λ is nonzero. To determine the time-dependent decay amplitudes and probabilities, it is useful to obtain an explicit expression for the time evolution of the neutral D meson. Doing the same exercise as in the mixing formalism (with Λ as the matrix) we obtain,

$$\begin{pmatrix} D^0(t,\hat{t},p) \\ \overline{D^0}(t,\hat{t},p) \end{pmatrix} = \begin{pmatrix} C + S\xi & SVW \\ SVW^{-1} & C - S\xi \end{pmatrix} \begin{pmatrix} D^0 \\ \overline{D^0} \end{pmatrix}. \tag{2.18}$$

The functions C and S depend on the meson proper time t, sidereal time $\hat{t}$ and are given by:

$$C = \cos\left(\frac{1}{2}\Delta\lambda t\right) e^{-\frac{1}{2}i\lambda t} \qquad S = -i\sin\left(\frac{1}{2}\Delta\lambda t\right) e^{-\frac{1}{2}i\lambda t}. \tag{2.19}$$

One can easily extract time-dependent decay probabibilities by manipulating Eq. 2.18. For the decay of D^0 to a right-sign final state f (which could be a semileptonic mode, or a Cabibbo favored hadronic mode (with DCS negligible)), the time-dependent decay probability is

$$\begin{aligned} P_f(t) &\equiv |\langle f|T|D^0(t)\rangle|^2 \\ &= \frac{1}{2}|F|^2\exp(-\frac{\gamma}{2}t) \times [(1+|\xi|^2)\cosh\Delta\gamma t/2 + (1-|\xi|^2)\cos\Delta m t \\ &\quad -2\ \mathrm{Re}\ \xi\ \sinh\Delta\gamma t/2 - 2\ \mathrm{Im}\ \xi\ \sin\Delta m t]. \end{aligned} \tag{2.20}$$

The time-dependent probability for the decay of $\overline{D}^0$ to a right-sign final state $\overline{f}$, $\overline{P}_{\overline{f}}(t)$, may be obtained by replacing in the above equation $\xi \to -\xi$ and $F \to \overline{F}$. In the formula,

F represents the basic transition amplitude for the decay $D^0 \to f$, $\Delta\gamma$ and Δm are the differences in physical decay widths and masses for the propagating eigenstates and can be related to the usual mixing parameters $x = \Delta M/\Gamma$ and $y = \Delta\Gamma/2\Gamma$. The complex parameter ξ controls the CPT violation and is seen to modify the shape of the time dependent decay probabilities. Expressions for wrong-sign decay probabilities involve both CPT and T violation parameters that scale the probabilities, leaving the shape unchanged. Using only right-sign decay modes, the following asymmetry can be formed,

$$A_{CPT}(t) = \frac{\overline{P}_{\overline{f}}(t) - P(t)}{\overline{P}_{\overline{f}}(t) + P(t)}, \tag{2.21}$$

which is sensitive to the CPT violating parameter ξ:

$$A_{CPT} = \frac{2 \text{ Re } \xi \sinh\Delta\gamma t/2 + 2 \text{ Im } \xi \sin\Delta m t}{(1+|\xi|^2)\cosh\Delta\gamma t/2 + (1-|\xi|^2)\cos\Delta m t}. \tag{2.22}$$

We can gain insight into the anticipated experimental sensitivity by plotting these functions with some reasonable assumptions. We use 95% confidence level (C.L.) upper bounds on the mixing parameters x and y of 5%, which is at the upper range of the current experimental sensitivity, as discussed previously. In Fig. 2.1(a) we plot the proper time decay probabilities for D^0 decay under the assumption of CPT violation at the level of Re ξ = 5% and Im ξ = 5%, which are independent parameters in the framework. One sees a CPT violation-induced wrong-sign contribution that vanishes both at zero proper time and at long proper times. This causes a distortion from a purely exponential decay of a D^0 (and $\overline{D}^0$), which is then visible in the asymmetry plot, A_{CPT} as shown in Fig. 2.1(b). Because of the small oscillation frequency and short lifetime, one sees only the start of the oscillation, growing beyond 0.3% at long proper times. Evident from Eqn. 2.22 is that positive values of Re ξ and Im ξ work to oppose one another in the asymmetry in a linear fashion. This is shown in the nearly linear behavior of A_{CPT} in Figs. 2.1(c,d) with parameters Im ξ = 5%, Re $\xi = 0$ and Im $\xi = 0$, Re ξ = 5% respectively, and consequently CPT asymmetries larger by a factor of 10 at long proper times. In practice, experiments will be sensitive to either Re ξ or Im ξ, but not both simultaneously.

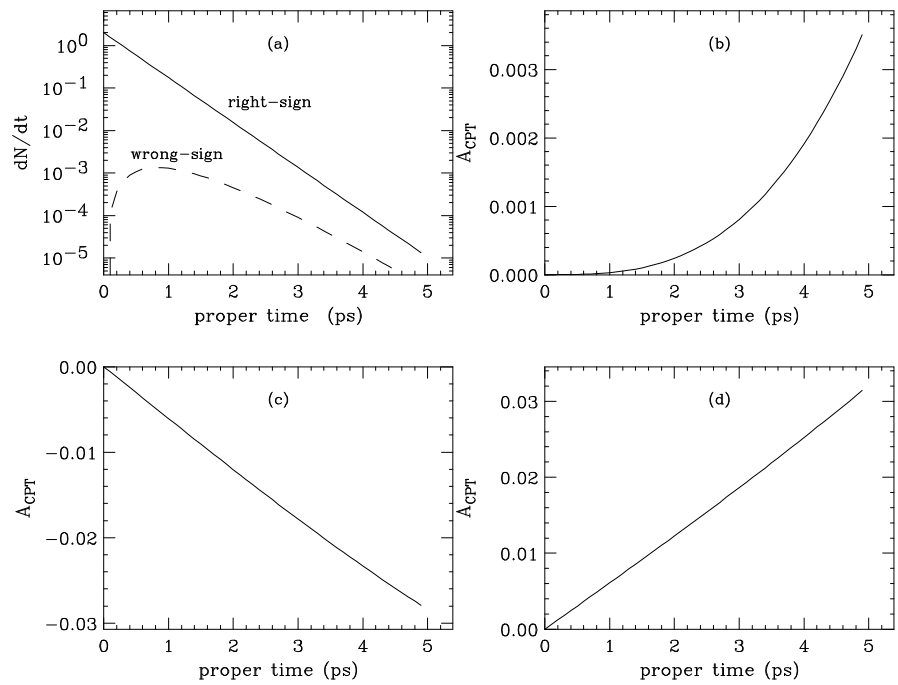

Figure 2.1: (a) Proper time decay probabilities for D^0 decay, right-sign (solid) and wrong-sign (dashed) and (b) A_{CPT} with Re $\xi = 5\%$, Im $\xi = 5\%$. (c) A_{CPT} with Re $\xi = 0$, Im $\xi = 5\%$. (d) A_{CPT} with Re $\xi = 5\%$, Im $\xi = 0$.

2.3 Double Cabbibo Suppressed Interference

In the previous section, we generated the asymmetry by assuming the basic transition amplitudes to be $\langle f|T|D^0\rangle = F$, $\langle f|T|\bar{D^0}\rangle = 0$, $\langle \overline{f}|T|\bar{D^0}\rangle = \overline{F}$, $\langle \overline{f}|T|D^0\rangle = 0$. This is fine as long as we are dealing with a semileptonic decay or if we neglect the Double Cabbibo Suppressed decays (DCS) of hadronic modes. The general framework developed in Ref. [6] assumes that the DCS effects are negligible. However in our forming the asymmetry we had to deal with DCS that were comparable to Cabbibo favored decays. We therefore will report the asymmetry in the previous section with DCS effects included. For the decay $D^0 \to K^-\pi^+$ the basic transition amplitudes are then $\langle f|T|D^0\rangle = F$, $\langle f|T|\bar{D^0}\rangle = F_{\rm DCS}$, $\langle \overline{f}|T|\bar{D^0}\rangle = \overline{F}$, and $\langle \overline{f}|T|D^0\rangle = \overline{F_{\rm DCS}}$.

For us to see if we can neglect DCS, we have to start with the more general framework where the DCS interference with the Cabbibo favored decays and the DCS term are not

neglected. Now we assume that $\langle f|T|\bar{D}^0\rangle = F_{\rm DCS}$ and $\langle \overline{f}|T|D^0\rangle = \overline{F_{\rm DCS}}$ are not neglected. To touch base with the formalism already developed for mixing, we will take the ratio $\langle \overline{f}|T|D^0\rangle/\langle \overline{f}|T|\bar{D}^0\rangle = -\sqrt{R_{\rm DCS}}\ e^{-i\delta}$ and $\langle f|T|\bar{D}^0\rangle/\langle f|T|D^0\rangle = -\sqrt{R_{\rm DCS}}\ e^{i\delta}$. With these in mind, the time dependent probability into a right-sign decay as in Eq. 2.20 including DCS presence takes this more general form:

$$
\begin{aligned}
P_f(t) &\equiv |\langle f|T|D^0(t)\rangle|^2 \\
&= \frac{1}{2}|F|^2\exp(-\frac{\gamma}{2}t) \times [(1+|\xi|^2)\cosh\Delta\gamma t/2 + (1-|\xi|^2)\cos\Delta m t \\
&\quad -2\ \mathrm{Re}\ \xi\ \sinh\Delta\gamma t/2 - 2\ \mathrm{Im}\ \xi\ \sin\Delta m t - 2\ \sqrt{R_{DCS}} \times \\
&\quad [(-\sinh\Delta\gamma t/2\ \cos\delta - \sin\Delta m t\ \sin\delta) \\
&\quad +(\cosh\Delta\gamma t/2 - \cos\Delta m t) \times (\mathrm{Re}\xi\ \cos\delta + \mathrm{Im}\xi\ \sin\delta)] \\
&\quad +R_{DCS} \times (\cosh\Delta\gamma t/2 - \cos\Delta m t)]. \qquad (2.23)
\end{aligned}
$$

The time-dependent probability for the decay of $\overline{D}^0$ to a right-sign final state $\overline{f}$, $\overline{D}_{\overline{f}}(t)$, may be obtained by replacing $\xi \to -\xi$ and $F \to \overline{F}$ in the above equation.

R_{DCS} is the ratio of DCS decay to the Cabbibo favored decay. δ is the strong mixing phase between DCS decay and Cabbibo favored. Using only right-sign decay modes, we form the asymmetry as in Eq. 2.21 that is sensitive to the CPT-violating parameter ξ. In the case of negligible contributions from DCS decay, $|\langle f|T|\overline{D^0(t)}\rangle| = 0$, we can form an identical asymmetry contribution as given by Eq. 2.22:

$$
A^0_{CPT}(t) = \frac{2\ \mathrm{Re}\ \xi\ \sinh\Delta\gamma t/2 + 2\ \mathrm{Im}\ \xi\ \sin\Delta m t}{(1+|\xi|^2)\cosh\Delta\gamma t/2 + (1-|\xi|^2)\cos\Delta m t}. \qquad (2.24)
$$

We can form the same asymmetry as in Eq. 2.22 by using, instead of probabilities given by Eq. 2.20, the probabilities given by Eq. 2.23 [1]. We have this additional interference term

[1] We have assumed that T is not violated and thus the phase related to T is zero, i.e., the only phase that enters in the probabilities due to interference is the strong phase.

in the A_{CPT} expression, which ignores the small contributions in the denominator:

$$A^{int}_{CPT}(t) = \frac{2\sqrt{R_{DCS}} \times (\cosh\Delta\gamma t/2 - \cos\Delta m t) \times (\mathrm{Re}\xi\ \cos\delta + \mathrm{Im}\xi\ \sin\delta)}{(1+|\xi|^2)\cosh\Delta\gamma t/2 + (1-|\xi|^2)\cos\Delta m t}. \tag{2.25}$$

With these new modifications, the total A_{CPT} is the sum of the two contributions, $A_{CPT} = A^0_{CPT}(t) + A^{int}_{CPT}(t)$. From this general expression of A_{CPT}, two different approaches can be taken. In the first approach we assume that Eq. 15 of [6] does not hold but Eq. 21 of [6] is valid since it is phenomenologically introduced and is not dependent on the model. Equation 15 of [6] is Re $\xi = x$ Imξ/y in terms of x, y mixing values. With small values of mixing, and the fact that D^0 has a relatively short lifetime, the following approximation is valid:

$$A_{CPT} = Re\xi\ y\ t/\tau - Im\xi\ x\ t/\tau + O(\sqrt{(}R_{\mathrm{DCS}})(x^2+y^2)). \tag{2.26}$$

In the second approach, we assume that Eq. 15 of [6] does hold, so we have Re $\xi =$ x Imξ/y. Under this constraint, and with small values of x, y mixing, our expression of A_{CPT} takes this form

$$A_{\mathrm{CPT}} = \frac{\mathrm{Re}\,\xi(x^2+y^2)(t/\tau)^2}{2x}\left[\frac{xy}{3}(t/\tau) + \sqrt{R_{\mathrm{DCS}}}\,(x\,\cos\delta + y\,\sin\delta)\right]. \tag{2.27}$$

This scenario is more strict since it requires that Eq. 15 of [6] is valid. While in the first approach we neglected the DCS decay interference term as small, we can not neglect it in the second approach because DCS interference term plays a comparable role in the A_{CPT}. In this thesis and the resulting journal result [18], we consider both these scenarios since the question of the constraint given by Eq. 15 of [6] is an open question.

2.4 Lorentz Violating Parameters

In the CPT and Lorentz-violating extension (SME) to the Standard Model [19], the CPT violating parameters may depend on lab momentum, orientation, and sidereal time [6, 20]. It can be shown that [20]

$$\Delta\Lambda \approx \beta^{\mu}\Delta a_{\mu}, \tag{2.28}$$

where $\beta^{\mu} = \gamma(1, \vec{\beta})$ is the four-velocity of the D meson in the observer frame. The effect of Lorentz and CPT violation in the SME appears in Eq. 2.28 via the factor $\Delta a_{\mu} = r_{q_1} a_{\mu}^{q_1} - r_{q_2} a_{\mu}^{q_2}$, where $a_{\mu}^{q_1}$ and $a_{\mu}^{q_2}$ are CPT- and Lorentz-violating coupling coefficients for the two valence quarks in the D meson, and where r_{q_1} and r_{q_2} are quantities resulting from quark-binding and normalization effects. The coefficients $a_{\mu}^{q_1}$ and $a_{\mu}^{q_2}$ for Lorentz and CPT-violation have mass dimension one and emerge from terms in the Lagrangian for the SME of the form $-a_{\mu}^{q}\bar{q}\gamma^{\mu}q$, where q specifies the quark flavor. A significant consequence of the four-momentum dependence arises from the rotation of the Earth relative to the constant vector $\Delta\vec{a}$. This leades to sidereal variations for CPT violating parameter ξ. In the case of FOCUS, a forward, fixed-target spectrometer, the ξ parameter assumes the following form:

$$\xi(\hat{t}, p) \quad = \quad \frac{\gamma(p)}{\Delta\lambda}[\Delta a_0 + \beta\Delta a_Z \cos\chi + \beta \sin\chi(\Delta a_Y \sin\Omega\hat{t} + \Delta a_X \cos\Omega\hat{t})], \tag{2.29}$$

where Ω and $\hat{t}$ are the sidereal frequency and time respectively, and X, Y, Z are non-rotating coordinates with Z aligned with the Earth's rotation axis. Δa_X, Δa_Y, Δa_0 and Δa_Z are the differences in the Lorentz-violating coupling coefficients between valence quarks. χ is the angle between the D^0 momentum and the Z axis. The parameter $\Delta\lambda$ in terms of x and y is:

$$\Delta\lambda = -\Delta m - \frac{i\Delta\gamma}{2} = x\Gamma - iy\Gamma = \Gamma(x - i\ y) = \frac{(x - iy)}{\tau}, \tag{2.30}$$

where τ is the mean lifetime of the D^0 meson.

2.5 Sidereal Time

Since CPT-violating parameters depend on sidereal time, we outline what sidereal time is and how we calculate it. Sidereal time is time according to the stars and not the sun. Careful observation of the sky will show that any specific star will cross directly overhead (on the meridian) about four minutes earlier every day. In other words, the day according to the stars (the sidereal day) is about four minutes shorter than the day according to the sun (the solar day). If we measure a day from noon to noon – from when the sun crosses the meridian (directly overhead) to when the sun crosses the meridian – again we will find the average solar day is about 24 hours. If we measure the day according to a particular star from when that star crosses the meridian to when that star crosses the meridian again we will find the average sidereal day is 23 hours and 56 minutes long. The 4 minute lag is explained by the fact that the earth not only rotates about its axis but also proceeds along its orbit around the sun, while with respect to the stars the earth's motion around the sun can be neglected. Denote $\hat{t}$ as Greenwich Mean Sidereal Time (GMST), and d the number of days that have passed or have to be passed since the epoch. In most astronomy books, the epoch starts on January 1st, 2000 AD, 12:00 noon Greenwich London time. There is an algorithm that finds the total number of days since that epoch [21]. Let d be the total number of full days that have passed or are to pass since that epoch, y the number of years, and m the number of months:

$$d = 367y - \text{int}(\frac{7}{4}(y + \text{int}(\frac{m+9}{12}))) + \text{int}(\frac{275m}{9}) + day - 730531.5. \tag{2.31}$$

Now we want to have the total number of full days plus the fraction of a day, so we have $d_{tot} = d + (h + min/60)/24$ in order to find sidereal time at that particular time of the day. h is the Greenwich UT hour and min is Greenwich UT minute. Now that we have the total number of days including the fractional part, the GMST angle [21] is given by:

$$GMST_{angle} = 280.46061837 + 360.98564736629 \times d_{tot}. \tag{2.32}$$

From this number we remove multiples of 360, and what is left is the hour angle. In order to convert to hours we take $\hat{t} = GMST_{hour} = GMST_{angle}24/360$. In our experiment, spill number comes with a time stamp, so we had to map spills with time stamps known to within 1 minute. A spill results in collisions and events. These time stamps were in Chicago time, and had to be converted to Universal Time (UT). During the year that data was taken, two important dates had to be included, Daylight Saving Time ending October 26, 1996 00:00 and Daylight Saving Time begining April 6, 1997 00:00. During Daylight Saving Time, we have to add 5 hours to Chicago local time to find Universal Time, but when there is no Daylight Saving Time, we add 6 hours to Chicago Local Time. After they are converted to UT, Eq. 2.31 and Eq. 2.32 were used to find the Greenwich Mean Sidereal Hour $\hat{t}$.

2.6 Previous Searches

Searches for CPT violation have been made in the neutral kaon system. Using an earlier CPT formalism [8], KTeV reported a bound on the CPT figure of merit $r_K \equiv |m_{K^0} - m_{\overline{K}^0}|/m_{K^0} < (4.5 \pm 3) \times 10^{-19}$ [9]. A more recent analysis, using the framework described in reference [6] and more data extracted limits on the coefficients for Lorentz violation of $\Delta a_X, \Delta a_Y < 9.2 \times 10^{-22}$ GeV [10]. CPT tests in B^0 meson decay have been made by OPAL at LEP [11], and by Belle at KEK which has recently reported $r_B \equiv |m_{B^0} - m_{\overline{B}^0}|/m_{B^0} < 1.6 \times 10^{-14}$ [12].

To date, no experimental search for CPT violation has been made in the charm quark sector. This is due in part to the expected suppression of $D^0 - \bar{D}^0$ oscillations in the "Standard Model", and the lack of a strong mixing signal in the experimental data.

Recent mixing searches include a study of lifetime differences between charge-parity (CP) eigenstates from FOCUS, which reported [13–15] a value for the parameter $y_{CP} = (3.42 \pm 1.39 \pm 0.74)\%$. The CLEO Collaboration has reported 95% confidence level bounds on mixing parameters x' and y' (related to the usual parameters x and y by a strong phase shift): [16] $(1/2)x'^2 < 0.041\%$ and $-5.8\% < y' < 1\%$. FOCUS has reported [17] a study of

the doubly Cabbibo suppressed ratio (R_{DCS}) for the decay $D^0 \to K^+\pi^-$ and has extracted a contour limit on y' (of order few %) under varying assumptions of R_{DCS} and x'. The question arises – what can be learned about indirect CPT violation given the apparent smallness of mixing in the charm system? It turns out that even in the absence of a strong mixing signal one can still infer the level of CPT violation sensitivity through study of the time dependence of D^0 decays, which we show in this thesis.

Chapter 3

The E831/FOCUS Experiment at Fermilab

FOCUS is a high-energy photoproduction experiment that took data during the Fermilab 1996–1997 fixed-target run. A bremsstrahlung-generated photon beam with energies ranging from approximately 20 to 300 GeV was incident on a BeO target. While the primary purpose of the FOCUS experiment is to study the photoproduction of charm and the properties of charmed mesons and baryons, the experiment has also been able to collect an impressive sample of light quark events. This chapter will give a brief overview of the FOCUS experiment and its detector.

3.1 Physics Overview

The FOCUS experiment has been at the forefront of charm physics since its analysis efforts began around 1998. Improving on its predecessor, E687 [22], FOCUS has been able to reconstruct over one million D mesons (see Fig. 3.1). Over thirty papers have been published on topics such as semileptonic charm decays, charmed baryon lifetimes, CP violation in the charm sector, and the spectroscopy of charmed meson and baryon excited states[1].

[1] A list of publications and more detail concerning ongoing physics analyses can be found at http://www-focus.fnal.gov/

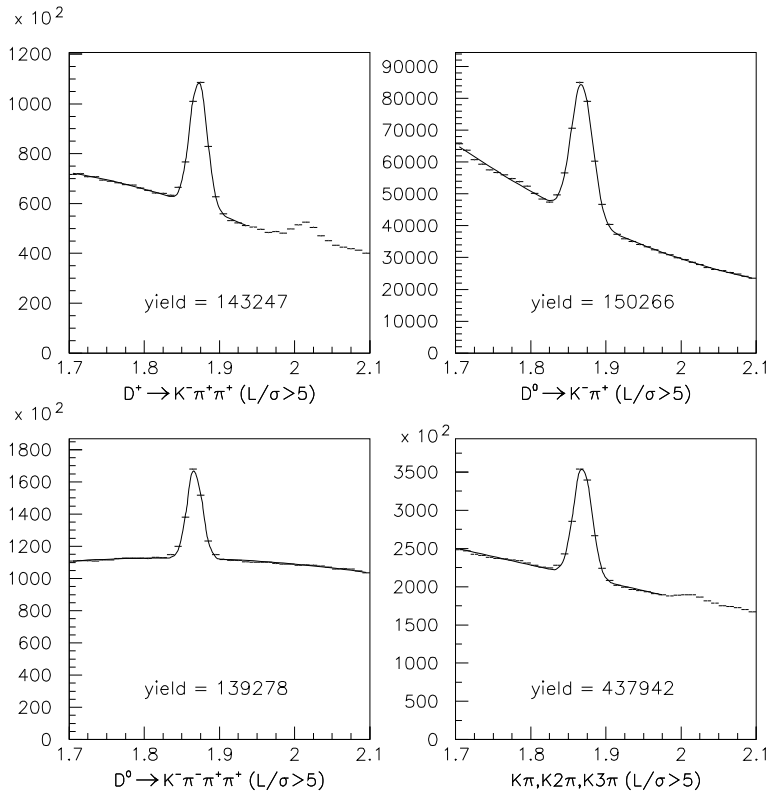

Figure 3.1: The FOCUS D meson signal in three different final states. $L/\sigma > 5$ was applied, where L/σ is the D meson decay length over its error.

3.2 The Accelerator

During the Fermilab 1996–1997 fixed-target run, 800 GeV protons from the Fermilab Tevatron were used to feed an array of fixed-target experiments. In the Main Switchyard, the proton beam extracted from the Tevatron was split into a meson beam line, a neutrino beam line, and a proton beam line. The FOCUS photon beam originated from the proton beam line. Figure 3.2 shows the general layout of Fermilab and the fixed target lines.

The 800 GeV protons of the Tevatron are generated in a series of five stages, each stage increasing the energy of the beam. The process begins with the Cockcroft-Walton, where electrons are added to hydrogen atoms to form negatively charged ions. The negative electric charge allows the H^- ions to be accelerated across an electrostatic gap to an energy of 750 keV. Next, the H^- ions are fed into a linear accelerator (Linac). The Linac accelerates the H^- ions from 750 keV to 400 MeV using a series of RF cavities. Once at the end of the accelerator, the ions are stripped of their electrons in a thin carbon foil, the result of which is a 400 MeV proton beam. From the Linac, the proton beam is picked up by the Booster synchrotron. With a relatively small diameter of 500 feet, the Booster accelerates the protons from 400 MeV to 8 GeV. By way of the Main Injector, the protons are now ready to enter the much larger Main Ring, a synchrotron with a 4 mile circumference housed in the same tunnel as the Tevatron. The Main Ring brings the energy of the protons from 8 GeV up to 150 GeV. In the final stage of acceleration, the protons are transferred from the Main Ring to the Tevatron. Using 1000 superconducting magnets, the Tevatron boosts the proton energy from 150 GeV to its final energy of 800 GeV for fixed target experiments.

During the fixed-target run period, the Tevatron held 1000 proton bunches separated by 20 ns. The acceleration process went through a one minute cycle: 40 seconds were spent filling the Tevatron with 800 GeV protons, and then during the remaining 20 seconds the protons were extracted from the Tevatron and routed through the Main Switchyard. The FOCUS experiment was located in Wideband Hall at the end of the proton fixed target line. Data collection within the FOCUS experiment was divided into separate "runs," periods of

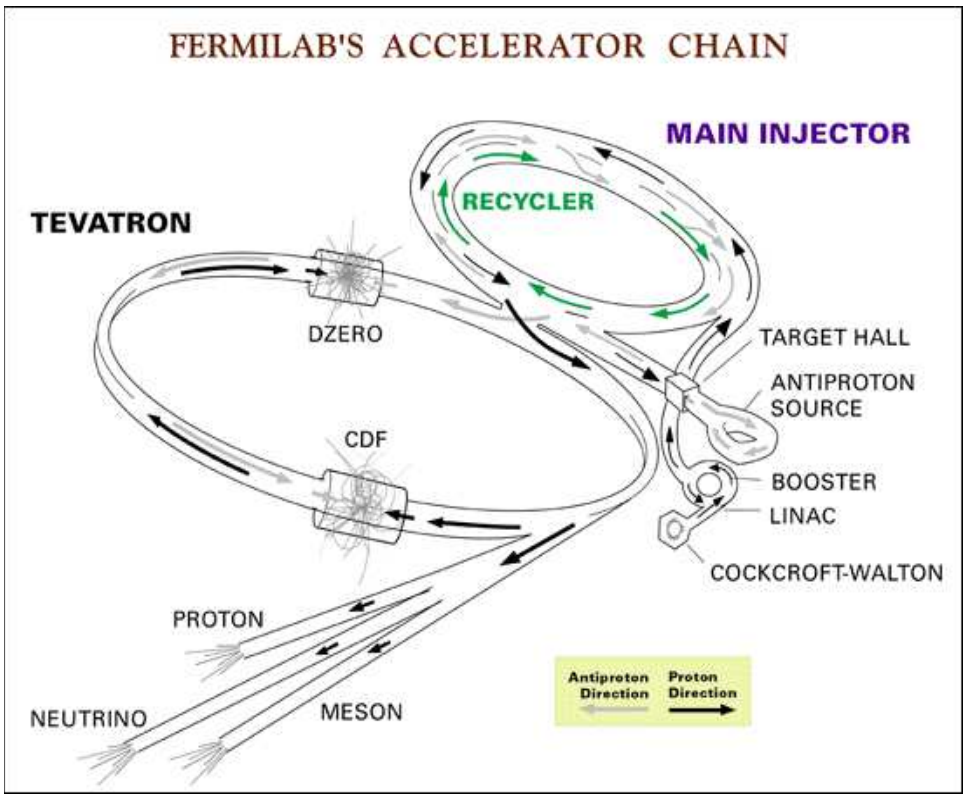

Figure 3.2: A schematic of the layout of the Fermilab accelerator complex.

roughly one hour of running.

3.3 The Photon Beam

Once the 800 GeV protons have been extracted from the Tevatron and sent down the proton fixed target line, the proton beam is converted to a photon beam [23] through a series of stages (see Fig. 3.3). The process begins 365 m upstream of the FOCUS experimental target where the 800 GeV proton beam interacts with the 3.6 meter long liquid deuterium production target. This interaction results in a spray of all varieties of charged and neutral particles. The charged particles are swept away by dipole magnets and collimators, leaving only neutral particles, primarily photons, neutrons, and K_L's. These neutral particles are sent through a lead converter that converts most of the photons in the neutral beam to e^+e^- pairs. The e^+e^- pairs are guided around a thick beam dump using a series of dipole magnets, and the remaining neutral particles in the beam are absorbed by the dump. The series of dipole magnets leading the e^+e^- pairs around the neutral particle dump consists of (1) the Momentum Dispersing Dipoles, the magnets that initially cause electrons to bend one way and positrons the other; (2) the Momentum Selecting Dipoles, which are optimized to select electrons and positrons with momenta around 300 GeV; and (3) the Momentum Recombining Dipoles, the magnets that recombine the electrons and positrons into a single beam. Once around the neutral beam dump, the e^+e^- beam is further focused by the Focusing Quadrupoles.

The e^+e^- beam can now be used to generate a photon beam using the bremsstrahlung process. About 40 m upstream from the FOCUS experimental target, the e^+e^- beam is sent through a lead radiator. The individual electrons and positrons radiate photons through bremsstrahlung. Because of the extremely high energy of the e^+e^- beam of around 300 GeV, the radiated photons travel in a direction nearly identical to the original direction of the e^+e^- beam. After radiating, the electrons and positrons are swept into instrumented beam dumps (the Recoil Positron and Recoil Electron detectors) by the Sweeping Dipoles,

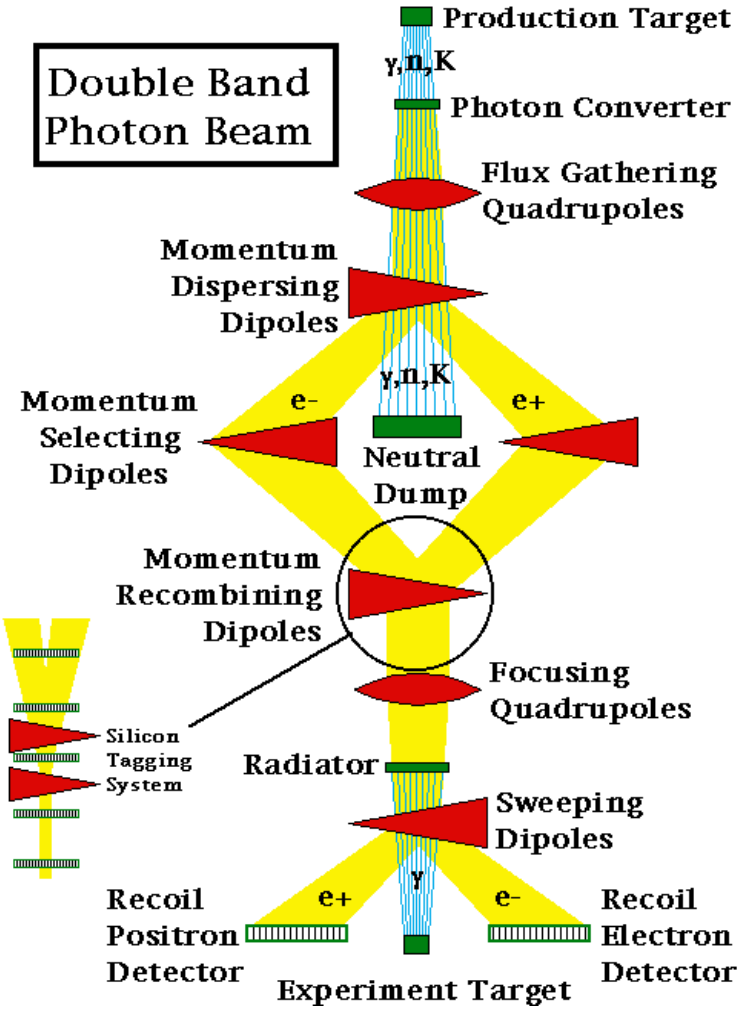

Figure 3.3: Generating the high energy photon beam used by FOCUS.

and only a high energy photon beam remains. The mean photon beam energy is around 150 GeV, but in addition there is a long low energy tail reaching down to around 20 GeV.

The energy of each photon in the beam nominally is measured by the beam tagging system. Before entering the Radiator, the energies of the electrons and positrons are measured by a set of five silicon planes interspersed between the Recombining Dipoles. After passing through the Radiator, when the electrons and positrons are swept to opposite sides of the experimental target, their energies are again measured, this time by lead-glass calorimeters, the Recoil Electron and Recoil Positron detectors. The energy of the radiated beam photon is then just the difference in energy of the electron (or positron) before and after the Radiator. In the case of a multiple bremsstrahlung event, the energy of the extra noninteracting photons is measured by a small central calorimeter, the Beam Gamma Monitor, and this energy is subtracted from the original measurement. In other words, the tagged photon beam energy (E_{BEAM}) is calculated from:

$$E_{BEAM} = E_{INC} - E_{OUT} - E_{BGM}, \tag{3.1}$$

where E_{INC} is the incident electron (positron) energy before radiating, E_{OUT} is the electron (positron) energy after radiating, and E_{BGM} is the energy of any additional photons produced in a multiple bremsstrahlung event. The energy resolution of the beam tagging system is approximately 16 GeV.

3.4 The Spectrometer

The FOCUS detector, building upon the previous E687 photoproduction experiment [22], is a forward multi-particle spectrometer designed to measure the interactions of high energy photons on a segmented BeO target (see Fig. 3.4). BeO was chosen as the target material to maximize the ratio of hadronic to electromagnetic interactions. The target was segmented into four sections to allow for a majority of charmed particles to decay outside of the target material.

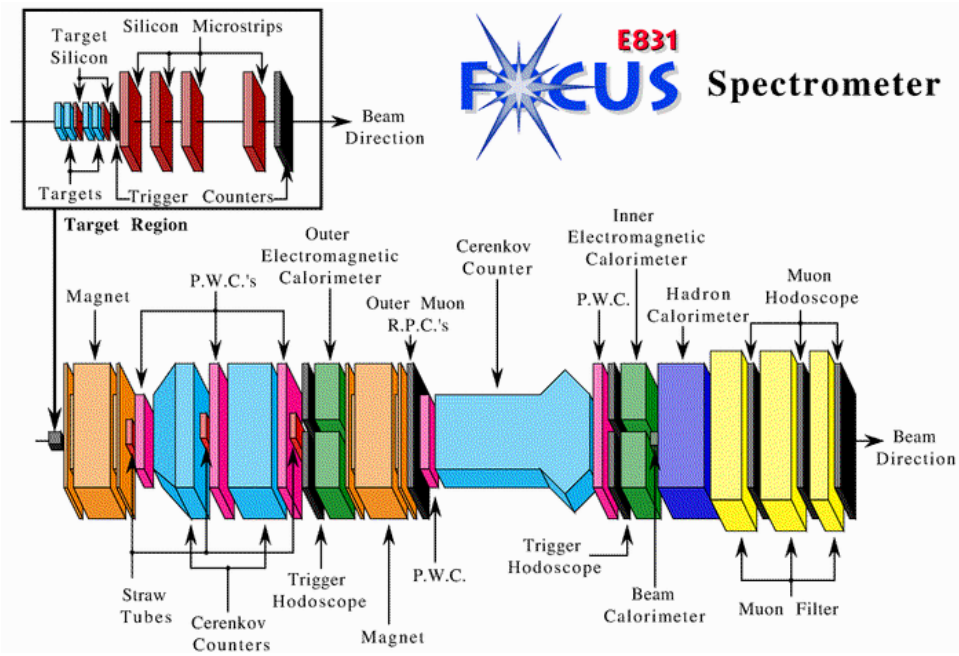

Figure 3.4: The FOCUS spectrometer.

Charged particles emerging from the target region are first tracked by two systems of silicon strip detectors. The upstream system, consisting of four planes (two stations of two views), is interleaved with the experimental target, while the other system lies downstream of the target and consists of twelve planes of microstrips arranged in three views. Once this initial stage of precision tracking is complete, the momentum of a charged particle is determined by measuring its deflections in two analysis magnets of opposite polarity with five stations of multiwire proportional chambers. The measured momentum is used in conjunction with three multicell threshold Čerenkov counters to discriminate between pions, kaons, and protons.

In addition to excellent tracking and particle identification of charged particles, the FOCUS detector provides good reconstruction capabilities for neutral particles. K_S^0's are reconstructed using the "one-bend" approximation described in Ref. [24]. Photons and π^0 are reconstructed using two electromagnetic calorimeters covering different regions of rapidity.

Three elements of the FOCUS detector are most important for the analysis of the charm decay $D^0 \to K^-\pi^+$ which we use to search for CPT violation. First, the tracking system provides a list of charged tracks and their momenta. Second, the particle identification system classifies the charged tracks as pions, kaons, or protons. Third, the triggering elements require that events satisfy a certain number of requirements before they are recorded. Further information on other detector elements (e.g., the calorimeters) can be found elsewhere [25, 26].

3.4.1 Tracking

The purpose of the tracking system is both to reconstruct the paths particles have traveled through the spectrometer and to measure the momenta of these particles. The first task is accomplished by a series of detecting planes normal to the beam direction and placed at advantageous positions throughout the spectrometer. Each plane consists of an array of parallel silicon strips or wires, depending on the detector type, which send out a signal when

a charged (ionizing) particle passes through a silicon plane or close by a wire. Knowing which wire or strip a particle has passed near or through provides a one-dimensional coordinate of the position of the particle on the detecting plane. By grouping planes at various tilts, or views (see Fig. 3.5), into stations, an (x, y) coordinate can be calculated at various positions of z, where z is the distance from the target, and x and y are horizontal and vertical coordinates, respectively. Connecting the (x, y) coordinates from station to station (z position to z position) results in a track, the path a charged particle has followed through the spectrometer.

The second task, measuring a track's momentum, is accomplished by observing the deflections of the charged particle in known magnetic fields. In FOCUS, this is accomplished by using two different large aperture dipole magnets. The first magnet (M1) provides a vertical momentum kick of 0.5 GeV/c, while the second magnet (M2) provides a larger vertical momentum kick of 0.85 GeV/c in the opposite direction. Having different strengths for the two magnets allows sensitivity to a larger range of momentum. A low momentum track will be measured well by M1, but may be bent out of the acceptance by M2. A high momentum track may not be deflected enough by M1 for a good momentum measurement, but will be picked up by the stronger M2. The momentum of a track is calculated by using

$$p = \frac{Kick}{\Delta S} \tag{3.2}$$

as the track passes through either magnet, where $Kick$ is the constant momentum kick of one of the magnets and ΔS is the change in vertical slope of the track as it passes through that magnet.

The FOCUS tracking system consists of several distinct subsystems. The upstream system consists of silicon strip detectors placed among the target elements (referred to as the target silicon system [27]) and silicon strip detectors placed just downstream of the target region (referred to as the SSD system). Charged tracks are followed through the two dipole magnets by the downstream tracking system, which consists of five stations of proportional wire chambers (PWC). Three stations of PWC are between M1 and M2, and

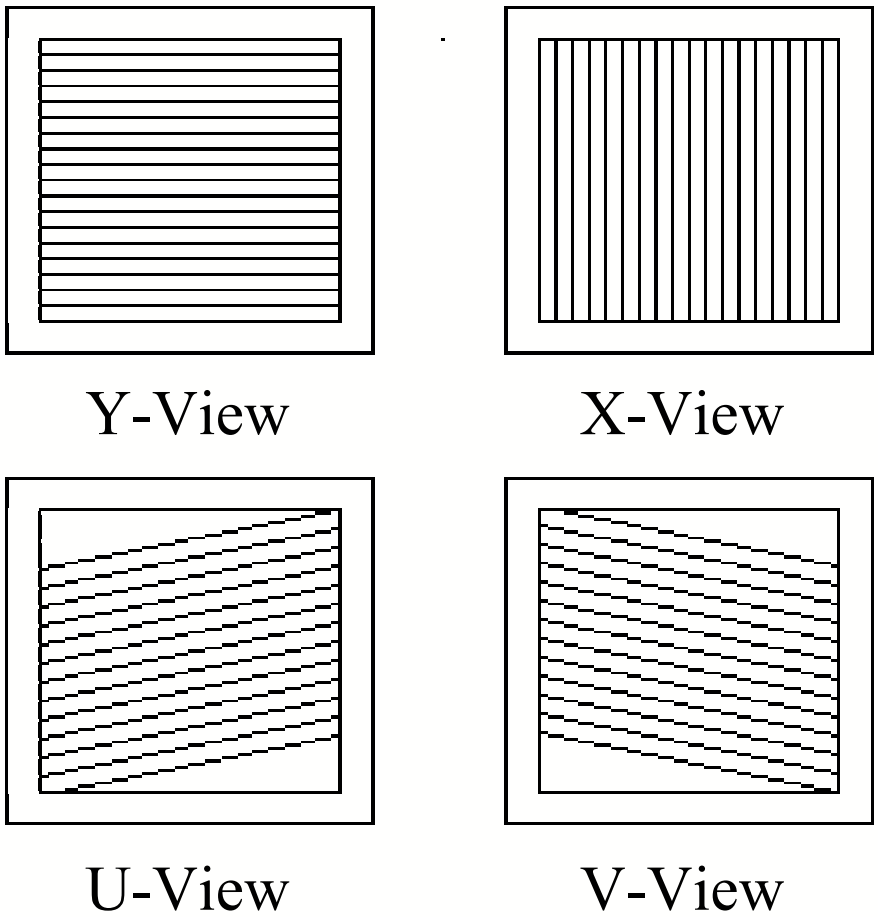

Figure 3.5: A rough sketch of the different PWC views. Charged particles passing through these planes ionize the gas around one of the wires, the charge is collected on the nearest wire, and then recorded, giving a one-dimensional coordinate of the particle. Combining views, the (x, y) position of a particle can be calculated at a given value of z.

two are downstream of M2.

The silicon strip detectors in the upstream system are essentially reverse-biased diodes with charge collecting strips etched on the surface. When a charged particle passes through the interior of the silicon, electron-hole pairs are created. The internal electric field pulls the freed electrons to the surface of the silicon where they are picked up by the conducting strip, amplified, and registered in the data acquisition system.

The target silicon system, the silicon strip system placed among the target elements, is composed of two stations of two planes of silicon strip detectors with strips oriented at $\pm 45°$ from the horizontal. The first station is between the second and third target elements, and the second station follows immediately after the last target element (see Fig. 3.4). The planes are 25×50 mm in size (the larger dimension is vertical), and the strips have a width of $25\,\mu$m, giving 1024 different channels per plane.

The SSD system, the second system of silicon strip detectors, begins just downstream of the target system and extends downstream approximately 30 cm, still upstream of the first dipole magnet. It consists of four stations of three planes each with the silicon strips oriented vertically, and $\pm 45°$ from the horizontal. The stations are each 6 cm apart except for the last, which is separated by 12 cm. The first station (i.e., the most upstream) consists of 25 mm long strips. In the central region the strips are $25\,\mu$m wide and in the outer region the strips are $50\,\mu$m wide. The other stations consist of 50 mm long strips, with widths of $50\,\mu$m in the central region and $100\,\mu$m in the outer.

Tracks in the upstream tracking system are found in three steps. First, clusters are formed within each plane. That is, regions where adjacent strips have fired are grouped together. By measuring the amount of charge collected, the cluster is forced to be consistent with having been formed by a single charged track. Second, projections are formed within each station. In other words, clusters within planes are joined to form a very short track segment within a station. Finally, tracks are formed by connecting the station projections. The last step is accomplished by fitting different combinations of station projections with straight lines and taking the best fits to be the tracks.

The downstream tracking system is composed of five stations of proportional wire chambers (PWC). A PWC operates on roughly the same principle as a silicon strip detector. When a charged particle passes through a PWC, the PWC gas is ionized and the ions drift through an electric field and are collected by parallel metal wires. The charge is collected at the end of a wire giving the one-dimensional position of a track. Arranging the PWC planes within a station at various tilts, or views, gives an (x, y) coordinate for a PWC station.

Five stations of four PWC planes each are interspersed throughout the FOCUS spectrometer. The planes within a station are oriented vertically, horizontally, and at $\pm 11.3°$ from the horizontal. The first three stations (most upstream) are placed between the magnets M1 and M2, and the last two stations appear downstream of M2 on either side of the last Čerenkov counter (C3). The first and fourth stations have the dimensions of 76×127 cm and have a wire spacing of 2 mm. The second, third, and fifth stations are 152×229 cm and have a wire spacing of 3.3 mm.

Tracks in the downstream system are reconstructed in three steps. First, hits in the planes with vertical strips are connected from station to station with straight lines, referred to as x view tracks. The line segments formed from hits in this view are straight since it is the projection unaffected by the magnetic field, i.e., it is the non-bend view. Second, the other three views (the horizontal wires, and $\pm 11.3°$ wires) are combined within each station to form short projections. Finally, the x-view tracks and station projections are combined by fitting to two straight lines, one before M2 and one after, and with a bend parameter to take into account the track's bending through M2.

Once tracks have been found in the upstream and downstream tracking systems, they must be linked together. This is accomplished by refitting all the hits of the upstream and downstream tracks with three straight lines and two bend parameters corresponding to the amount of deflection resulting from M1 and M2. With two opportunities to measure the momentum, tracks can be linked by enforcing consistency. Doubly linked tracks, where one upstream track is linked with two downstream tracks, are allowed to accommodate the possibility of photons converting to e^+e^- pairs that do not significantly separate until after

M1.

The momentum resolution for charged tracks depends on the momentum of the track and whether the track has passed through M1 and M2 or just M1. For tracks only deflected by M1, the resolution is given by:

$$\frac{\sigma_p}{p} = 0.034 \cdot \frac{p}{100\,\mathrm{GeV}/c}\sqrt{1 + (\frac{17\,\mathrm{GeV}/c}{p})^2}. \tag{3.3}$$

For tracks extending through M2 the momentum resolution is:

$$\frac{\sigma_p}{p} = 0.014 \cdot \frac{p}{100\,\mathrm{GeV}/c}\sqrt{1 + (\frac{23\,\mathrm{GeV}/c}{p})^2}. \tag{3.4}$$

For low momentum tracks, the momentum resolution is limited by multiple scattering within the detector material. The momentum resolution for high momentum tracks is limited by the spacing of the wires and strips and uncertainties in the alignment of the detector planes.

3.4.2 Particle Identification

Particle identification in FOCUS is provided by a series of three Čerenkov counters, which are based on the principle that when a particle travels through a medium with a velocity greater than c/n, where c is the speed of light in vacuum and n is the index of refraction of the medium, then the particle will radiate photons. Being sensitive to these radiated photons, a Čerenkov counter can determine whether or not the velocity of a particle is above or below the velocity threshold, c/n. This velocity threshold corresponds to different momenta thresholds for particles of different masses[2], and this is what allows a Čerenkov counter to distinguish between particle types. For example, if the velocity threshold of a Čerenkov counter were $0.9999\,c$, then the momentum threshold for a pion would be $9.87\,\mathrm{GeV}/c$, while the momentum threshold for a kaon would be $34.9\,\mathrm{GeV}/c$. So, if a track had a momentum of $20\,\mathrm{GeV}/c$, as determined by the tracking system, then the Čerenkov counter would fire

[2]The momentum of a particle, p, is given by $p = \gamma m v$, where m is the mass of the particle, v is the velocity and $\gamma = (1 - \frac{v^2}{c^2})^{-1/2}$.

Table 3.1: Properties of the three FOCUS Čerenkov detectors.

Counter	Material	$\pi^{\pm}$ Threshold GeV/c	$K^{\pm}$ Threshold GeV/c	$p^{\pm}$ Threshold GeV/c
C1	80% He, 20% N_2	8.4	29.8	56.5
C2	N_2O	4.5	16.0	30.9
C3	He	17.4	61.8	117.0

if the track were a pion, but would not fire if the track were a kaon. In this particular example, the Čerenkov counter ideally could cleanly distinguish between pions and kaons for all tracks with momenta between 9.87 and 34.9 GeV/c.

By using three different Čerenkov counters filled with gases of different indices of refraction (see Table 3.1), FOCUS can cleanly distinguish between pions, kaons, and protons over a wide range of momentum. Now, for example, a 20 GeV/c pion, a 20 GeV/c kaon, and a 20 GeV/c proton will all have different signatures. The pion will fire all three counters C1, C2, and C3; the kaon will only fire C2; and the proton will not radiate at all. Notice that there is ideally a clean separation between pions and kaons with momenta all the way from 4.5 GeV/c to 61.8 GeV/c. E687 used a particle identification system based only on these thresholds and logic tables.

FOCUS has improved on this system by measuring the angle with which photons are radiated by a particle traveling with a velocity above threshold. This provides additional information about the particle's velocity, v, since the angle of radiation, θ, is given by

$$\cos\theta = \frac{c}{nv}. \tag{3.5}$$

Therefore the higher the velocity is above threshold, the larger the ring of the emitted photons. The measurement of the angle has been made possible by dividing the back of the Čerenkov counters into arrays of cells, with smaller cells near the center of the counter and larger cells further out from the center.

FOCUS has implemented a system called CITADL for particle identification based on the detected rings in the counters [28]. The CITADL system works by assigning likelihoods

to different particle hypotheses. For example, if a particle of given momentum (measured by the tracking system) were a pion, then we can calculate its velocity and the angles of radiation and thus know which cells in which counters should have fired. The likelihood for the pion hypothesis is then calculated based on the status of these cells. If a given cell should be "on" given the pion hypothesis, and the cell was found to be "on", then the total likelihood for the pion hypothesis receives a contribution of

$$L_{\text{cell}} = (1 - e^{-\mu}) + a - a(1 - e^{-\mu}), \tag{3.6}$$

where μ is the expected number of photoelectrons in the cell, a is the accidental firing rate, and Poisson statistics has been assumed. If the cell was found to be "off", then the total likelihood receives a contribution of

$$L_{\text{cell}} = 1 - [(1 - e^{-\mu}) + a - a(1 - e^{-\mu})]. \tag{3.7}$$

The likelihoods are summed over all the cells in the ring of cells that should have fired given the pion hypothesis to give a total likelihood for the pion hypothesis:

$$L_{\pi} = \sum_{\text{cells}} L_{\text{cell}}. \tag{3.8}$$

Similarly, likelihoods are calculated for the $e^{\pm}$, $K^{\pm}$, and $p^{\pm}$ particle hypotheses.

To convert the likelihoods to χ^2-like measures, the CITADL system introduces the variables

$$W_i = -2\ln(L_i), \tag{3.9}$$

where i indicates the hypothesis under consideration, i.e., either e^+e^-, $\pi^{\pm}$, $K^{\pm}$, or $p^{\pm}$. The W_i with the lowest value indicates the most likely particle hypothesis. Since kaons and pions dominate the hadronic final states, useful parameters for particle identification are the "pionicity", defined as

$$\text{Pionicity} \equiv W_K - W_{\pi}, \tag{3.10}$$

and the "kaonicity", defined as

$$\text{kaonicity} \equiv W_\pi - W_K. \tag{3.11}$$

Increasing the "kaonicity" requirement, for example, decreases the chances a pion will be misidentified as a kaon.

3.4.3 Triggers

Whenever an interesting event occurs in the detector, data must be read out and stored. The trigger system is responsible for discriminating between interesting and uninteresting events. The trigger decision takes place in several stages and there are several different triggers based on different physics questions. The data for the $K^-\pi^+$ analyses included in the remaining chapters are obtained through the hadronic trigger. While triggering elements are located throughout the spectrometer and serve various purposes, the hadronic trigger imposes only three simple criteria on events.

First, like all other triggers, the hadronic trigger requires a coincidence in TR1 and TR2. TR1 is just downstream of the target assembly, and TR2 is just downstream of the SSD system. A coincidence in TR1 and TR2 guarantees that at least one charged track has passed through the SSD system.

Second, in addition to having tracks in the SSD system, the hadronic trigger requires at least two charged tracks to traverse the entire downstream tracking system. The OH and H$\times$V detectors are located just after the last PWC station and are designed to count charged tracks. The H$\times$V detector covers the inner region of the acceptance and the OH detector covers the outer region. The hadronic trigger requires either two charged tracks be detected by the H$\times$V or one charged track register in the H$\times$V and one in the OH. Both the H$\times$V and the OH include a vertical gap from top to bottom to allow e^+e^- pairs to pass.

Finally, a minimum hadronic energy of 18 GeV as determined by the hadronic calorimeter is an additional requirement imposed by the hadronic trigger. This requirement ensures the presence of hadronic tracks (as opposed to e^+e^- tracks).

3.5 Data Collection

Over the course of its running, the FOCUS experiment collected 6.5 billion events recorded on 5926 tapes, each tape holding 4.5 Gigabytes of data. The data was collected over approximately 6500 runs, each run corresponding to roughly one hour of running time. The data was processed in four separate stages.

(1) PassOne was where all the major reconstruction was performed, e.g., track reconstruction and particle identification.

(2) Skim1 separated the PassOne output into six large superstreams based on different physics criteria. One of the superstreems was the hadronic meson decays also called as "SEZDEE" (Super EaZy DEE) stream. This stream included all hadronic decays of D mesons. This stream was still large (approximately 300 8mm tapes, 1.2 TB worth of data).

(3) In Skim2, the superstreams were separated into separate substreams by requiring more specific physics criteria. One of the substreams of SEZDEE was tuned to select $D^0 \to K^-\pi^+$ decays by requiring that the invariant mass of $K^-\pi^+$ is between 1.7 GeV and 2.1 GeV, have a decay length significance greater than 2.5, and a confidence level of secondary vertex greater than 1%. After these cuts the data was reduced to a size of ≈ 63 GB.

(4) In the final stage, the $K^-\pi^+$ data was copied to the local disks at one of the Indiana University High Energy Physics clusters.

Chapter 4

Data Analysis

In this thesis we investigate the current experimental sensitivity for a CPT-violating signal using data collected by the FOCUS Collaboration during the 1996–97 fixed-target run at Fermilab. The analysis is also described in a journal publication [18].

4.1 Analysis Aproach

The data analysis is as follows. We analyze the two right-sign hadronic decays $D^0 \to K^-\pi^+$ and $\bar{D}^0 \to K^+\pi^-$. We use the soft pion from the decay $D^{*+} \to D^0\pi^+$ to tag the flavor of the D at production, and the kaon charge in the decay $D^0 \to K^-\pi^+$ to tag the D flavor at the time of decay. (Charge conjugate modes are assumed throughout this thesis.)

4.2 Analysis Cuts

$D^0 \to K^-\pi^+$ events were selected by requiring a minimum detachment of the secondary (decay) vertex from the primary (production) vertex of $5\sigma_L$. σ_L is the decay length error. The primary vertex was found using a candidate driven vertex finder which nucleated tracks about a "seed" track constructed using the secondary vertex and the reconstructed D momentum vector. Both primary and secondary vertices were required to have confidence level fits of greater than 1%. The D^*-tag is accomplished by requiring the $D^* - D^0$ mass difference to be less than 3 MeV/c^2 of the nominal value [29].

Kaons and pions were identified using the Čerenkov particle identification cuts. These cuts are based on likelihood ratios between the various stable particle hypotheses, and are computed for a given track from the observed firing response ("on" or "off") of all cells within the track's ($\beta = 1$) Čerenkov light cone in each of three multi-cell, threshold Čerenkov counters as described earlier. The product of all firing probabilities for all cells within the three Čerenkov cones produces a χ^2-like variable called $W_i \equiv -2\times\log(\text{likelihood})$ where i ranges over electron, pion, kaon and proton hypotheses. For the K and the π candidates, we require W_i to be no more than 4 greater than the smallest of the other three hypotheses ($W_i - W_{min} < 4$) which eliminated candidates that are highly to have been misidentified. In addition, D^0 daughters must satisfy the slightly stronger $K\pi$ separation criteria $W_\pi - W_K > 0.5$ for the K and $W_K - W_\pi > -2$ for the π. Doubly misidentified $D^0 \to K^-\pi^+$ candidates are removed by imposing a hard Čerenkov cut on the sum of the two separations ($(W_\pi - W_K)_K + (W_K - W_\pi)_\pi > 8$). Primary vertices that lie in the TR1 region are poorly reconstructed so we exclude events in TR1, by imposing the z coordinate of the primary vertex < 2 cm. Fig. 4.1 shows the invariant mass distribution for the two D^*-tagged, right-sign decays $D^0 \to K^-\pi^+$ and $\bar{D}^0 \to K^+\pi^-$. Fig. 4.2 shows the invariant mass distributions for right-sign decays split up into particle and antiparticle. A fit to the mass distribution is carried out using a Gaussian function to describe the signal and a second-order polynomial for the background. The fit yields $17\,227 \pm 144$ D^0 and $18\,463 \pm 151$ $\bar{D}^0$ signal events.

Fig. 4.3 shows the primary and secondary vertices for D^0's for the run period 6 which has 4 target segments interwoven with target silicons. Most of the primary vertices lie within the target segments and some in the target silicons. The contours of the target segments and target silicons can be seen. About 60% of D^0 decays occur outside of target segments.

The reduced proper time is a traditional lifetime variable used in fixed-target experiments that uses the detachment between the primary and secondary vertex as the principal tool in reducing non-charm background. The reduced proper time is defined by

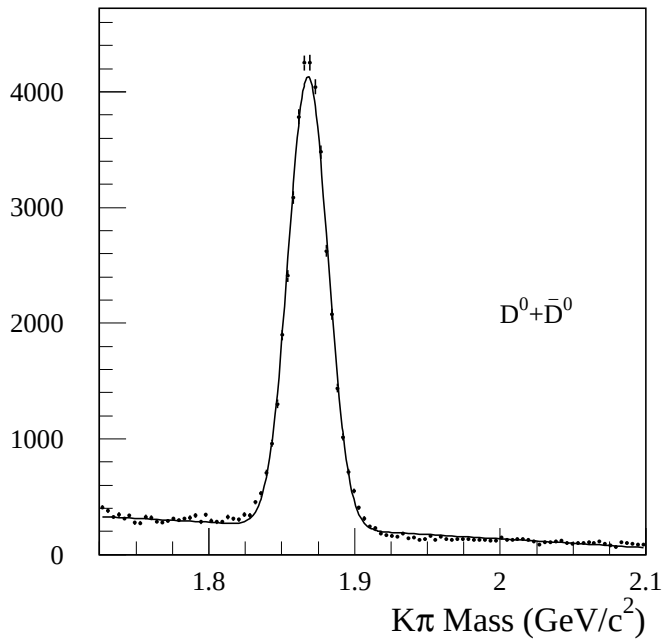

Figure 4.1: Invariant mass distribution for the sum of D^0 and $\overline{D}^0$ right-sign decay candidates.

$t' = (\ell - N\sigma_\ell)/(\beta\gamma c)$ where ℓ is the distance between the primary and secondary vertex, σ_ℓ is the resolution on ℓ, and N is the minimum detachment cut required to tag the charmed particle through its lifetime. Fig. 4.4 shows reduced proper time distributions for the two right-sign decays: $D^0 \to K^-\pi^+$ and $\bar{D}^0 \to K^+\pi^-$.

Table 4.1 shows a summary of the fits for $D^0 \to K^-\pi^+$ and $\bar{D}^0 \to K^+\pi^-$. It gives us an overall picture of yields, signal to background ratios, masses and lifetimes.[1] The above cuts have been chosen to maximize the signal to background ratio.

It is useful to know how how the signal to background ratio is distributed in bins of reduced proper time. We denote S_i as the amount of signal in bin i and B_i the amount of background in the same bin. When we apply sideband subtraction, each event carries a

[1] From a simple exponential fit.

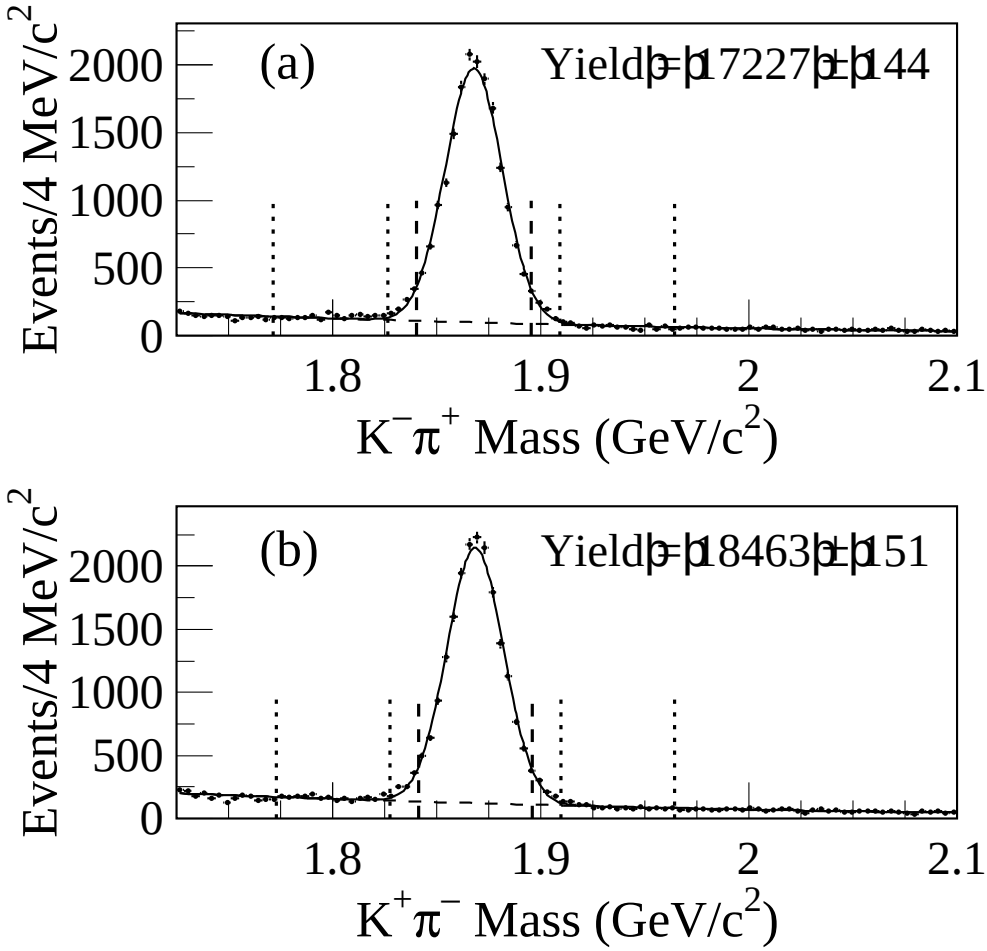

Figure 4.2: Invariant mass of (a) $D^0 \to K^-\pi^+$ and (b) $\bar{D}^0 \to K^+\pi^-$ for data (points) fitted with a Gaussian signal and quadratic background (solid line). The vertical dashed lines indicate the signal region, and the vertical dotted lines indicate the sideband region.

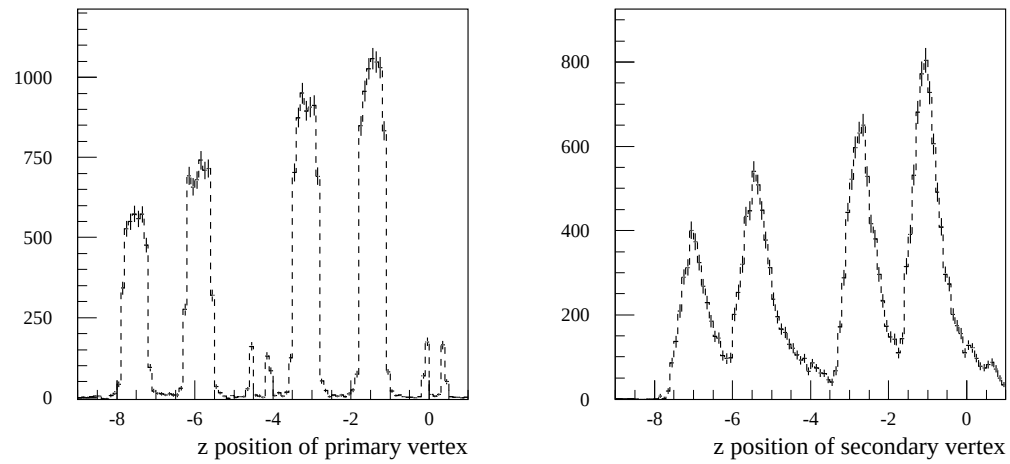

Figure 4.3: (Left) z position of the primary vertex of D's for $runnumber > 9750$ and (right) z position of D's secondary vertices for $runnumber > 9750$. The dashed line is to guide the eye.

Table 4.1: Summary of the fits for $D^0 \to K^-\pi^+$ and $\bar{D}^0 \to K^+\pi^-$.

Parameter	$\overline{D^0}$	D^0	$D^0 + \overline{D^0}$
Yield	18287 ± 235	17085 ± 224	35342 ± 322
S/B	10.24	11.11	10.12
Mass (MeV/c^2)	1868.50 ± 0.11	1867.80 ± 0.11	1868.10 ± 0.08
σ(MeV/c^2)	13.51 ± 0.10	13.63 ± 0.10	13.57 ± 0.07
$\tau(fs)$	412.8 ± 3.8	405.7 ± 3.8	409.6 ± 2.7

weight and thus errors of each bin will depend on signal to background ratio. The smaller this ratio, the larger the errors. When there is only signal then the error is equal to the square root of the bin content. Let's see quantitatively what happens. When the sideband lines are chosen as in Fig. 4.2, we get a formula that connects error with signal to background ratio $err_i = \sqrt{S_i(1 + 1.5 \times B_i/S_i)}$. Based on this formula, we extract signal to background ratio per each bin when we know err_i and S_i. Fig. 4.5 shows the distribution of signal to background ratio in bins of reduced proper time for $\bar{D}^0$ and D^0. Both show that signal to background ratio decreases in large t'. This is due to the fact that contamination from other charm mesons is more likely at larger t' values than for smaller values.

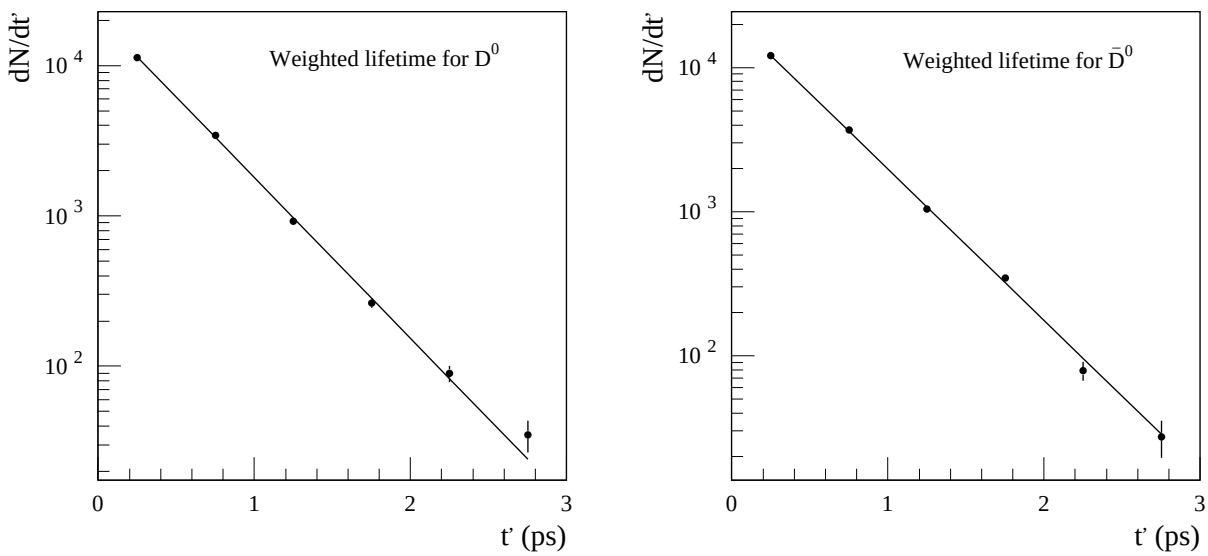

Figure 4.4: Background subtracted reduced proper time distributions for D^0 and $\bar{D}^0$.

4.3 Results for the Asymmetry

We plot the difference in right-sign events between $\bar{D}^0$ and D^0 in bins of reduced proper time t'. The background subtracted yields of right-sign D^0 and $\bar{D}^0$ were extracted by properly weighting the signal region $(-2\sigma, +2\sigma)$, the low mass sideband $(-7\sigma, -3\sigma)$ and high mass sideband $(+3\sigma, +7\sigma)$, where σ is the width of the fitted signal Gaussian. For each data point, these yields were used in forming the ratio:

$$A_{\mathrm{CPT}}(t') = \frac{\overline{Y}(t') - Y(t')\frac{\overline{f}(t')}{f(t')}}{\overline{Y}(t') + Y(t')\frac{\overline{f}(t')}{f(t')}}, \tag{4.1}$$

where $\overline{Y}(t')$ and $Y(t')$ are the yields for $\bar{D}^0$ and D^0 and $\overline{f}(t')$, and $f(t')$ are their respective correction functions. In the absence of detector acceptance corrections, this is equivalent to A_{CPT} as defined in Eqn. 2.21. The functions $\overline{f}(t')$ and $f(t')$ account for geometrical acceptance, detector and reconstruction efficiencies, and the absorption of parent and daughter particles in the nuclear matter of the target. The correction functions are determined using a detailed Monte Carlo (MC) simulation using PYTHIA [31]. The fragmentation is done

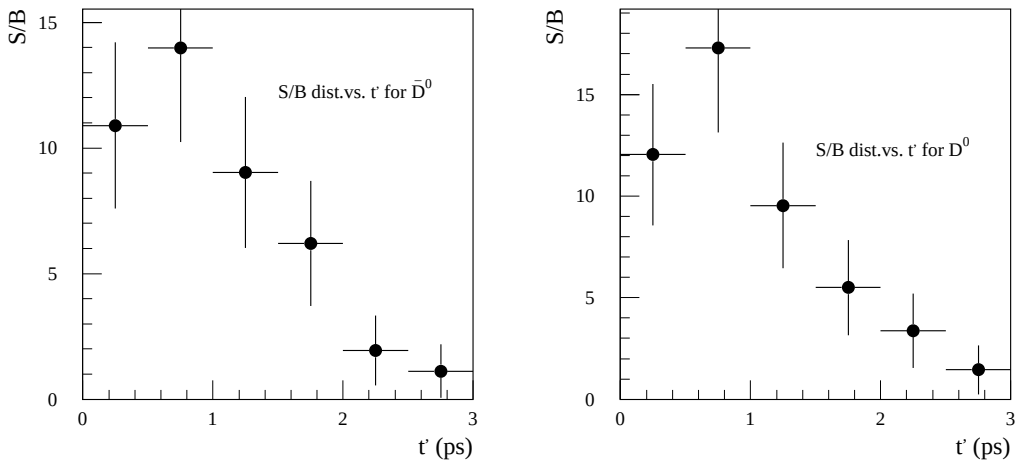

Figure 4.5: $\frac{S}{B}$ in bins of reduced proper time for $\bar{D}^0$ (left) and D^0 (right).

using the Bowler modified Lund string model. PYTHIA was tuned using many production parameters to match various data production variables such as charm momentum and primary multiplicity. The shapes of the $f(t')$ and $\overline{f}(t')$ functions are obtained by dividing the reconstructed MC t' distribution by a pure exponential with the MC generated lifetime. Fig. 4.7 shows these corrections. Detector resolution effects cause less than 8% change in the t' distribution as measured by deviations from a pure exponential decay. The ratio of the correction functions, shown in Fig. 4.6(a), enters explicitly in Eq. 4.1 and its effects on the asymmetry are less than 1.3% compared to when no corrections are applied. Due to the QCD production mechanism for photoproduced charm mesons, more $\bar{D}^0$ than D^0 are produced in the FOCUS data sample. This has been previously investigated in photoproduction by E687, in which the production asymmetries were studied in the context of a string fragmentation model [30]. The effect on the A_{CPT} distribution is to add a constant, production-related offset, which is accounted for in the fit.

The A_{CPT} data in Fig. 4.6(b) are fit to a line using the form of Eq. 2.26 plus a constant offset. The allowed fit parameters are a constant production asymmetry parameter α and $\mathrm{Re}\,\xi\ y - \mathrm{Im}\,\xi\ x$. The value of Γ used in the fit is taken as $\Gamma = 1.6 \times 10^{-12}$ GeV [29]. The

result of the fit is:

$$\mathrm{Re}\,\xi\ y - \mathrm{Im}\,\xi\ x = 0.0083 \pm 0.0065. \tag{4.2}$$

We also report α for completeness:

$$\alpha = 0.026 \pm 0.009. \tag{4.3}$$

If one assumes mixing parameter x, y values of 5%(current 95% C.L. upper limits) and Im $\xi = 0$, one obtains for Re ξ, Re$\xi = 0.17 \pm 0.13$. We infer one standard deviation errors on Re ξ of 0.13, and 95% confidence level upper bounds of 0.26.

4.4 Results for Coefficients of Lorentz Violation

Any CPT and Lorentz violation within the Standard Model can be described by the SME proposed by Kostelecký *et al.* [19]. In quantum field theory, the CPT-violating parameter ξ must generically depend on lab momentum, spatial orientation, and sidereal time [6, 20]. The SME can be used to show that Lorentz violation in the D system is controlled by the four vector Δa_μ. The precession of the experiment with the earth relative to the spatial vector $\vec{\Delta a}$ would modulate the signal for CPT violation, thus making it possible to separate the components of Δa_μ. The coefficients for Lorentz violation depend on the flavor of the valence quark states and are model independent. In the case of FOCUS, where D^0 mesons in the lab frame are highly collimated in the forward direction and under the assumption that D^0 mesons are uncorrelated, the ξ parameter assumes the following form [6] outlined earlier:

$$\xi(\hat{t}, p) \quad = \quad \frac{\gamma(p)}{\Delta\lambda}[\Delta a_0 + \beta\Delta a_Z \cos\chi + \beta \sin\chi(\Delta a_Y \sin\Omega\hat{t} + \Delta a_X \cos\Omega\hat{t})]. \tag{4.4}$$

Ω and $\hat{t}$ are the sidereal frequency and time respectively, X, Y, Z are non-rotating coordinates with Z aligned along the Earth's rotation axis, $\Delta\lambda = \Gamma(x - iy)$, and $\gamma(p) = \sqrt{1 + p^2_{D^0}/m^2_{D^0}}$.

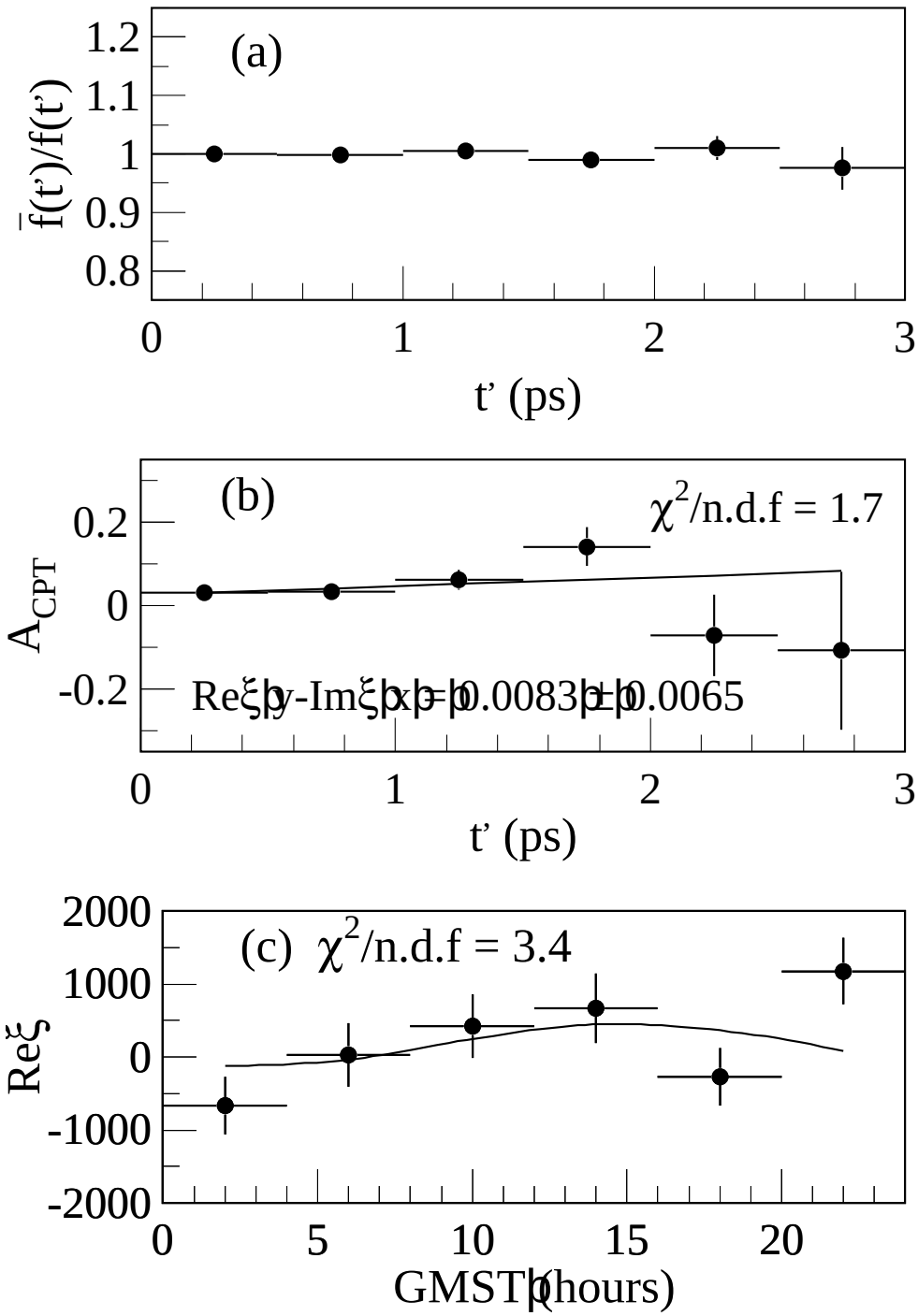

Figure 4.6: (a) The ratio of the corrections, and (b) A_{CPT} as a function of reduced proper time. The data points represent the A_{CPT} as given in Eq. 4.1 and the solid line represent the fit given in functional form by Eq. 2.22: (c) $\mathrm{Re}\,\xi$ as a function of Greenwich Mean Sidereal Time (GMST).

Binning in sidereal time $\hat{t}$ is very useful because it provides sensitivity to components Δa_X and Δa_Y. Since Eq. 15 of Ref. [6] translates into $\mathrm{Re}\,\xi\, y - \mathrm{Im}\,\xi\, x = 0$, setting limits on the coefficients of Lorentz violation requires expanding the asymmetry in Eq. 2.21 to higher (non-vanishing) terms. In addition, the interference term of right-sign decays with DCS decays must also be included since it gives a comparable contribution. One can follow the procedure given by equations [16] to [20] of Ref. [6] where the basic transition amplitudes $\langle f|T|\overline{P^0}\rangle$ and $\langle \overline{f}|T|P^0\rangle$ are not zero but are DCS amplitudes. After Taylor expansion the asymmetry can be written as:

$$A_{\mathrm{CPT}} = \frac{\mathrm{Re}\,\xi(x^2+y^2)(t/\tau)^2}{2x}\left[\frac{xy}{3}(t/\tau) + \sqrt{R_{\mathrm{DCS}}}\,(x\,\cos\delta + y\,\sin\delta)\right], \tag{4.5}$$

where R_{DCS} is the branching ratio of DCS relative to right-sign decays and δ is the strong phase between the DCS and right-sign amplitudes. We searched for a sidereal time dependence by dividing our data sample into four-hour bins in Greenwich Mean Sidereal Time (GMST) [21], where for each bin we repeated our fit in t' using the asymmetry given by Eq. 4.5 and extracted $\mathrm{Re}\,\xi$. The resulting distribution, shown in Fig. 4.6(c), was fit using Eq. 4.4 and the results for the expressions involving coefficients of Lorentz violation in the SME were:

$$C_{0Z} \equiv N(x,y,\delta)(\Delta a_0 + 0.6\,\Delta a_Z) = (1.0 \pm 1.1)\times 10^{-16}\ \mathrm{GeV}, \tag{4.6}$$

$$C_X \equiv N(x,y,\delta)\Delta a_X = (-1.6 \pm 2.0)\times 10^{-16}\ \mathrm{GeV}, \tag{4.7}$$

and

$$C_Y \equiv N(x,y,\delta)\Delta a_Y = (-1.6 \pm 2.0)\times 10^{-16}\ \mathrm{GeV}, \tag{4.8}$$

where $N(x,y,\delta) = [xy/3 + 0.06\,(x\,\cos\delta + y\,\sin\delta)]$ is the normalization factor. The angle between the FOCUS spectrometer axis and the Earth's rotation axis is approximately $\chi = 53^\circ$ ($\cos\chi = 0.6$). We average over all D^0 momentum so $\langle\gamma(p)\rangle \approx \gamma(\langle p\rangle) = 39$ and $\beta \approx$

1. We also compare with the previous measurements for the kaon r_K and B meson r_B by constructing a similar quantity r_D [8], $r_D = |\Delta\Lambda|/m_{D^0} = \beta^\mu \Delta a_\mu / m_{D^0} = |\overline{\xi}||\Delta\lambda| = \gamma(p)|\Delta a_0 + 0.6\,\Delta a_Z|/m_{D^0}$. The result for $N(x,y,\delta)\,r_D$ is:

$$N(x,y,\delta)\,r_D = (2.3 \pm 2.3) \times 10^{-16}\ \text{GeV}. \tag{4.9}$$

Although it may seem natural to report r_D, the parameter r_D (and r_K, r_B) has a serious defect: in quantum field theory, its value changes with the experiment. This is because it is a combination of the parameters Δa_μ with coefficients controlled by the D^0 meson energy and direction of motion. The sensitivity would have been best if $\chi = 90°$.

4.5 Monte Carlo

To understand the corrections, we analyzed simulated Monte Carlo events. Our Monte Carlo simulation includes the PYTHIA Model for photon gluon fusion and incorporates a complete simulation of all detectors and trigger systems, with known multiple scattering and absorption effects. The default Monte Carlo flag which is responsible for scattering and absorption effects include a simulation of D^0 and $\bar{D}^0$ cross sections set at half the cross section for a pion. The Monte Carlo was prepared such that after trigger requirement and analysis cuts as in the data, we reconstruct 50 times the data statistics. Fig. 4.7 shows the corrections $f(t')$ for D^0, $\bar{D}^0$, D^0+$\bar{D}^0$ and the ratio of $\frac{\bar{D}^0}{D^0}$. The deviations are less than 8% for individual $f(t')$. Furthermore they cancel out when we take the ratio (of the order of 1.3%) $\frac{\bar{f(t')}}{f(t')}$. The ratio is the only combination used when we form the asymmetry, so our detector corrections on the asymmetry are very small.

Fig. 4.8 shows the asymmetry in Monte Carlo by fitting it with the function in Eq. 2.22. There is enough data statistics in the Monte Carlo sample to demonstrate that there is no slope in the asymmetry, i.e., only a small value of $Re\xi = -0.0003 \pm 0.0210$, consistent with zero, could result from these corrections. Thus a significant slope in observed real

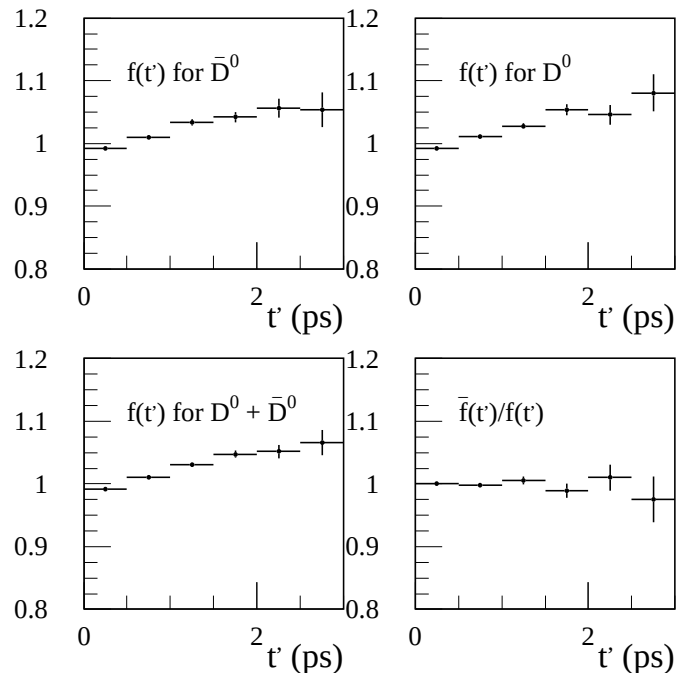

Figure 4.7: $f(t')$ corrections and their ratio for D^0 and $\bar{D}^0$.

data should be attributed to CPT. The D^0, $\overline{D^0}$ production asymmetry in Monte Carlo is $\alpha = 0.052 \pm 0.001$.

4.6 Systematic Uncertainties

Previous analyses have shown that MC absorption corrections are very small [13]. The interactions of pions and kaons with matter have been measured, but no equivalent data exists for charm particles. To check for any systematic effects associated with the fact that the charm particle cross section is unmeasured, we examined several variations of D^0 and $\bar{D}^0$ cross sections. The standard deviation of these variations returns systematic uncertainties of ± 0.0017, $\pm 0.3 \times 10^{-16}$ GeV, $\pm 0.0 \times 10^{-16}$ GeV, and $\pm 0.1 \times 10^{-16}$ GeV to our measurements of $\mathrm{Re}\,\xi\ y - \mathrm{Im}\,\xi\ x$, C_{0Z}, C_X, and C_Y respectively.

We also investigated parent (D^0,$\bar{D}^0$) and daughter (K, π) absorption separately. The study showed that the flat corrections in MC are small, not only because absorption effects

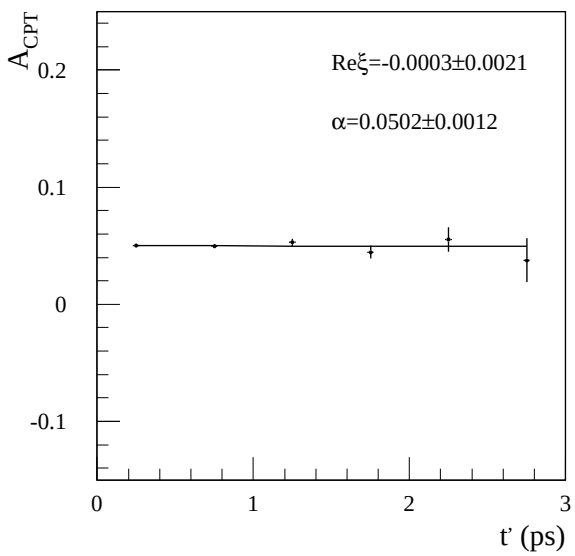

Figure 4.8: Asymmetry in Monte Carlo fitted with Eq. 2.22

are small, but also because of a cancellation due to two competing effects. The D^0 has a slightly higher absorption rate than the $\bar{D}^0$, and the net absorption rate of a (K^-, π^+) from a D^0 is slightly lower than the net absorption rate of a (K^+, π^-) from the $\bar{D}^0$.

In a manner similar to the S-factor method used by the Particle Data group PDG [29], we made eight statistically independent samples of our data to look for systematic effects. We split the data in four momentum ranges and two years. The split in year was done to look for effects associated with target geometry and reconstruction due to the addition of four silicon planes near the targets in January, 1997 [27]. We found no contribution to our measurements of $\mathrm{Re}\,\xi\ y - \mathrm{Im}\,\xi\ x$ and C_{0Z}. The contributions to C_X and C_Y were $\pm 1.3 \times 10^{-16}$ GeV and $\pm 1.6 \times 10^{-16}$ GeV respectively. We also varied the bin widths and the position of the sidebands to assess the validity of the background subtraction method and the stability of the fits. The standard deviation of these variations returns systematic uncertainties of ± 0.0012, $\pm 0.3 \times 10^{-16}$ GeV, $\pm 0.9 \times 10^{-16}$ GeV, and $\pm 0.5 \times 10^{-16}$ GeV to our measurements of $\mathrm{Re}\,\xi\ y - \mathrm{Im}\,\xi\ x$, C_{0Z}, C_X, and C_Y respectively. Finally, to uncover any unexpected systematic uncertainty, we varied our ℓ/σ_ℓ and $W_\pi - W_K$ requirements and the standard deviation of these variations returns systematic uncertainties of ± 0.0036, $\pm 1.5 \times 10^{-16}$ GeV,

Table 4.2: Contributions to the systematic uncertainty.

Contribut.	$\mathrm{Re}\,\xi\, y - \mathrm{Im}\,\xi\, x$	C_X (GeV)	C_{0Z} (GeV)	C_Y (GeV)
Absorption	0.0017	0.0×10^{-16}	0.3×10^{-16}	0.1×10^{-16}
Split sample	0.0000	1.3×10^{-16}	0.0×10^{-16}	1.6×10^{-16}
Fit variant	0.0012	0.9×10^{-16}	0.3×10^{-16}	0.5×10^{-16}
Cut variant	0.0036	1.0×10^{-16}	1.5×10^{-16}	1.1×10^{-16}
Total	**0.0041**	$\mathbf{1.9 \times 10^{-16}}$	$\mathbf{1.6 \times 10^{-16}}$	$\mathbf{2.0 \times 10^{-16}}$

$\pm 1.0 \times 10^{-16}$ GeV, and $\pm 1.1 \times 10^{-16}$ GeV to our measurements of $\mathrm{Re}\,\xi\; y - \mathrm{Im}\,\xi\; x$, C_{0Z}, C_X, and C_Y respectively. Contributions to the systematic uncertainty are summarized in Table 4.2. Taking contributions to be uncorrelated, we obtain a total systematic uncertainty of ± 0.0041 for $\mathrm{Re}\,\xi\, y - \mathrm{Im}\,\xi\, x$, $\pm 1.6 \times 10^{-16}$ GeV for C_{0Z}, $\pm 1.9 \times 10^{-16}$ GeV for C_X, and $\pm 2.0 \times 10^{-16}$ GeV for C_Y.

To see further details on the assessment of systematic errors, see Appendix A.

Chapter 5

Conclusions

We have performed the first search for CPT and Lorentz violation in neutral charm meson oscillations. We have measured:

$$\mathrm{Re}\,\xi\, y - \mathrm{Im}\,\xi\, x = 0.0083 \pm 0.0065 \text{ (stat)} \pm 0.0041 \text{ (syst)}, \tag{5.1}$$

which leads to a 95% confidence level limit of:

$$-0.0068 < (\mathrm{Re}\,\xi\, y - \mathrm{Im}\,\xi\, x) < 0.0234. \tag{5.2}$$

As a specific example, assuming $x = 1\%$ and $\mathrm{Im}\,\xi = 0$ and $y = 1\%$ (current central values for mixing), one finds:

$$\mathrm{Re}\,\xi = 0.83 \pm 0.65 \text{ (stat)} \pm 0.41 \text{ (syst)}, \tag{5.3}$$

with a 95% confidence level limit of

$$-0.68 < \mathrm{Re}\,\xi < 2.34. \tag{5.4}$$

Within the SME, we set three independent first limits on the expressions involving coefficients of Lorentz violation of:

$$(-2.8 < N(x, y, \delta)(\Delta a_0 + 0.6\,\Delta a_Z) < 4.8) \times 10^{-16} \text{ GeV}, \tag{5.5}$$

$$(-7.0 < N(x, y, \delta)\Delta a_X < 3.8) \times 10^{-16} \text{ GeV}, \tag{5.6}$$

and

$$(-7.0 < N(x, y, \delta)\Delta a_Y < 3.8) \times 10^{-16} \text{ GeV}. \tag{5.7}$$

As a specific example, assuming $x = 1\%$, $y = 1\%$ (current central values for mixing) and $\delta = 15°$ (current theoretical prediction) one finds the 95% C.L. limits on the coefficients of Lorentz violation of:

$$(-3.7 < \Delta a_0 + 0.6\,\Delta a_Z < 6.5) \times 10^{-13} \text{ GeV}, \tag{5.8}$$

$$(-9.4 < \Delta a_X < 5.0) \times 10^{-13} \text{ GeV}, \tag{5.9}$$

and

$$(-9.3 < \Delta a_Y < 5.1) \times 10^{-13} \text{ GeV}. \tag{5.10}$$

The measured values are consistent with no significant CPT or Lorentz invariance violation.

Part II

Chapter 6

Introduction to Λ_b^0

The UA1 experiment at CERN announced the discovery of Λ_b^0 baryon in 1991 [32]. They measured the production fraction times branching ratio to be:

$F(\Lambda_b) \times B(\Lambda_b \to J/\psi\Lambda) = (1.8 \pm 1.0) \times 10^{-3}$.

Later on, in 1996 both ALEPH [33] and DELPHI [34] measured the Λ_b^0 mass in the decay $\Lambda_c\pi$. Each experiment found only 4 candidates. Λ_b^0 was unambiguously observed by CDF 110 pb^{-1} Run I data [35] with a mass of 5621 ± 4 (stat) ± 3 (syst) MeV, and a production fraction times branching ratio of

$$F(\Lambda_b) \times B(\Lambda_b J/\psi\Lambda) = (3.7 \pm 1.7 \text{ (stat)} \pm 0.7 \text{ (syst)}) \times 10^{-4}. \tag{6.1}$$

Since the signal consisted of only 20 events, only a mass measurement was made; lifetime measurement in this mode required more data. In the second part of this thesis, we report a preliminary measurement of the lifetime of Λ_b^0 in the fully reconstructed decay mode $\Lambda_b^0 \to J/\psi\Lambda$. Measuring the lifetime in this decay mode is particularly interesting, since no other measurement has been published in a fully reconstructed decay mode.

More importantly, there was a long standing discrepancy in the measured value in Λ_b^0 and b-baryon lifetimes compared to theoretical predictions [29]. There was concern about this disagreement. Figure 6.1 shows the lifetime ratios where the yellow bands are theoretical predictions. The experimental world average for $\tau(\Lambda_b)/\tau(B^0)$ is 0.797 ± 0.052, while theory predicted the value to be between 0.9 and 1. However the most recent calculations, only

in the past year, show less of a discrepancy [29]. Figure 6.2 shows the recent results. To understand any discrepancy, we need to consider clean decays of Λ_b^0 baryon such as the exclusive $\Lambda_b^0 \to J/\psi\Lambda$ decay.

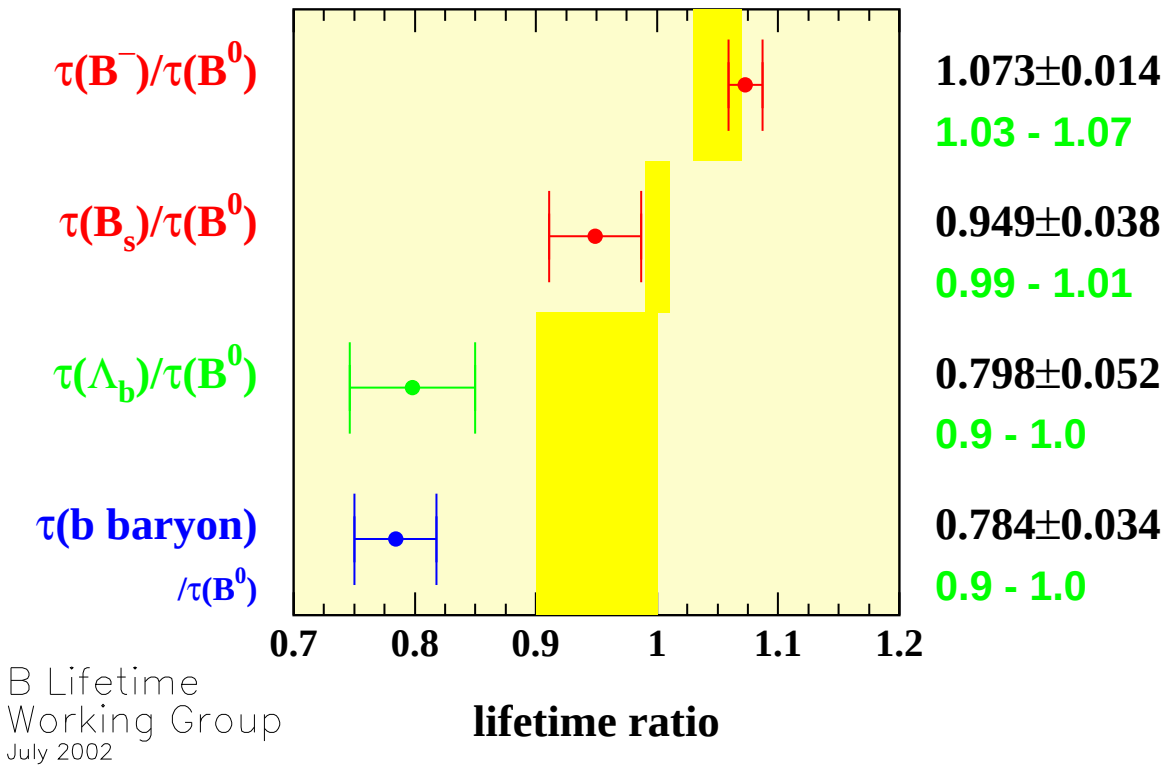

Figure 6.1: World averages of b hadron lifetimes compared to older theoretical predictions (yellow or dark grey bands).

The Λ_b^0 heavy baryon is an outstanding system to understand quark dynamics and Heavy Quark Effective Theory (HQET) and the operator product expansion (OPE) [41]. The quark content of Λ_b^0 is (udb) where the b quark is separated from the *(ud)* quarks that form their own spin-0 system. The $\Lambda_b^0 \to J/\psi\Lambda$ decay receives only small nonspectator contributions and hence its theoretical calculation is relatively straight forward.

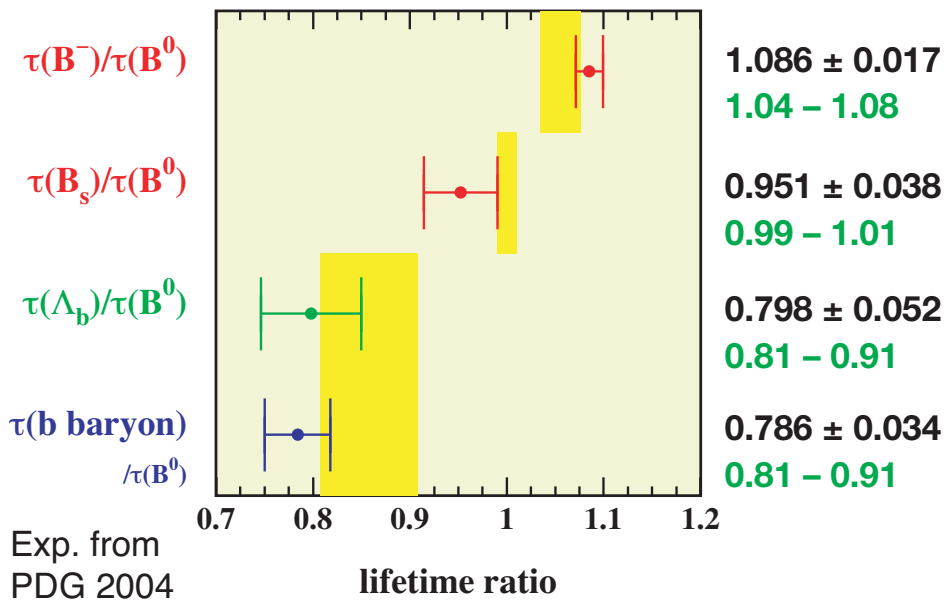

Figure 6.2: World averages of b hadron lifetimes compared to more recent theoretical predictions (yellow or dark grey bands).

The decay mode $\Lambda_b^0 \to J/\psi\Lambda$ is said to be fully reconstructed, because all of the final state particles leave tracks in the detector. Thus the Λ_b^0 full momentum and invariant mass may be determined. This is in contrast to semileptonic decay modes such as $\Lambda_b \to \Lambda_c \ell\nu$ that contain neutrinos. Neutrinos are neutral and interact very weakly; they leave no signal in the DØ detector. The semileptonic decays of Λ_b^0 have larger branching ratio and therefore are more abundant in our detector; however the sample is not as pure as in the case of fully reconstructed decay like $\Lambda_b^0 \to J/\psi\Lambda$.

Since the Λ_b^0 is more massive than than the B^+ and B^0 mesons, it is currently produced only at the Tevatron. DØ and CDF are the only currently operating detectors that can study it (in comparison to the B factories, Belle and BaBar, operating at the $\Upsilon(1S)$).

The decay $\Lambda_b^0 \to J/\psi\Lambda$ is a color-suppressed decay that proceeds through an internal W decay. The Feynman diagram is shown in Figure 6.3. The decay is color-suppressed because the colors of the quarks from the virtual W must match the colors of the c quark

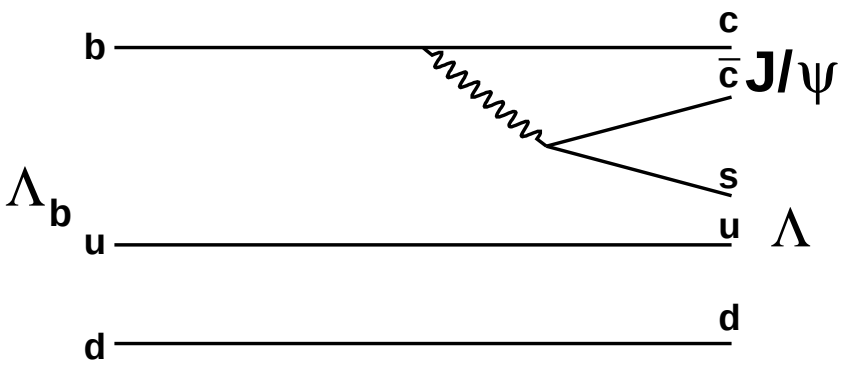

Figure 6.3: Feynman diagram for the decay $\Lambda_b^0 \to J/\psi\Lambda$.

and the remaining diquark system.

A brief description of the analysis follows. We reconstruct Λ_b^0 candidates as described in Chapter 9 and first establish the Λ_b^0 mass signal. In addition to reconstructing $\Lambda_b^0 \to J/\psi\Lambda$ we also reconstruct $B_d^0 \to J/\psi K_S^0$. This serves as a control sample, since it has similar topology to that of Λ_b^0 but the B^0 is more abundant and has a well-known lifetime. For each candidate, we obtain the value of proper decay length. We then perform an unbinned maximum likelihood fit to the distribution of proper decay lengths in the data, to extract the value of $c\tau(B^0)$ and $c\tau(\Lambda_b)$. A first result was presented at Lepton-Photon conference in Summer 2003. The signal and lifetime presented in this thesis are found with additional data until January 2004. Even more data, in an analysis continued by members of CINVESTAV group, resulted in a submitted result [36].

Chapter 7

Theory Predictions

7.1 Spectator Model

In the Spectator Model of hadrons, a heavy quark inside a hadron is bound to the lighter "spectator" quarks. One can estimate the weak decay of the heavy quark separately. In this approximation, all the hadrons containing a given heavy quark have the same lifetime. The heavier the quark the more valid the approximation. In the simple spectator model, we can write the decay width of a b hadron;

$$\Gamma(b) = \frac{9|V_{cb}|^2 G_F^2 m_b^5}{192\pi^3}. \tag{7.1}$$

This is simply the formula for the muon decay width, with the CKM matrix element V_{cb} for quark coupling (b to c). We assume b decays mostly to c. With $m_b \approx 4.2$ GeV [29] and $|V_{cb}| \approx 0.045$ [37] this gives $\tau = 1.2$ ps. Experiments are precise enough now to show that this model is clearly insufficient. Experiments show that $\tau(\Lambda_b) < \tau(B^0) \approx \tau(B_s) < \tau(B^+)$

7.2 Present Findings

In the previous section we stated that the "naive" spectator model is insufficient to explain the hierarchy of lifetimes of heavy hadrons. Heavy Quark Effective Theory is however employed to explain this hierarchy. Heavy Quark Expansion (HQE) predicts the ratios of

lifetimes of beauty mesons, which agree well with experimental observations well within experimental and theoretical uncertainties. Most recent analyses give [38, 39]

$$\frac{\tau(B_u)}{\tau(B_d)}|_{ex} = 1.085 \pm 0.017, \ \frac{\tau(B_u)}{\tau(B_d)}|_{th} = 1.07 \pm 0.03, \tag{7.2}$$

$$\frac{\tau(B_s)}{\tau(B_d)}|_{ex} = 0.951 \pm 0.038, \ \frac{\tau(B_s)}{\tau(B_d)}|_{th} = 1.00 \pm 0.02, \tag{7.3}$$

which show evidence of excellent agreement of theoretical predictions and experimental measurements. This agreement also provides us with some confidence that quark-hadron duality, which states that smeared partonic amplitudes can be replaced by the hadronic ones, is expected to hold in inclusive decays of heavy flavors.

The only remaining possible problem may appear in the ratio of lifetimes of heavy mesons and baryons. For instance, the low experimental value of the ratio $\tau(\Lambda_b)/\tau(B_d)$ has long been a puzzle for the theory. The latest compilation of experimental observations [39] suggests that the ratio

$$\frac{\tau(\Lambda_b)}{\tau(B_d)}|_{ex} = 0.797 \pm 0.053, \tag{7.4}$$

is inconsistent with the initial theoretical predictions of this ratio, as shown in Fig. 6.1. Only recent next-to-leading order (NLO) calculations of perturbative QCD [40] and $1/m_b$ corrections [41, 42] to the spectator effects significantly reduced the discrepancy, yielding, as reported in [43],

$$\frac{\tau(\Lambda_b)}{\tau(B_d)}|_{th} = 0.88 \pm 0.05, \tag{7.5}$$

which appears in better agreement with experimental data.

7.3 Formalism

Inclusive decay rates can be calculated in the HQE. The most convenient way of doing so is to employ the optical theorem to relate the decay width to the imaginary part of the matrix element of the forward scattering amplitude:

$$\Gamma(H_b \to X) = 1/2m_b\langle H_b|T|H_b\rangle,\, T = Im\, i\int d^4xT\{H_{eff}(x)H_{eff}(0)\}. \tag{7.6}$$

Here H_{eff} represent an effective $\Delta B = 1$ Hamiltonian at the scale $\mu = m_b$,

$$H_{eff} = \frac{4G_F}{\sqrt{(}2)}V_{cb}\sum[c_1Q_1^{u'd'} + c_2Q_2^{u'd'}] + h.c., \tag{7.7}$$

where d' and u' are quark flavor eigenstates, c_i are the Wilson coefficients, and Q_1 and Q_2 are the four-quark operators. In the heavy quark limit, the energy release is large and therefore an Operator Product Expansion (OPE) can be constructed for Eq. 7.6, which results in series of local operators of increasing dimension suppressed by powers of $1/m_b$ as shown [44]:

$$\begin{aligned}\Gamma(H_b \to f) \;=\; & \frac{G_F^2 m_b^5}{192\pi^3}|KM|^2\Big[c_3(f)\frac{\langle H_b|\bar{b}b|H_b\rangle}{2M_{H_b}} + \frac{c_5(f)}{m_b^2}\frac{\langle H_b|\bar{b}i\sigma_{\mu\nu}G_{\mu\nu}b|H_b\rangle}{2M_{H_b}} + \\ & + \sum_i \frac{c_6^{(i)}(f)}{m_b^3}\frac{\langle H_b|(\bar{b}\Gamma_i q)(\bar{q}\Gamma_i b)|H_b\rangle}{2M_{H_b}} + O(1/m_b^4)\Big],\end{aligned} \tag{7.8}$$

where the dimensionless coefficients $c_i(f)$ depend on the parton level characteristics of f (such as the ratios of the final state masses to m_b). KM denotes the appropriate combination of weak mixing angles, and $G_{\mu\nu}$ is the gluonic field strength tensor. The last term implies also the summation over the four-fermion operators with different light flavors q.

At leading order in the heavy quark expansion, all heavy hadrons have the same lifetime. The situation changes at higher orders. At order $1/m_b^2$ the difference between meson and baryon lifetimes appear due to the structure. The ratio of lifetimes of Λ_b^0 and B_d is

$$\frac{\tau(\Lambda_b)}{\tau(B_d)} = 1 + \frac{1}{2m_b^2}[\mu_\pi^2(\Lambda_b) - \mu_\pi^2(B_d)] + \frac{C_G}{m_b^2}[\mu_G^2(\Lambda_b) - \mu_G^2(B_d)] + O(1/m_b^3), \tag{7.9}$$

with $C_G \approx 1.2$ [44,45]. μ_π^2 and μ_G^2 represent kinetic energy and chromomagnetic interaction corrections [44]. At this order in the HQE, the difference is mainly driven by the fact that light quarks in Λ_b^0 appear in a $J^P = 0^+$ quantum state, diminishing any correlations of spins between the heavy-quark and the light quark-gluon cloud. This implies that $\mu_G^2(\Lambda_b) = 0$. With matrix elements of kinetic energy operators canceling each other to a large degree, this difference amounts to at most 1–2%, which is not sufficient to explain the observed pattern of lifetimes.

The main contribution comes from dimension six operators that enter at the $1/m_b^3$ level. An important subclass of these operators involves four-quark operators, whose contribution is additionally enhanced due to the phase-space factor $16\pi^2$. These effects are commonly called Weak Annihilation (WA), Weak Scattering (WS), and Pauli Interference (PI). They introduce differences in the lifetimes of all heavy mesons and baryons [44–47]. Their contribution to the lifetime ratios are governed by the matrix elements of $\Delta B = 0$ four-fermion operators:

$$T_{spec} = T_{spec}^u + T_{spec}^{d'} + T_{spec}^{s'}, \tag{7.10}$$

where T_i contributing to Eq. 7.6 are expressed in terms of the four-quark operators O_i^q. They are defined as, $O_1^q = \overline{b_i}\gamma^\mu(1-\gamma_5)b_i\overline{q_j}\gamma_\mu(1-\gamma_5)q_j$, $O_2^q = \overline{b_i}\gamma^\mu\gamma_5 b_i\overline{q_j}\gamma_\mu(1-\gamma_5)q_j$. Most of the recent progress in understanding lifetimes has been concentrated on computing the next-to-leading order (NLO) QCD corrections to Wilson coefficients of these operators or calculating matrix elements of these operators in quark models or on the lattice. At this order one can parametrize the meson-baryon lifetime ratio as:

$$\frac{\tau(\Lambda_b)}{\tau(B_d)} \approx 0.98 - (d_1 + d_2\bar{B})r - (d_3\epsilon_1 + d_4\epsilon_2) - (d_5 B_1 + d_6 B_2) + \delta_{1/m}, \tag{7.11}$$

where the scale dependent parameters d_i are defined in Ref. [45] and $r = |\psi_{bq}^{\Lambda_b}(0)|^2/|\psi_{bq}^{B_q}(0)|^2$ is the ratio of the wave functions at the origin of the Λ_b^0 and B_q mesons. $\delta_{1/m}$ represent contributions of order $1/m_b^4$ and higher. In the Ref. [41, 42], higher order corrections have been calculated and they shift the ratio of the lifetimes by -4.5% in addition to the $\approx$ 10% given by up to order $1/m_b^3$. In particular, when one goes to the calculation of the subleading $1/m_b$ $(1/m_b^5)$ as shown in Ref. [42], the inclusion of these corrections brings into agreement the theoretical predictions and experimental observations of the ratio of lifetimes of Λ_b^0 baryon and B_d meson. Even though these calculations bring into better agreement theory with experimental measurements, this is mainly due to sizable theoretical and experimental uncertainties. The discrepancy of $\tau(\Lambda_b)/\tau(B_d)$ ratio could reappear again if future measurements at the Tevatron and later at LHC would find the mean value to stay the same, with shrinking errors. In this thesis, we add another clean contribution to the world-average measurement of the lifetime ratio.

Chapter 8

The DØ Detector for Run II

This chapter describes the DØ detector and the Tevatron upgrade at Run II. It is based on Diehl's review [48]. Fig. 8.1 shows an elevation view of the DØ detector.

First in section 8.1 we define the coordinate system used in DØ detector. Section 8.2 describes the upgrades to the world's highest energy accelerator, the Tevatron, and its current status. Since the tracking system and muon spectrometer are crucial to B physics, emphasis will be placed on the muon detector and central tracking system in this chapter. Section 8.3 describes the new silicon vertex system. Section 8.4 describes the upgrades to the central fiber tracking system. Section 8.5 describes upgrades to the calorimeter systems. Section 8.6 describes the upgrades to the muon detectors. Section 8.7 describes the trigger systems. Section 8.8 describes the data acquisition system.

8.1 The DØ Coordinate System

At DØ, the primary coordinate system has the z-axis along the proton beam direction, and the positive y-axis pointing up, so that (x, y, z) make a right-handed Cartesian system.

Sometimes cylindrical (r, ϕ, z) coordinates are used, as are spherical (r, ϕ, θ) coordinates, r and θ, giving respectively the perpendicular distance and the angle from the z-axis. The azimuthal coordinate, ϕ, gives the angle from the x-axis in the $x - y$ projection.

The angular variables are defined so that $\theta = 0$ is along the positive z-axis direction, and $\phi = \pi/2$ is parallel to the positive y-axis.

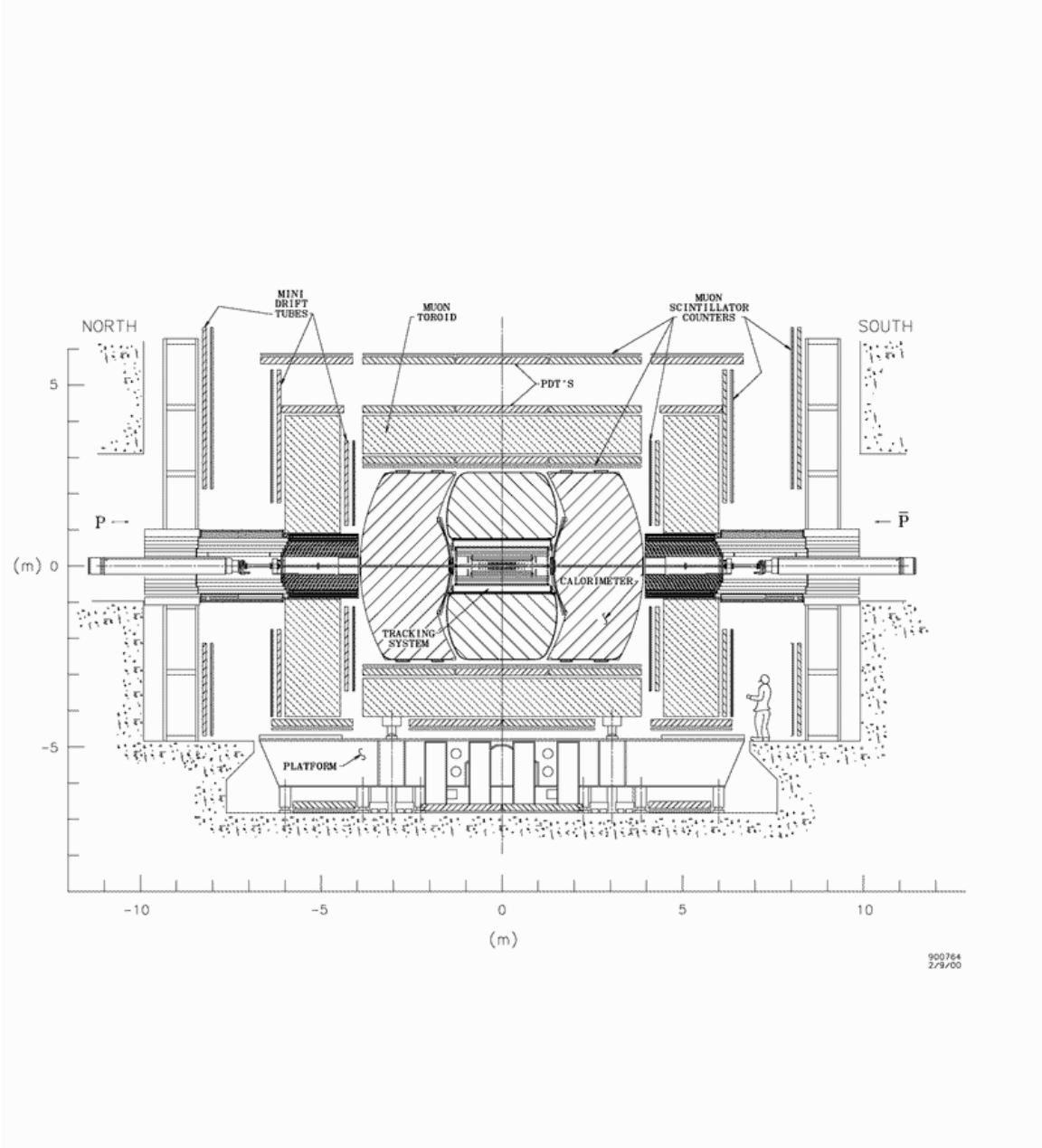

Figure 8.1: Elevation view of the upgraded DØ detector.

The rapidity y is defined as

$$y = \frac{1}{2} \ln \frac{E + p_z}{E - p_z}, \tag{8.1}$$

where E is the energy, and p_z is the particle momentum on the z-direction.

The variable of pseudorapidity is often more convenient, which is defined as

$$\eta = -\ln[\tan \frac{\theta}{2}]. \tag{8.2}$$

In the limit that $m \ll E$ (where m is the invariant mass), the pseudorapidity approximates the true rapidity.

"Transverse" momentum (p_T) is also commonly used. p_T is the momentum vector projected onto a plane perpendicular to the beam axis:

$$p_T = p \sin \theta. \tag{8.3}$$

This is particularly useful due to the fact that in a high energy collision, many of the products of the collision escape down the beam pipe, so the momenta along the beam of the colliding partons are unknown. However, their transverse momenta are very small compared to their momenta along the beam, so momentum can be considered to be conserved in the transverse plane.

8.2 The Run II Accelerator Upgrade

In Run II, beginning in March 2001, the Tevatron collides protons with antiprotons at a center-of-mass energy of 1.96 TeV, which is a slightly higher energy than the 1.8 TeV available in Run I. In the first 3 years, four times the Run I integrated luminosity has been collected (by the end of August 2004). We show in Fig. 3.2 a schematic of the Fermilab Tevatron Collider.

In Run II, a large advance has been made with the construction of the Main Injector, a 150 GeV synchrotron, built in a separate tunnel from the Tevatron. The Main Injector has replaced the function of the Main Ring for antiproton production. It produces 2×10^{11} antiprotons per hour [49], four times the rate of the old Main Ring. A new permanent magnet "Recycler Ring" [50] allows recovery and reuse of uncollided antiprotons when the Main Injector has produced enough to merit injecting a new store into the Tevatron. Instantaneous luminosities in the range $5-20\times10^{31}\mathrm{cm}^{-2}\mathrm{s}^{-1}$ were available early in Run II. Because the number of protons per bunch is near the limit of the Tevatron, the number of bunches is increased from Run I's 6 bunches of protons and 6 of antiprotons to 36 of each species. With an instantaneous luminosity of $20 \times 10^{31}\mathrm{cm}^{-2}\mathrm{s}^{-1}$, an average of 5.2 $p\bar{p}$ collisions occurs each bunch crossing. Increasing the number of bunches decreases the average number of collisions per bunch crossing. By decreasing the bunch width as the store is depleted by collisions, the luminosity can be maintained at an optimal level.

Such changes have profound implications for the detectors. Where in the past, there were 3.5 microseconds between each beam crossing, in Run II this is 396 ns for 36 bunches. This required all the front-end electronics from the detector to be replaced with electronics capable of faster response. Aside from the issues of shorter times between collisions, the detector improves its ability to identify leptons, energetic photons and charged particles, and particles emerging from a secondary vertex (daughters of long-lived parents). Increasing the collision rate by an order of magnitude also requires substantial upgrades of the trigger and data acquisition systems to handle the increased data flow.

8.3 Silicon Microvertex Tracker (SMT)

The purposes of the silicon detectors are to identify tracks of charged particles that decay before they reach the outer tracker, to reconstruct the decay vertices of b hadrons, and to extend or improve the track-finding and momentum resolution. Because the proton and antiproton beams are very thin ($\sigma_{\mathrm{transverse}} < 40\ \mu\mathrm{m}$) and because their transverse positions

can be maintained very close to the center of the beampipe, a typical b-hadron decay vertex can be identified by the impact parameters of the tracks of ~ 300 μm. This requires fine-pitched detectors oriented perpendicularly to the trajectories of the charged particles and mounted as close as practical to the decay vertices. The fine pitch and small radius necessary to achieve sufficient impact parameter resolution also improves the momentum resolution of the tracker systems.

The accelerator parameters contribute to the design decisions. The interactions are spread out over a length $\sigma_z = 25$ cm, setting the length scale and motivating the detectors to have extended geometries. The expected integrated luminosity implies a radiation dose of ≤ 1 Mrad during the life of the silicon detector. This, in turn, forces the sensors and readout chips to be radiation-hard and operated at cold temperatures, which mitigates some of the adverse effects of radiation.

The basic detector design is the "barrel geometry" comprised of layers of silicon detectors arranged in plates perpendicular to the beampipe. In addition to measuring separated vertices and improving the momentum resolution, DØ chose to use silicon detectors to extend the tracking coverage to high pseudorapidity with disk-shaped assemblies comprised of wedge-shaped silicon wafers arranged in plates oriented perpendicular to the beamline.

The DØ silicon microvertex detector [53] consists of six barrel modules, twelve small disks ("F-disks"), and four large disks ("H-disks"). The mixed barrel/disk geometry provides silicon sensors arrayed at normal incidence, as is optimal for good tracking resolution, to charged particles with $|\eta| < 3$. Figure 8.2 shows the DØ silicon barrel modules with barrel detectors parallel to the beamline and disks perpendicular to the beamline.

The six barrel modules are constructed with 4 layers of ladder assemblies with considerable overlap. Each barrel module is 12.4 cm in length and the total length of the barrel is 76.2 cm. The 4-layer coverage corresponds to the region $\eta = 1.5$ for interactions at $z = 0$. Barrel layers one and three are constructed from double-sided silicon sensors with axial $(r - z)$ and $90°$ stereo layers, except for the modules on each end of the barrel, modules one and six, which have single-sided axial strips. These are single-sided because

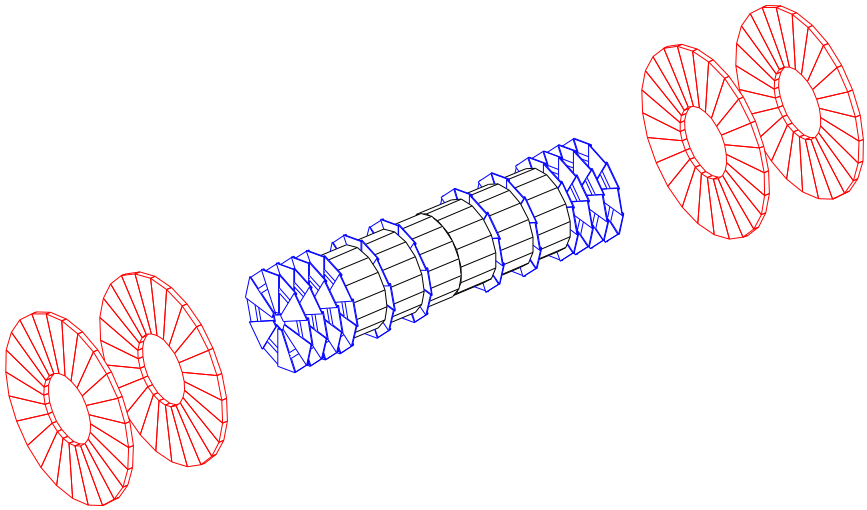

Figure 8.2: DØ silicon detector. The figure shows the configuration of the 6 barrel modules, the 12 "F-disks", and the 4 "H-disks".

stereo tracking is dominated by the information from the F-disks. Barrel layers two and four are constructed from double-sided detectors with axial and 2° stereo layers in all six barrel modules. All of the detectors are AC-coupled to the readout electronics.

The 12 "F-disks" are comprised of 12 trapezoidal wedges arranged into a plate with a hole for the beampipe. The active area inner radius is at 2.5 cm from the center of the beampipe and the outer is at 9.8 cm. The detectors are AC-coupled, double-sided, with strips angled at $\pm 15°$ with respect to the vertical. The pitch of the p-side and n-side detectors is 50 μm and 62.5 μm, respectively, and the silicon wafers are 300 μm thick. Naturally, the strips are of different length depending on their locations on the wedge. The six innermost F-disks attached to the outer sides of the six barrel modules. The three additional F-disks are attached to each outer side of the barrel assembly, with the effect of extending the acceptance of the silicon system to higher pseudorapidity, especially for interactions which occur at larger z.

The four large "H-disks" are located at $z = \pm 94$ cm and $z = \pm 126$ cm. The inner radius

of the active area is at 9.6 cm from the center of the beampipe and the outer is at 23.6 cm. The detectors are AC-coupled, single-sided, with 40 μm pitch strips (pairwise readout makes the effective pitch 80 μm) angled at $\pm 7.5°$ from the vertical. Each plane has wedges glued together back-to-back to provide a 15° stereo angle. These forward disks are necessary to provide track stubs for forward particles which would otherwise exit the region of full solenoidal magnetic field without hitting the outer tracker. They cover a pseudorapidity range of approximately $2 \leq |\eta| \leq 3$.

All of the three detector types are able to withstand a radiation dose greater than 1 Mrad. The dose depends on the detector location and integrated luminosity. The innermost layer is expected to receive 0.5 Mrad/fb^{-1}. The effect of the radiation damage is to increase the leakage current, increase the bias voltage necessary for full depletion, and decrease the signal-to-noise ratio. The effects are temperature dependent and can be reduced by operated the detectors at low temperatures. The detectors are operated at temperatures between $5 - 10°$ C using a cooling mixture of deionized ethylene glycol and water.

The DØ silicon detectors are read out using the SVX II chip [54]. SVX II is a 128 channel, radiation hard CMOS chip mounted directly on the "High Density Interconnects" (HDI's), kapton-based flexible circuit, wire-bonded to the sensors at the ends of the ladders and wedges. Each of the 128 channels in an SVX II chip features a preamplifier, a 32 stage analog pipeline with 4 μs delay, an 8-bit Wilkinson type ADC, and a latch-based sparsified readout. The chip is programmable for any interaction time from 132 to 396 ns. The pipeline depth, ADC ramp rate, preamplifier bandwidth, and thresholds are downloadable to each SVX II chip.

Connections to the outside world continue from the HDI's to 8-ft long "low-mass" cables that join the ends of the HDI's to unpowered "transition cards" mounted on the ends of the central calorimeter cryostat. Ultimately, these signals are gathered by a sequencer board connected by optical link to VME readout buffer electronics in the movable counting house. The DØ silicon detector has 792,576 channels.

8.4 Outer Tracker: Central Scintillating Fiber Tracker (CFT)

The outer tracker [48] is the charged particle tracker at largest radius within the calorimeter. Outer trackers perform two functions. The first is measuring the momentum and charge of particles produced in the collision, and the second is to provide pattern recognition assistance for the silicon detectors.

A particle with non-zero charge q and momentum p in a solenoidal magnetic field along the z-direction of strength B will travel in a helix with radius r given by

$$r = \frac{p_T}{qB}, \tag{8.4}$$

where $p_T = \sqrt{p_x^2 + p_y^2}$. Therefore, by measuring the track's curvature in the $r - \phi$ plane, we effectively measure p_T. By measuring the track's direction in the $r - z$ plane, we measure p_T/p_z, which completes our measurement of the 3D momentum vector of the particle.

Tracks in these detectors typically have several dozen hits, which allows for highly efficient and pure identification of these tracks. Silicon trackers in these detectors have of order a half-dozen hits, and while they can be used standalone, a much better way to use them is to find the track in the outer tracker and project this track back into the silicon. Once the approximate trajectory in the silicon detector has been established, the tracking algorithm can search the silicon detector for hits and use these hits to improve the track measurement. This technique uses each component to its best advantage: the silicon tracker measures the track's point of origin and initial direction, and the outer tracker measures the track's momentum.

The DØ Solenoid and Scintillating Fiber Tracker

One substantial improvement to the DØ detector for Run II was the addition of a superconducting solenoidal magnet providing a solenoidal field of 2T parallel to the z-axis. Having a magnetic field enhances the DØ detector. It has the ability to measure the momentum

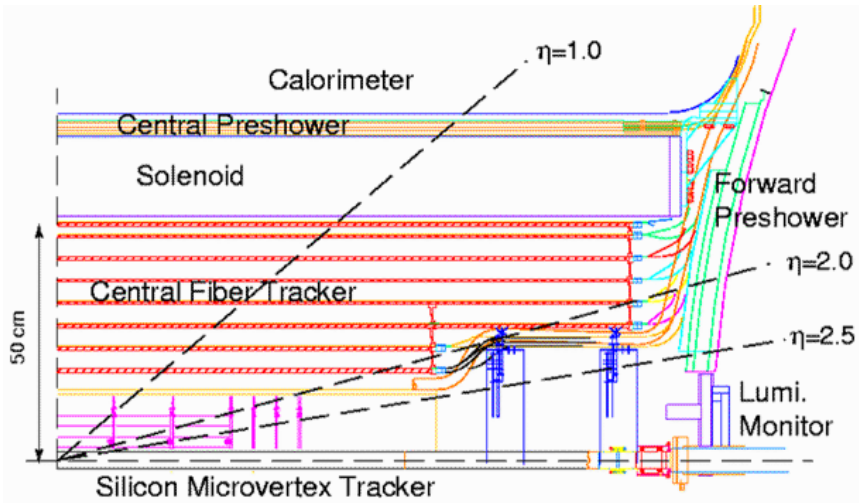

Figure 8.3: DØ's scintillating fiber tracker.

and charge of leptons and hadrons. The muon momentum can be measured in the central magnetic field, before the muon has scattered in the steel of the muon toroids, and this allows for the comparison of the muon's momentum as measured in the solenoid to the momentum as measured in the toroids. We can see that the muon momentum resolution is much improved after matching a muon local track with central track.

Mechanically, the DØ outer tracker is a simple device. Layers of scintillating fiber are placed on carbon-fiber composite cylinders. When a particle travels through one of these fibers, the scintillator emits light, which is totally internally reflected down the fiber, coupled to a clear fiber, and transported to a solid-state light detector. Fig. 8.3 shows a side view of the tracker.

In detail, the DØ central fiber tracker (CFT) [55] consists of scintillating fibers mounted on eight concentric cylinders made from a composite of layers of high modulus of elasticity carbon fiber sandwiching structural foam. The cylinders range in radius from 20 to 50 cm and are about 2.5 m in length, except for the inner two, which are about 1.7 m in length. The scintillating fibers are double clad, 835 μm in diameter, and are constructed in ribbons

each 128 fibers wide composed of a "doublet" layer of fibers with the centers of one of the single layers in the space between the fibers of the other single layer. There are eight doublet axial (aligned along the beam axis) layers of scintillating fiber, as well as eight doublet stereo layers that make a $\pm 3°$ angle with the beam axis. The outer (8th) layer is at the largest possible radius. The 7th layer is as close to the outer layer as is possible. The inner layer is at the least possible radius. The detector is divided into 80 sectors in ϕ. Each pie-shaped slice has 960 fibers and the entire detector therefore has 76,800 channels.

The scintillation light from the fibers is totally internally reflected down the length of the fiber. A connection is made at the edge of the tracker to a clear fiber that transports the light to a solid-state light detector called a Visible Light Photon Counter (VLPC). The number of photons available at the VLPC's, for a charged particle which traverses through the center of a fiber, varies from 10 to 40, depending on the charged particle's pseudorapidity and on attenuation due to the distance from the clear fiber connector. The VLPC's are small silicon devices which have an array of eight photo sensitive areas, each 1 mm in diameter, on their surface. They operate at temperatures from 6 to 15 K, have a quantum efficiency of over 80%, and have a gain of 20,000 to 50,000. The high quantum efficiency is important because of the low number of photons.

The momentum resolution is currently $\sigma(p_T)/p_T = 0.13\% \cdot p_T$ when scintillating fiber tracker measurements are combined with the silicon tracker. The p_T-dependent impact parameter resolution is currently 30 μm in the x and y direction, and 42 μm in the z direction for high momentum tracks, if SMT and CFT information are combined.

8.5 Calorimeters and Preshower Detectors

Because of the dependence of the Tevatron's physics program on lepton identification and jet energy measurement, calorimetry is a critical aspect of Run II experiments. The calorimeters are used for identification and measurement of the electron, neutrino and jets from the decays of the top quarks in these events.

The calorimetry is divided into two parts, electromagnetic and hadronic. Nearest the vertex is the electromagnetic calorimeter that measures the energy of electrons and photons (including those from π^0 and η decay) and has improved position measurement at the point of maximum shower development. Farther in radius is the hadronic calorimeter which measures the energy of hadrons as they interact with the material of the calorimeter. Muons deposit a small amount of energy (due to ionization) in both sections, and the lack of a large energy deposit can be used to identify a particle as a muon. Neutrinos deposit no energy at all in these calorimeters, but the absence of energy deposition appears as a momentum imbalance in the transverse plane, also called "missing E_T".

DØ's hermetic, radiation-hard uranium and liquid-argon calorimeter [52] consists of three separate cryostats: the Central Calorimeter (CC), and the two Endcap Calorimeters (EC's). Each is segmented into an electromagnetic section, a hadronic section, and a coarse hadronic section (inside to outside), with many layers of sampling. Each is divided into pseudoprojective towers covering $\eta \times \phi = 0.1 \times 0.1$ rad. The readout of the electromagnetic section has four layers of longitudinal segmentation. The third electromagnetic layer, at EM shower maximum, has segmentation $\eta \times \phi = 0.05 \times 0.05$ rad. The readout of the hadronic sections have 4 (5) longitudinal layers in the CC (EC's). There are no projective cracks. The calorimeter provides hermetic coverage to $|\eta| < 4$. The energy resolution is $\sigma_E/E = 15\%/\sqrt{E(GeV)} \oplus 0.4\%$ for electrons and photons. For charged pions and jets the resolutions are approximately $50\%/\sqrt{E(GeV)}$ and $80\%/\sqrt{E(GeV)}$, respectively.

The Inter Cryostat Detectors (ICD's) augment the DØ liquid argon calorimeters by providing a measurement of the energy in between the central and endcap cryostats. This improves the energy measurement for jets that straddle the intercryostat region and improves the resolution of the missing transverse energy measurement. Sixteen new ICD detector segments form an annular ring of 1/2" thick scintillator covering $1.1 \leq |\eta| \leq 1.4$ on the hadronic section of the inner end of each EC cryostat. The sixteen segments are further segmented into sections of size $\Delta\eta \times \Delta\phi = 0.1 \times 0.1$. Each section has an embedded wavelength shifting fiber to collect light. These are in turn connected to long clear fibers

which carry the light to photomultiplier tubes located underneath the cryostats, in a region with reduced magnetic field from the solenoid.

The primary purpose of the Central and Forward Preshower Detectors (CPS and FPS) is to exploit the difference between energy loss mechanisms of electrons and photons with that of the backgrounds, principally hadronic jets with leading π^0's, to improve the trigger and offline purity. Secondly, they provide a precision measurement of the starting point of the electromagnetic showers. The CPS is cylindrically shaped, mounted on the outside of the solenoid magnet, and covers the region $|\eta| \leq 1.3$. The FPS are shaped like annular rings, mounted on the inside of the EC's, and cover the region $1.5 \leq |\eta| \leq 2.5$. The FPS and CPS are shown in Fig. 8.4.

The DØ Run II luminosity monitor (Level-0) consists of two arrays of plastic scintillation counters located on the inside faces of the EC's and arranged symmetrically around the beampipe. The pseudorapidity coverage is $2.7 \leq |\eta| \leq 4.4$. Because the solenoid field is ~ 1 Tesla in that region, short magnetic field resistant photomultiplier tubes are used to read the light. A coincidence of hits in the counters on both sides of the interaction point provides the simplest indication that an inelastic collision occurred.

A new near beam detector called the "Forward Proton Detector (FPD)" is available for Run II. It is a series of small, retractable scintillating fiber detectors placed a few millimeters from the beamline in the region 20–60 meters from both sides of the interaction point. They are triggered by small scintillation counters and read out by multi-anode PMT's. Their purpose is to identify scattered protons and anti-protons in diffractive events.

8.6 Muon Systems

The muon detection strategy at DØ relies on the penetration power of muons. Several meters of absorber (including the calorimeters) absorbs the vast majority of hadrons, and any charged particle that penetrates this material is inferred to be a muon. Because they are at large radius, muon detectors are large, and to keep costs reasonable, they have very

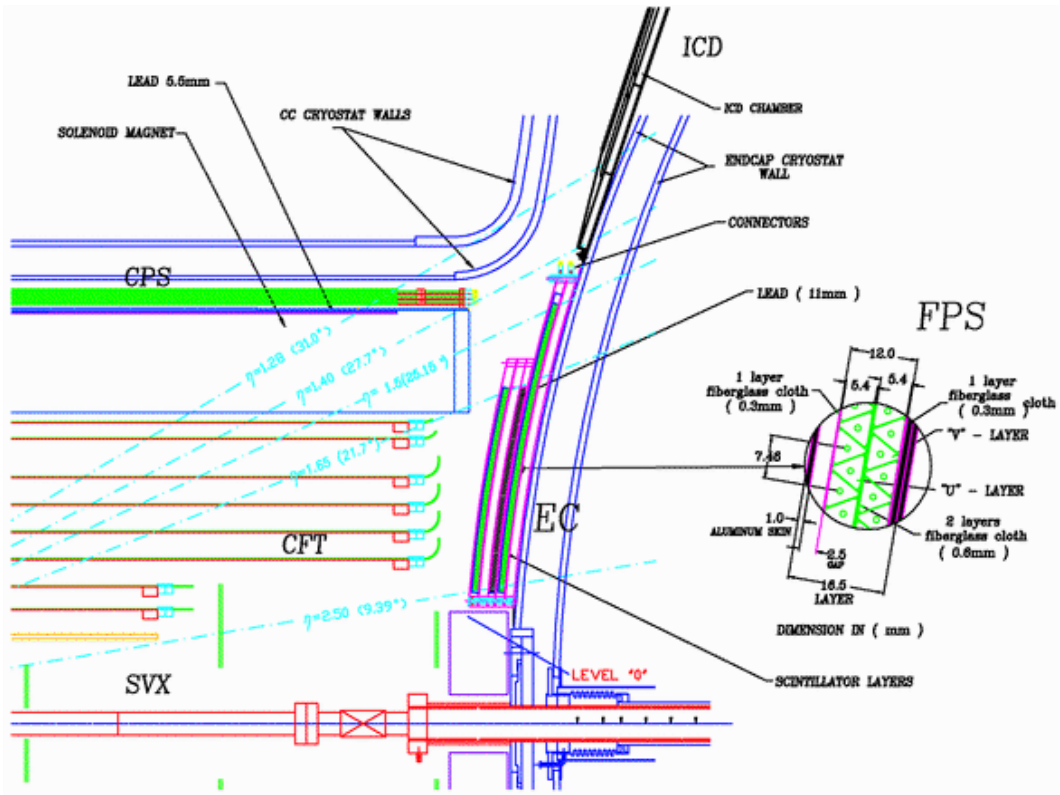

Figure 8.4: One quarter $r - z$ view of the end of the DØ trackers and the start of the EC, indicating the Central Preshower, the Level-0 detector, the solenoid magnet and calorimeter cryostats, and the Forward Preshower detector. The Forward Preshower detector is shown in detail in the inset.

coarse granularity: typically they are single wire proportional chambers with drift times in excess of a microsecond. Fig. 8.5, and 8.6 show an $r - z$ view of the DØ detector, and all components are illustrated in the graph.

The muon detector consist of scintillator and drift tubes, with effectively complete coverage out to $|\eta| < 2$. As seen in the layout, the detector is split at $|\eta|$ of 1 into a central and forward system. Each has 3 layers (usually called A,B,C with A between the calorimeter and iron and the other two outside the iron) of drift tubes. In the central region are proportional drift chambers (called PDTs). In the forward region are minidrift tubes (called MDTs). Figure 8.7 shows the layout of PDTs and MDTs.

In Run II, scintillator counters are added adjacent to the chambers. Scintillator has a response time measured in nanoseconds, so that the coincidence between the counter and the chamber unambiguously determines the bunch crossing. Because the timing resolution is substantially better than the minimum required to resolve bunch crossings, we gain the ability to use timing to reject certain backgrounds: particularly out of time particles produced upstream of the interaction point and cosmic rays.

There is 2 or 3 layers of scintillator coverage with the forward scintillators sometimes called pixels, the central A-layer counters called A-phi, and the BC counters called the cosmic cap. Scintillator time is read out with both a 15–20 ns "trigger" gate and a 80–100 ns "readout" gate. The DØ detector relies on layers of scintillation counters and drift chambers to identify muons and measure their position and momentum.

The muon system has three large toroid magnets, one central and two forward, which act as absorber in addition to the calorimeter, provide a structure on which to mount the muon detectors, and provide a bend to the muons so the detectors can measure the momentum. The calorimeters contain between 7 and 10 interaction lengths of material, depending on the pseudorapidity. The thickness of the calorimeters plus the toroid magnets varies between 13 to 14 interaction lengths for $|\eta| \leq 0.9$, 10 to 15 interaction lengths for $0.9 \leq |\eta| \leq 1.2$, and 18 to 20 interaction lengths for $1.2 \leq |\eta| \leq 2.0$. Muons with momentum greater than ~ 1.4 GeV/c (~ 3.5 GeV/c) penetrate the calorimeter (toroid magnet) at $\eta = 0$. In addition, new

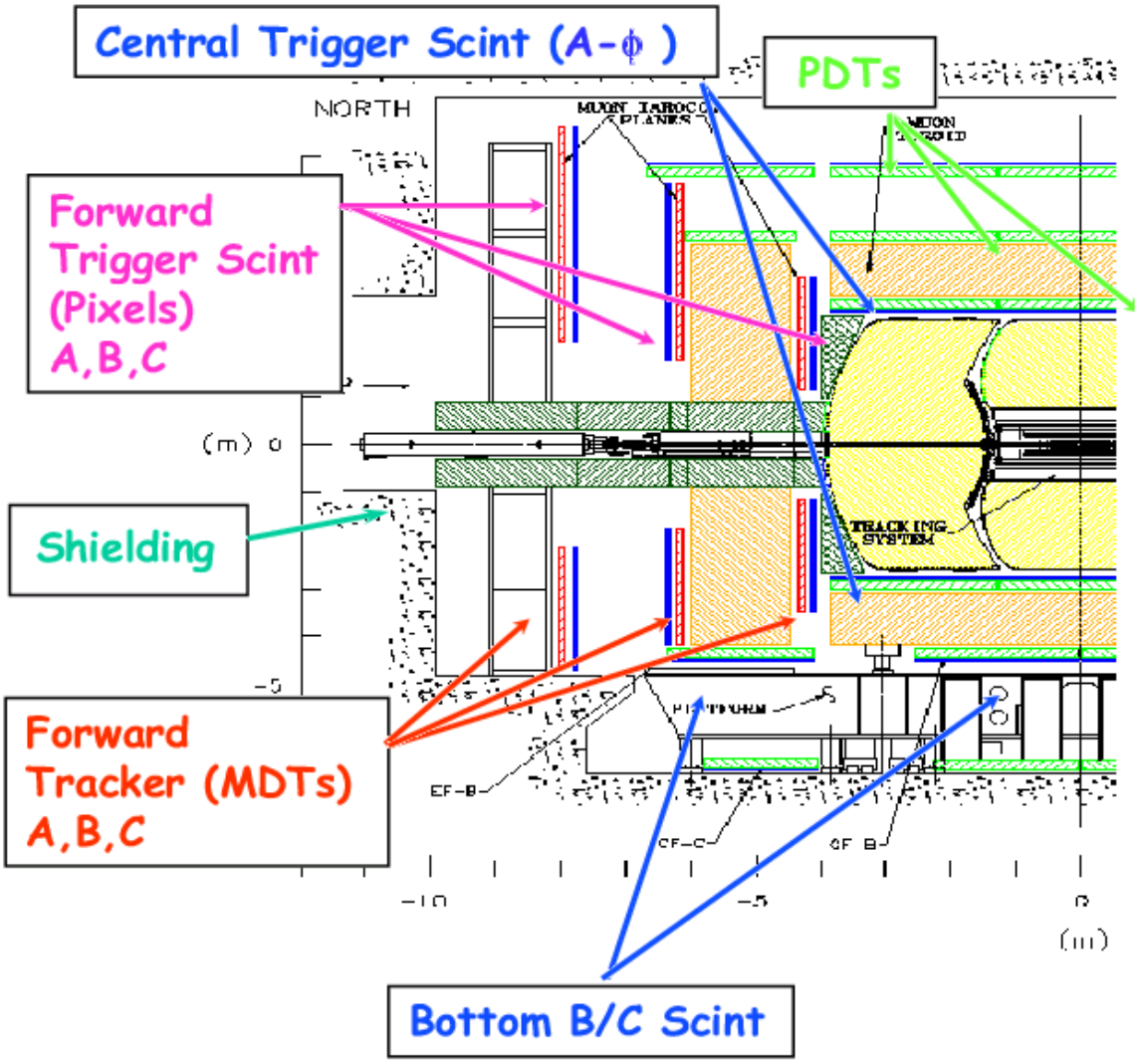

Figure 8.5: Half $r - z$ view of the DØ muon subdetector.

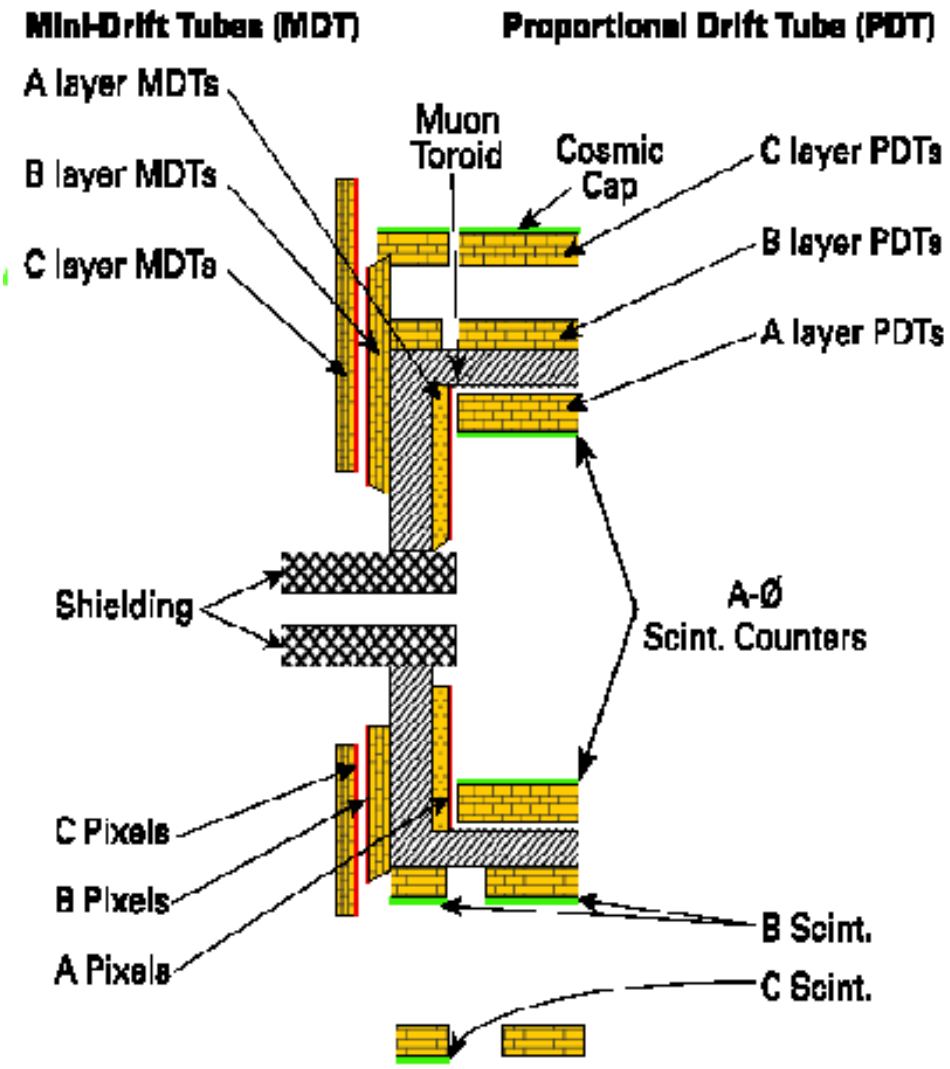

Figure 8.6: Illustration of the DØ muon subdetector components.

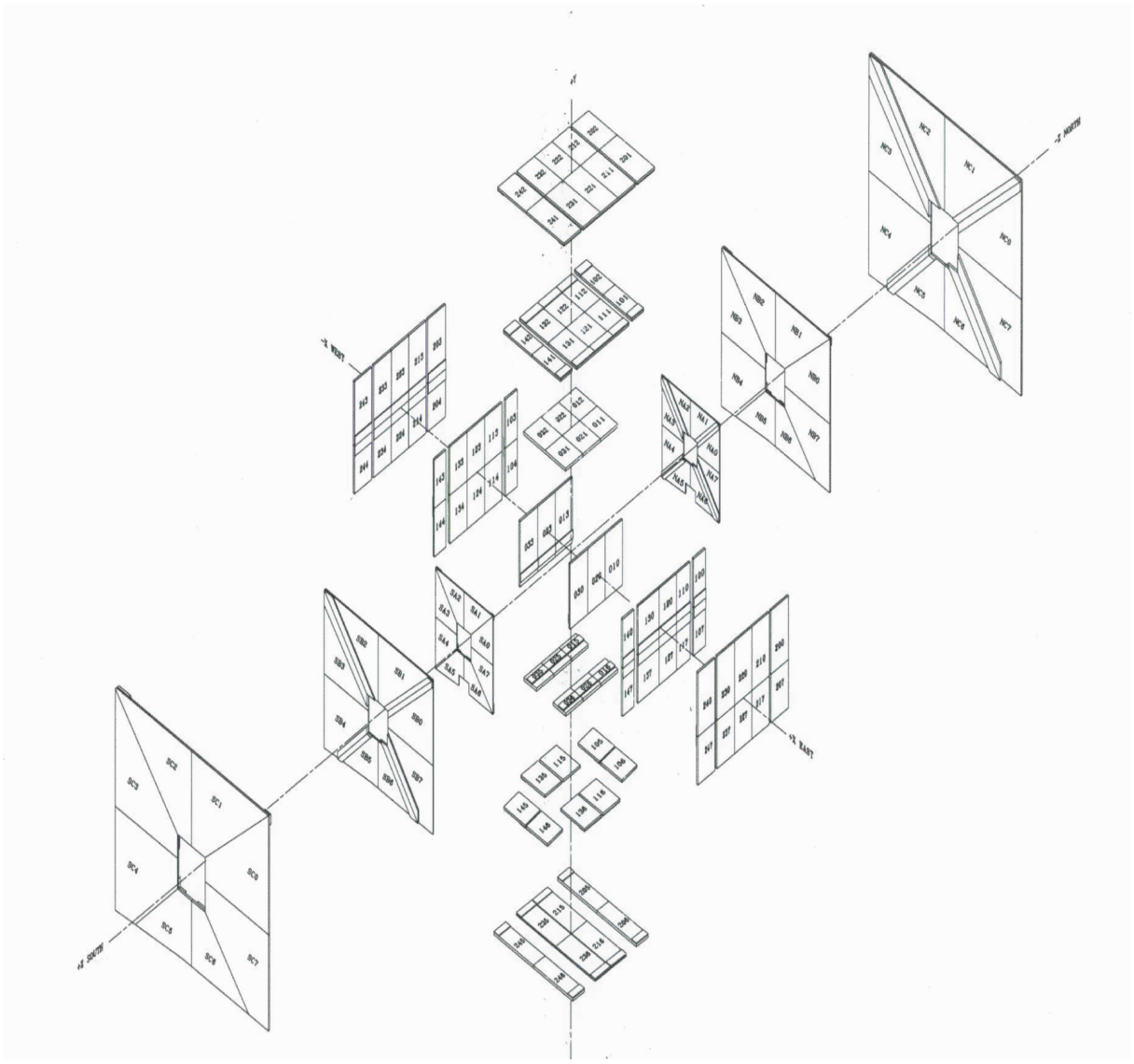

Figure 8.7: Layout of PDTs and MDTs.

massive shielding structures isolate the muon detectors from backgrounds generated near the beampipe and accelerator elements.

8.6.1 Central Muon System Drift Chambers

The central muon drift chambers were retained from Run I, but their electronics have been replaced. The drift chambers are made from extruded aluminum cells of 4-inch width and lengths up to 228 inches. The wires in the cells are parallel to the field in the toroid magnets so that the bending of the track in the toroids takes place in the drift ordinate. Refer to Fig. 8.5, 8.6.

Individual drift chambers (PDT's) in the C- and B-layers consist of three staggered decks of up to 24 cells each. Drift chambers in the A-layer consist of four staggered decks of 24 cells each, except for the ones on the bottom, which are three deck PDT's. The top and bottom of each cell has a copper-clad cathode pad. The copper has a milled cut separating it into an inner and outer pad such that the width of the inner pad alternately increases and decreases along its length. The wavelength of the vernier is 24 inches. Pairs of wires are connected through a delay chip at the end away from the front-end electronics. Fig. 8.8 shows the geometry of a PDT cell.

On passing through a cell, a muon will cause a hit in the cell and a hit in the neighbor cell which is some time later depending on the muon's proximity to the far end. Charge is accumulated on the inner and outer pads of the cell through which the muon passed. The drift time is derived from the sum of the two cells times. The distance along the wire is derived from the difference. The normalized difference of the integrated pad charge provides the distance along a pad wavelength.

The Run I A-layer PDT's were rebuilt so as to increase their effective lifetimes. The ends of the PDT's were removed. The cathode pads, which outgassed a dielectric that coated the anode wires in Run I, were replaced with new G-10 pads that do not outgas. The lifetime of the B- and C-layer PDT's is long enough so that aging won't pose a problem

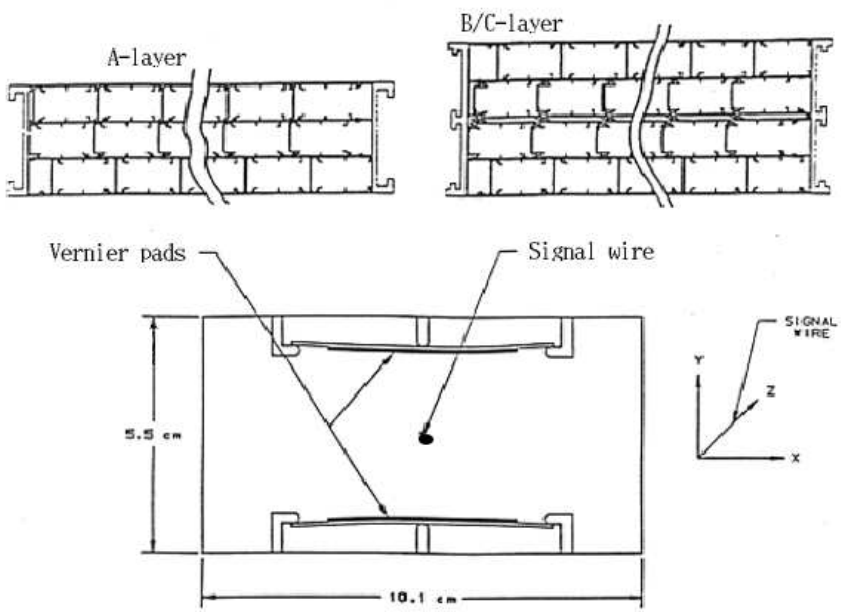

Figure 8.8: Geometry of a PDT cell.

for these detectors.

The PDT's use a drift gas composed of 80% argon, 10% CF_4, and 10% CH_4. The maximum drift time is approximately 500 ns, longer than the bunch spacing. This poses no problem for the electronics, which records each hit in as many crossings in that it could have occurred. The time measurements are made in 1.8 ns bins. The drift ordinate resolution is ~ 500 μm per hit, limited by the fluctuations in the drift time due to the gas. Normally the drift velocity is about 0.1 mm/ns.

The muon momentum is calculated from the bend in the toroid magnet as determined from the difference in slopes between the line formed from the interaction point and the A-layer hits and the line through the B- and C-layer hits. The momentum resolution is expected to be $\sigma(1/p) = 0.18/p \otimes 0.005$ with p in GeV/c. This momentum resolution is worse than that expected from the fiber tracker measurement, especially at low p_T.

8.6.2 Central Muon System Scintillation Counters

An important part of the upgrade is two new layers of scintillation counters. These detectors not only tag the bunch crossing from which the muons originate for the slow drift chambers, but also reject background particles which leave hits at times other than expected from a muon originating at the interaction point. Refer to Fig. 8.5, 8.6.

The A-layer contains 630 "A-phi" counters, each approximately 32" long and spanning 4.5° in azimuthal angle. There are 9 counters in a row spanning $-1.0 \leq \eta \leq 1.0$. Each row has a slight overlap with a neighboring row so as to minimize the cracks between counters. The counters are made from 1/2 inch thick Bicron scintillator plates with many Bicron BCF'92 wavelength shifting fibers embedded in deep grooves. The fibers collect and transmit the light to a single photomultiplier tube (PMT). The counters have a time resolution of $\sigma = 4$ ns and are expected to discriminate between muons produced in the collisions and the background, that is composed of particles backscattered from the calorimeter exit, and arrives 14 ns later than a muon. The "A-phi" counters span 93% of the azimuthal angle.

There is a gap in the A-layer coverage where the calorimeter is supported by the detector platform.

A layer of scintillation counters has been added on the outside of the muon toroid magnet. The 240 "Cosmic Cap" C-layer scintillation counters were deployed late in the second half of Run I and previously have been described in detail [57]. These counters are between 81.5 and 113 inches long and 25 inches wide. Eight of them are mounted on the outside of each C-layer PDT on the top and sides of the central muon detector. Underneath the toroid magnet, the three layer coverage is broken up because of the support structure for the central platform and toroid magnets. 120 new "Cosmic Bottom" counters are arrayed on bottom C-layer and B-layer PDT's. The Cosmic Cap and Cosmic Bottom counters are made from 1/2 inch thick Bicron scintillator with Bicron BCF'91A wavelength shifter fibers embedded in grooves. Each counter is read out with two photomultiplier tubes. One advantage of using two PMT's is that coincidental tube noise is improbable. Another is the immediate redundancy available in case one of the PMT's fails.

The scintillation counters have an LED pulser calibration system capable of providing a clocked, timed, amplitude-controlled photon pulse. Each PMT is connected by a light-shielded optical fiber to a light-tight box which houses bundles of LED's glued into a clear acrylic block. A single box may provide the photon pulse for up to 100 PMT's. The stability of the photon pulse is monitored with a light-sensitive diode housed in the clear block. This system allows the timing and amplitude to be monitored and controlled.

The muon system has a wide range of options available for triggering. Triggers may be composed of coincidences of in-time hits in scintillation counters, hits in layers of the PDT's, and tracks found in the central tracker. Low-p_T muons would rely on hits only in the A-layer detectors and fiber tracker. High-p_T muons would also use scintillation counters and PDT's in the B- and C-layers.

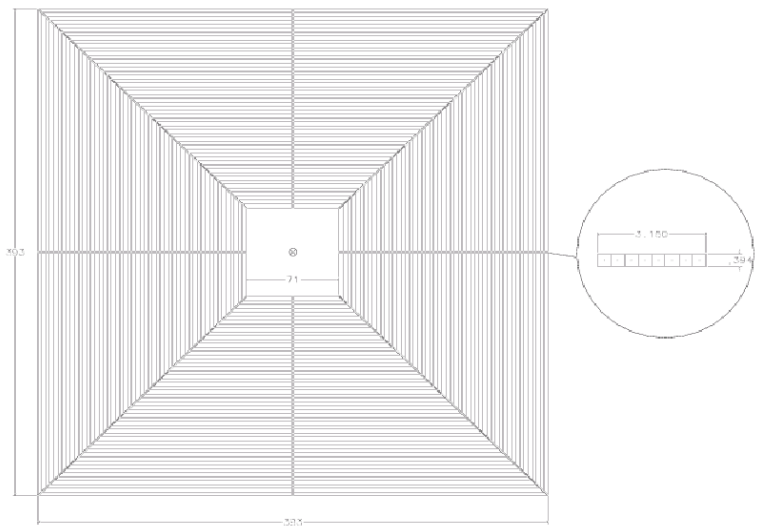

Figure 8.9: DØ forward muon mini-drift tube (MDT) plane. The octant boundaries are shown.

8.6.3 Forward Muon System Drift Tubes

The Mini-Drift Tube (MDT) system [58] is comprised of three planes of drift-tubes, with one plane in front of, and two planes behind the forward toroid magnet. The layers are divided into octants with tubes of different length depending on position in the octant. As in the central region, the MDT A-layer has four decks of drift tubes and the B and C-layers have three decks each. The drift tubes, made from long aluminum extrusions of eight 1 cm square cells, are contained in plastic sleeves. Wires in the cells are oriented parallel to the magnetic field of the forward toroid magnet. The sleeves of tubes are mounted on an aluminum support structure which also provides mechanical support for the infrastructure. A plane of MDT counters is shown in Fig. 8.9.

The MDT's use a non-flammable gas mixture composed of 90% CF_4 and 10% CH_4, with a maximum drift time of about 60 ns. The momentum resolution is limited by multiple Coulomb scattering in the iron toroid and the hit resolution of the detector. The MDT

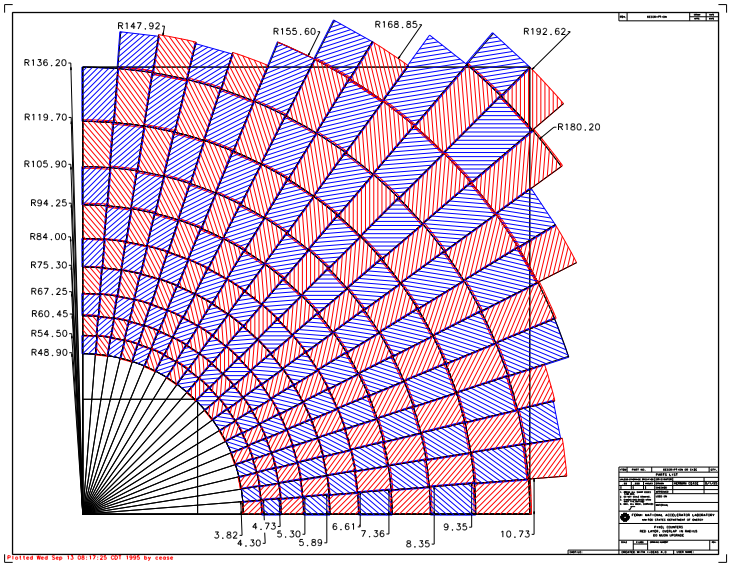

Figure 8.10: Two DØ forward muon pixel octants.

electronics uses a coarse digitization of the drift time (18.8 ns time bin). The momentum resolution is roughly $\sigma(p_T)/p_T = 0.2$. Importantly, it is on par with the resolution of DØ's central tracker in the forward region where the full coverage of the fiber tracker's layers has ended.

8.6.4 Forward Muon System Scintillation Counters

Three layers of "Pixel" scintillation counters [58] are added to the forward region (approximately $1.0 \leq |\eta| \leq 2.0$). Their primary role is muon triggering. The ~ 4800 pixel counters have segmentation $0.1 \times 4.5°$ in $\Delta\eta \times \Delta\phi$. Most of the trapezoidal shaped pixel counters are made from 0.5" thick Bicron scintillator with wavelength shifting bars. They are each read out by a single PMT. The counters are held in protective aluminum containers with a steel fastener, on one corner, which mates to the magnetic shield of the PMT. A few of

the counters have special space constraints and are made with wavelength shifting fiber so as to allow more flexibility in the orientation of the PMT and magnetic shield. The same kind of LED pulser calibration system used in the central muon scintillators is used for the Pixel counters.

The counters are assembled into octants of ~ 100 counters each. The octants provide mechanical support for the counters and their infrastructure. These are mounted directly onto the A- and B-layer sides of the forward toroid magnets and onto the inside face of the C-layer support frame. Two octants are shown in Fig. 8.10.

Forward muon triggers are formed from coincidences in the three layers of scintillation counters consistent with a muon of a given momentum. The MDT's provide a p_T measurement at trigger level, especially important in the fiducial region where the fiber tracker has reduced coverage.

8.6.5 Shielding

The purpose of shielding is to shield the muon detectors from backgrounds generated at high $|\eta|$ from the interaction of the beam jets with forward elements of the detector and accelerator hardware, such as the beampipe and low-beta quadrupole magnet. The shielding is built in several large, movable sections extending from the endcap calorimeters, through the forward toroid magnets, to the Tevatron tunnels. The shields themselves totally contain the accelerator elements within the collision hall, including the low-beta quadrupole magnet, inside a case of 20 inches of iron, six inches of polyethylene, and two inches of lead. The shielding is shown in Figs. 8.5, 8.6.

8.7 Trigger

One of the defining features of hadron collider physics is the necessity to select the small fraction of all bunch crossings containing interesting collisions. A fast selection process,

called the "trigger", sorts events into categories of various levels of interest. An event that passes the trigger is written to magnetic tape for later analysis. An event that fails the trigger is lost forever. An event can fail to pass the trigger because the collision was a well understood process, because the event was mistaken for a well understood process (trigger inefficiency), or because the trigger or data acquisition were busy processing previous collisions (dead time).

There are three trigger levels. After Level-1 trigger, the event rate is reduced from 7 MHz to 10 KHz. Level-2 trigger reduces the event rate 10 times more. We can further reduce the event rate 20 times by the Level-3 software trigger. After Level-3, 50 events are written to tape per second.

8.7.1 Trigger Level-1

The first element of the trigger is the formation of trigger primitives. These are collections of a few bits of data that represent the status of various detector elements. For example, one set of trigger primitives are the calorimeter cells with energy above a particular threshold. Another would be which muon chambers have detected a particle, and whether this particle is consistent with a high p_T muon, a low p_T muon, or neither. Another would be the number and position of tracks found in the outer tracker (silicon is not in the trigger at this stage).

A limited amount of processing is then applied to these trigger primitives. Typically, this is performed in Field Programmable Gate Arrays (FPGA's) with inputs from the front-end detector electronics. In DØ, for instance, Level-1 muon primitives are formed from combinations of in-time hits in scintillation counters, coincidences of hit cells in the drift chambers, and tracks formed from hit patterns in the axial scintillating fibers of the central tracker.

The primitives are sent to the global Level-1 trigger. Combinations of trigger primitives are compared against a runtime programmable list containing the definitions of triggers to be used in the run. The DØ Level-1 trigger system can support up to 128 different unique

triggers. If the trigger primitives satisfy at least one of the triggers, the event is passed to the next trigger level. A block diagram of DØ's trigger is shown in Fig. 8.11.

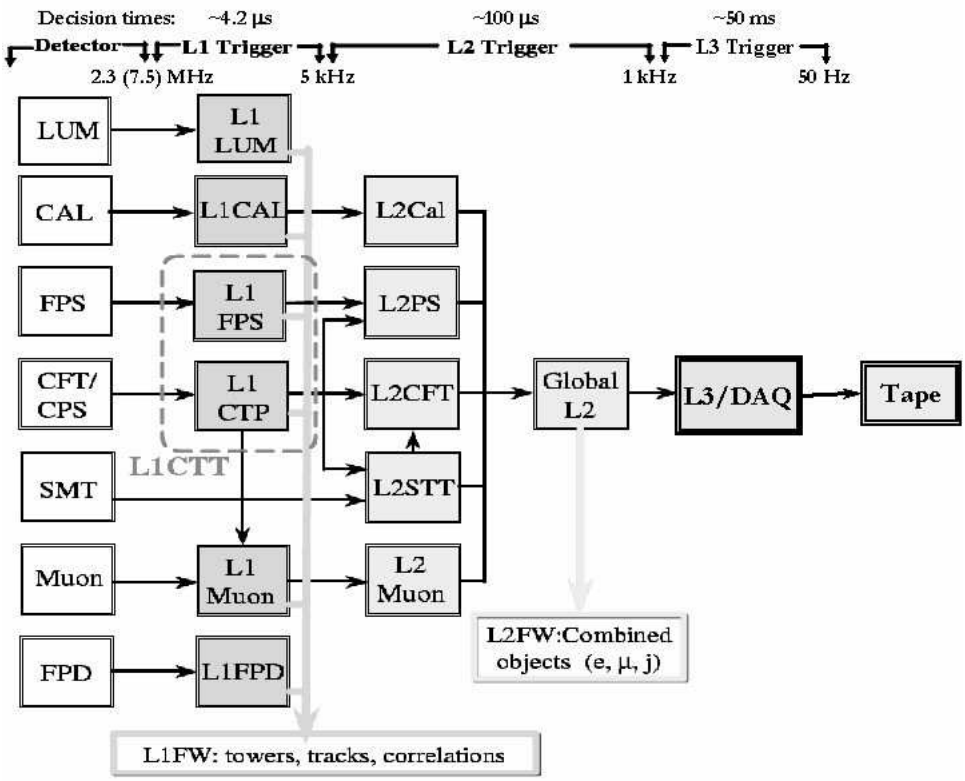

Figure 8.11: Design of the DØ trigger system.

It takes time to form the primitives and to make a Level-1 trigger decision. Meanwhile collisions continue to occur. Since the trigger needs to be ready for the next crossing while it is processing an event, the data from the detectors is placed in a pipeline (a microprocessor's "assembly line" for executing program instructions; a pipelined function unit in a processor separates the execution of an instruction into multiple stages) which increments every crossing.

The DØ Level-1 trigger has a deadtimeless output rate of 10 kHz. If any single one of the 128 combinations is positive, and the DAQ system is ready for acquisition, then the

Level-1 framework issues an accept, and the event data is digitized and moved into a series of 16 event buffers to await a Level-2 trigger decision.

The central Level-1 trigger logic is performed locally in the detector octants. A muon low p_T trigger is defined using only centroids found in the A-layer, while a high p_T trigger is defined by using correlations between centroids found in the A-layer and B- or C-layer. Four thresholds (2, 4, 7 and 11 GeV/c) are defined using the CFT information. The information for each octant in each region is combined in the muon trigger manager, which produces global muon trigger information. The muon trigger manager makes a trigger decision based on the p_T threshold (2, 4, 7 and 11 GeV/c), pseudorapidity region ($|\eta| < 1.0, |\eta| < 1.5$ and $|\eta| < 2.0$), quality (Loose, Medium and Tight) and multiplicity information. This trigger decision is sent to the Level-1 Trigger Framework where it is included in the global physics trigger decision.

8.7.2 Trigger Level-2

At Level-2, the Level-1 decision is confirmed, or not, using the additional time to provide more and better information. This is done in two stages. The first stage, called the preprocessor stage, uses FPGA's to refine the trigger primitives found by Level-1 and to prepare the data for the second stage. The second stage, called the global processor stage, combines and correlates information from the trigger primitives.

The preprocessor FPGA's have about 50 μs to perform refinements to the trigger primitives. For example, the first stage photon primitive, formed from a single tower at Level-1, is required to have a shape that looks like an isolated electromagnetic shower at Level-2. The additional time is used to compare the energy of the tower of interest with nearby towers. Additional related information can also be used, such as energy in the shower maximum. Because of the increased accuracy of the measurement, thresholds can be set tighter in Level-2, producing a great deal of the rejection in the global processor stage.

The global processor stage for DØ is a VME-based CPU card using a Digital Alpha

processor. Using a general purpose CPU at this level of the trigger provides a great deal of flexibility – essentially all of the Level-1 primitives are available at Level-2, where they can be combined in ways not possible at Level-1. For instance, Level-1 can produce photon triggers and it can produce jet triggers. However, Level-2 provides the ability to correlate the two in ways not possible by the dedicated hardware of Level-1. For example, requiring that the jet be opposite the photon in ϕ and having similar E_T. This can be used to select events of a given topology with particularly interesting kinematics, for example. Perhaps more importantly, though, is that this design provides added flexibility for implementing new triggers during the Run II even if they have not been anticipated before the run begins. This might be in response to better than promised luminosity from the accelerator, or it might be in response to early physics results.

Level-2 is where the information from the silicon vertex trigger (SVT) becomes available. Layers of silicon are read out into this trigger, which uses an associative memory and roads provided from the outer tracker to identify silicon tracks. This provides improved momentum resolution, but more importantly, it also provides impact parameter resolution for each track sufficient to identify particles from displaced vertices. Since the vast majority of two track triggers are not from heavy flavor decay, the SVT provides three orders of magnitude rejection. Silicon information doesn't just improve the impact parameter resolution, it also improves the momentum resolution, because the two tend to be highly correlated. The maximum deadtimeless output rate of Level-2 is about 1000 Hz at DØ.

By shifting a 3-tube wide window over all the cells in an octant, and looking for wire triplets with a matching scintillator hit, the muon preprocessor first finds track stubs separately in the A-layer and the BC-layer. The track stubs found are reported to an ALPHA preprocessor board that matches track stubs in the A layer with that in the BC-layer, and creates Level-2 objects from matched or unmatched stubs. These Level-2 objects hold the ϕ, η and p_T of the muon, and are reported to the Level-2 global processor. Upon a Level-2 Accept, the Level-2 objects are sent to Level-3 for more precise muon track reconstruction.

8.7.3 Trigger Level-3

The third level trigger is often described as an event filter. It is a software-based system characterized by parallel data paths that transfer data from the detector front-end crates to a farm of processors. It reduces the input rate of 1 kHz to an output rate of 50 Hz.

DØ's farm of 500 parallel commodity CPU's builds the event into the offline format, runs a modified (for faster execution time) version of the offline reconstruction on the event, and makes a decision to accept or reject the event. If the event is accepted, it is already in or close to the proper format for offline analysis. Additionally, this trigger level can be used to characterize the event and decide whether an event should receive priority in reconstruction. Reconstructing a small fraction (say 1%) of events in an "express stream" can be used to provide rapid feedback on the detector's performance and . The overall output rate of Level-3 is about 50 Hz, with some variation depending on luminosity and dataset selection requirements.

Running what is effectively the offline reconstruction online also provides an excellent monitor of the health of the experiment. The full offline reconstruction lags a day or two behind the data taking in order to use the final calibration constants, but the Level-3 reconstruction lags only a fraction of a second. Serious problems can therefore be detected before a large amount of data is collected. As an additional benefit, because Level-3 looks at the output of Level-2 and offline looks at the output of Level-3, monitoring at Level-3 examines many times more events than offline monitoring, also improving the probability to spot trouble sooner.

Using commodity processors has a number of advantages. First, the nature of an event filter naturally lends itself to parallel processing: each CPU processes an entire event, with a supervisor process assigning incoming events to CPUs that finish their events and become ready for new ones. Second, these computers are inexpensive, and getting more so with time, and finally, the system is highly expandable: additional CPU's can be added at a later date, until the bandwidth into Level-3 becomes the limiting factor.

The muon Level-3 trigger utilize some aspects of the offline muon reconstruction. Level-3 muons have more complete information on the vertex and inner tracking components that will improve momentum resolution, and has the ability to require that multiple muons come from the same vertex. Similar fits are done in Level-1 as in the final offline reconstruction. Requirements on matching the muon track to the inner tracking can reduce remnant combinatorics plus punchthroughs. Level-3 also uses the calorimeter information to reduce combinatorics, and separate muons into isolated and non-isolated. Level-3 improves on Level-2's ability to separate muon sources into prompt, slow, or out-of-time by fitting the available scintillator hits along a track to the particle's velocity. Level-3 can remove a cosmic ray muons both by their being out-of-time and by looking for evidence of a penetrating track on the opposite side of the detector. Level-3 can also clean up single muon events that Level-1 and Level-2 identified as dimuons, such as those which pass through the FAMUS–WAMUS overlap region.

8.7.4 *B* Triggers with DØ

B-hadron observability depends strongly on the detector capabilities to trigger on soft lepton(s) present in semi-leptonic channel or on J/ψ's produced in B decays. Hadronic B triggers are not considered in the following.

The Level-1 muon hardware trigger is based on the combination of low p_T track candidates measured in the CFT, spatially matched with hits in the scintillator planes and/or drift chambers. Single muon events with $p_T^\mu > 4$ GeV/c run prescaled currently, and dimuons with $p_T^\mu > 2$ GeV/c are expected to run unprescaled.

The electron trigger is aimed at soft electron pair detection. Level-1 candidates are selected separately in EM calorimeter trigger towers ($\Delta\eta = \Delta\varphi = 0.2$) with a transverse energy deposit $E_T > 2.0$ GeV, and in the tracking system with a low p_T track coincident with pre-shower cluster. Electron candidates of both systems are then required to match within a quadrant in φ and to have opposite signs. These electron triggers are not used in the following analysis.

Level-2 triggers include setting of the invariant mass window and angular cuts in di-lepton channels to select J/ψ decays and improve background rejection.

8.8 Data Acquisition

The data flow in trigger Level-3/data acquisition is illustrated in Fig. 8.12. Events are reconstructed on the FNAL processor farm system, with that portion dedicated to DØ capable of matching the 50 Hz data acquisition rate. Following reconstruction, data are stored on a tightly coupled disk and robotic tape system, and made available for analysis on a centralized analysis processor.

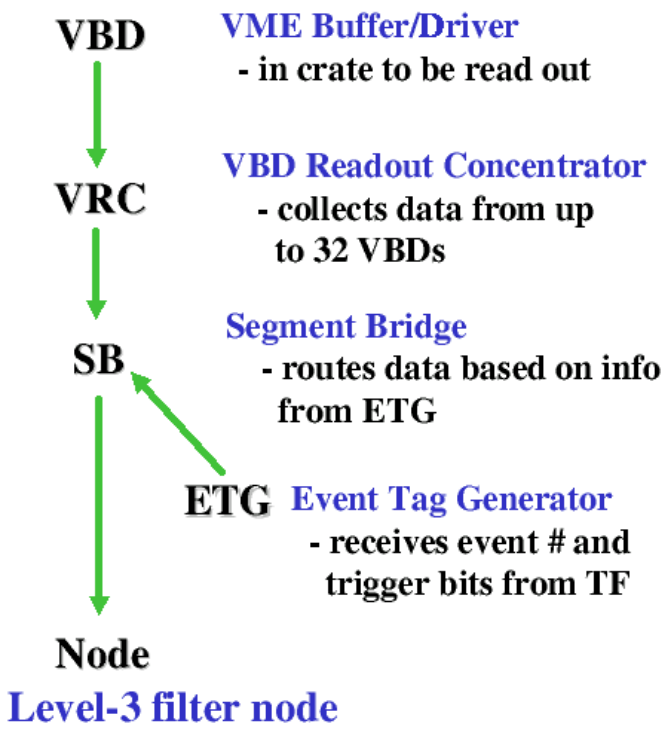

Figure 8.12: Simplified data flow in Level-3/DAQ for DØ Run II.

Chapter 9

Establishing the Λ_b^0 Signal

9.1 Data and Monte Carlo Event Samples

The data used corresponds to an integrated luminosity of approximately 225 pb^{-1} collected between April 2002 and January 2004. This analysis is described in Ref. [68] and repeated in Ref. [69].

9.1.1 Dimuon data sample

The data used in this analysis was part of a skim that was called the "D" skim, which included either D mesons for semileptonic studies or J/ψ's for exclusive channels. The dimuon requirements on this skim are:

- two muons with opposite charge;
- $p_T > 1$ GeV for each muon;
- number of CFT hits > 1 for each particle;
- at least 1 muon with $nseg = 3$; $nseg$ is a muon quality cut that describes the hits in the muon detector layers.
- for $nseg > 0$, $p_T(\mu) > 1.5$ GeV; for $nseg = 0$, $p_T > 1$ GeV;
- 2.5 GeV $<$ Mass$(\mu^+\mu^-) <$ 3.6 GeV;

- for a muon with $nseg = 0$:
  - $p_T(\mu^+\mu^-) > 4.0$ GeV;
  - $p(\mu) < 7$ GeV;
  - p_T of second muon > 2.5 GeV; and
  - χ^2 of global muon track fit < 25 for both muons.

9.1.2 Primary vertex reconstruction

To determine the primary vertex, the AATrack package [61] is used:

```
AATrack v0-10-06-01
beam spot file version 2.09
```

that follows the procedure as outlined in Ref. [62]. A primary vertex is determined for each event by minimizing a χ^2 function that depends on all the tracks in the event and a term that represents the beam spot constraint. The beam spot is the run-by-run average beam position, where a run typically lasts several hours. The beam spot is stable during the periods of time when the proton and the antiproton beams are kept colliding continously, and can be used as a constraint for the primary vertex fit. The initial primary vertex candidate and its χ^2 are obtained using all tracks. Next, each track used in the χ^2 calculation is removed temporarily and the χ^2 is calculated again; if the χ^2 decreases by 9 or more, this track is discarded from the PV fit. This procedure is repeated until no more tracks can be discarded. The PV resolution achieved by using this procedure is 25 μm.

9.1.3 Secondary vertex reconstruction

To reconstruct secondary vertices (i.e., J/ψ, Λ and Λ_b^0 vertices), the BANA package [63] is used.

9.1.4 Λ_b^0 Candidate Selection

Further cuts are used to select J/ψ mesons:

- Require that a primary vertex reconstructed.
- For dimuons forming a vertex, require:
  - distance from primary vertex to J/ψ vertex < 10 cm.
  - Limited number of track measurements downstream (< 1) of the vertex and missed hits upstream (< 5) of the vertex.
- 2.8 GeV $<$ Mass$(\mu^+\mu^-) <$ 3.35 GeV; and
- number of SMT hits for each muon $>= 1$.

Figure 9.1 and Fig. 9.2 show the $(\mu^+\mu^-)$ invariant mass for all inclusive events and for events containing a Λ candidate, respectively.

To select $\Lambda \to p\pi^-$ candidates, we require:

- two oppositely charged tracks forming a vertex;
- the higher momentum track is assumed to be the proton;
- limited number (< 1) of track measurements downstream of the vertex;
- number of CFT hits ≥ 1 for each track;
- 1.105 GeV $<$ Mass$(p\pi) <$ 1.125 GeV;
- $p_T(\Lambda) > 0.4$ GeV; and
- Λ candidates falling within a K_S^0 mass window of 0.465 GeV $<$ Mass$(\pi^+\pi^-) <$ 0.52 GeV are removed.

Figure 9.3 shows the invariant mass of $(p\pi)$ for all events containing a J/ψ candidate.

Once good J/ψ and Λ candidates have been found in the same event, the two muons from J/ψ are combined with the reconstructed neutral Λ track to form a Λ_b^0 vertex. Further requirements are made on the vertex:

- vertex $\chi^2(\Lambda_b) < 10$;
- $p(\Lambda_b^0) > 5$ GeV;
- xy distance from J/ψ vertex to Λ vertex > 0.3 cm;
- assuming that the higher momentum track is the proton, $p(p) > 0.8$ GeV; and
- collinearity of $\Lambda_b^0 > 0.99$, where collinearity is defined as the cosine of the angle between the momentum of Λ_b^0 in the xy plane and the direction from primary to secondary in the xy plane.

Figure 9.4 shows the invariant mass of $(\mu^+\mu^-\Lambda)$ subject to the above cuts. The signal is modeled with a Gaussian function, and the background by a constant plus an exponential function. The exponential function is taken for the fact that there is a large shoulder on the left of the signal due to partially reconstruced B mesons. The number of signal events extracted from the fit is 48±11 with a mean of 5630±10 MeV and a width of $\sigma = 39\pm8$ MeV.

To check the validity of the signal for the presence of long lived signal for lifetime measurement purposes, the decay length cut and decay length significance cut were varied. Figure 9.5 shows the decay length and decay length significance in data.

A transverse signed decay length is defined using the vector between the Λ_b^0 vertex and the primary vertex, $\vec{L}_{xy} = \vec{x}_{\Lambda_b} - \vec{x}_{PV}$, and forming: $L_{xy} = (\vec{L}_{xy} \cdot \vec{p}_T(\Lambda_b))/|\vec{p}_T(\Lambda_b)|$.

Figures 9.6, 9.7, and 9.8 show the invariant mass of the $\mu^+\mu^-\Lambda$ system subject to the above cuts and adding $L_{xy} > 0.01$ cm, $L_{xy} > 0.02$ cm, and $L_{xy} > 0.03$ cm requirements, respectively. The number of signal events extracted from the fit in each case is 33 ± 8,

33 ± 7, and 31 ± 6, respectively, with the signal-to-noise increase in each case as expected for a signal with lifetime.

Figures 9.9 and 9.10 show the invariant mass of the $\mu^+\mu^-\Lambda$ system subject to the above cuts and adding $L_{xy}/\sigma(L_{xy}) > 2$ and > 4, respectively. The number of signal events extracted from each fit is 37 ± 8 and 31 ± 6, respectively, with increased signal-to-noise, again indicating lifetime information in the signal.

Figures 9.11, 9.12, and 9.13 show the invariant mass of the $\mu^+\mu^-\Lambda$ system subject to the above cuts and adding proper lifetime cuts $c\tau > 370$ μm, $c\tau > 740$ μm, and $c\tau > 1000$ μm requirements, respectively. The number of signal events extracted from the fit in each case is 18 ± 5, 7 ± 3, and too small to allow a fit, respectively. This fractional event loss is consistent with the signal having a lifetime of the order of a B hadron.

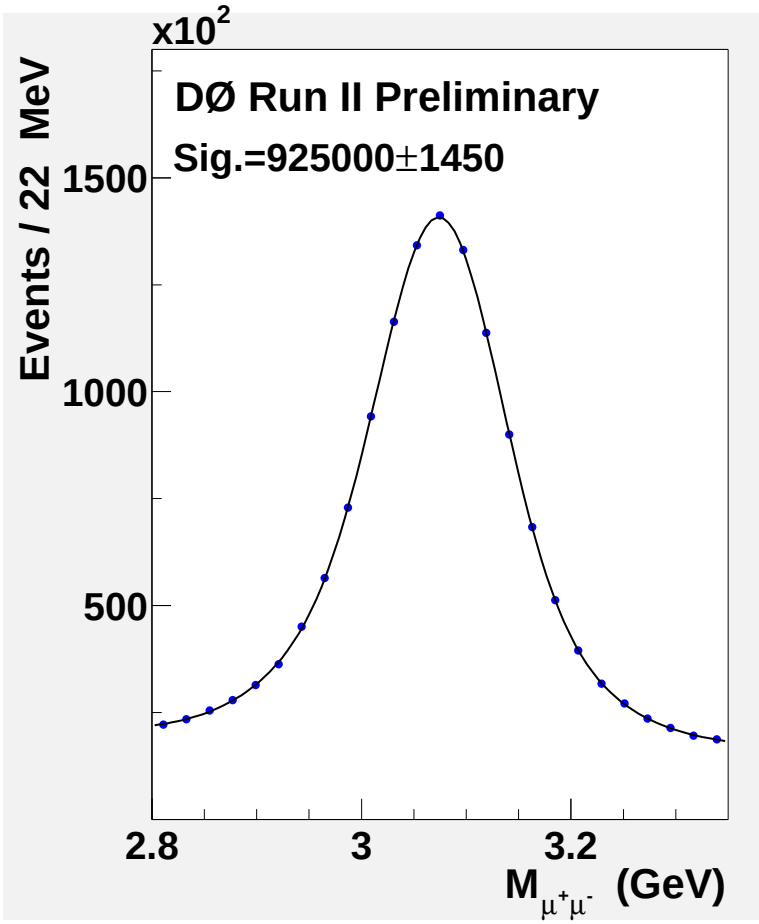

Figure 9.1: Invariant mass distribution of the $(\mu^+\mu^-)$ system for all the events. The signal is described by a double Gaussian function and the background by a second order polynomial. The signal mean is 3070.0 ± 0.1 MeV and the fitted widths are $\sigma_1 = 55 \pm 1$ MeV and $\sigma_2 = 100 \pm 1$ MeV.

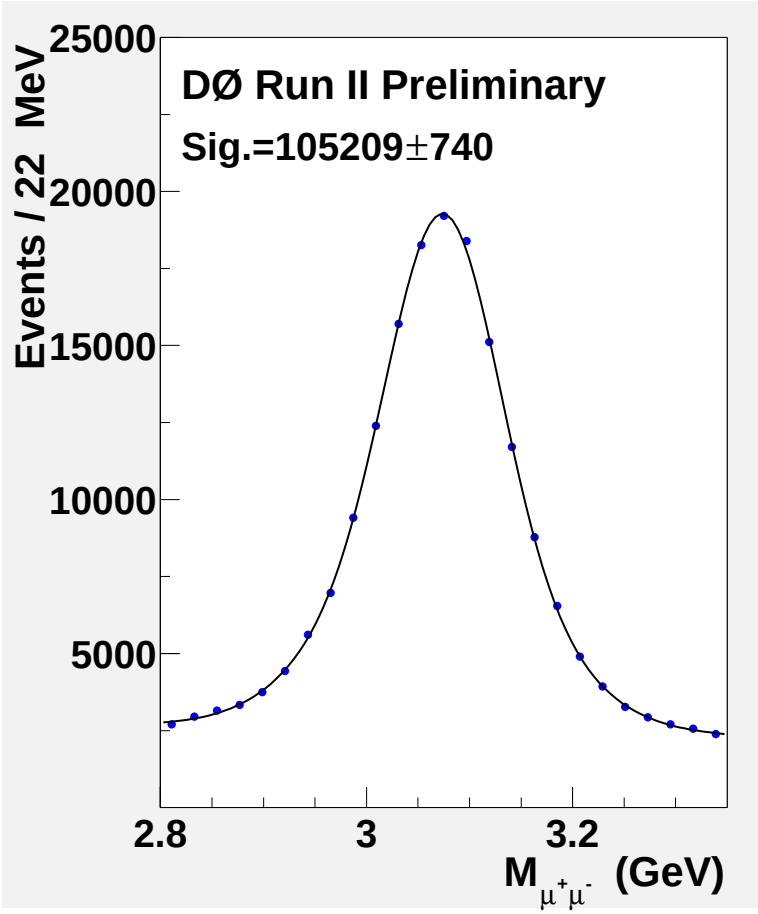

Figure 9.2: Invariant mass distribution of the $(\mu^+\mu^-)$ system for all the events containing a Λ candidate. The signal is described by a double Gaussian function and the background by a second order polynomial. The signal mean is 3069 ± 1 MeV and the fitted widths from double Gaussian function are $\sigma_1 = 52 \pm 1$ MeV and $\sigma_2 = 91 \pm 5$ MeV.

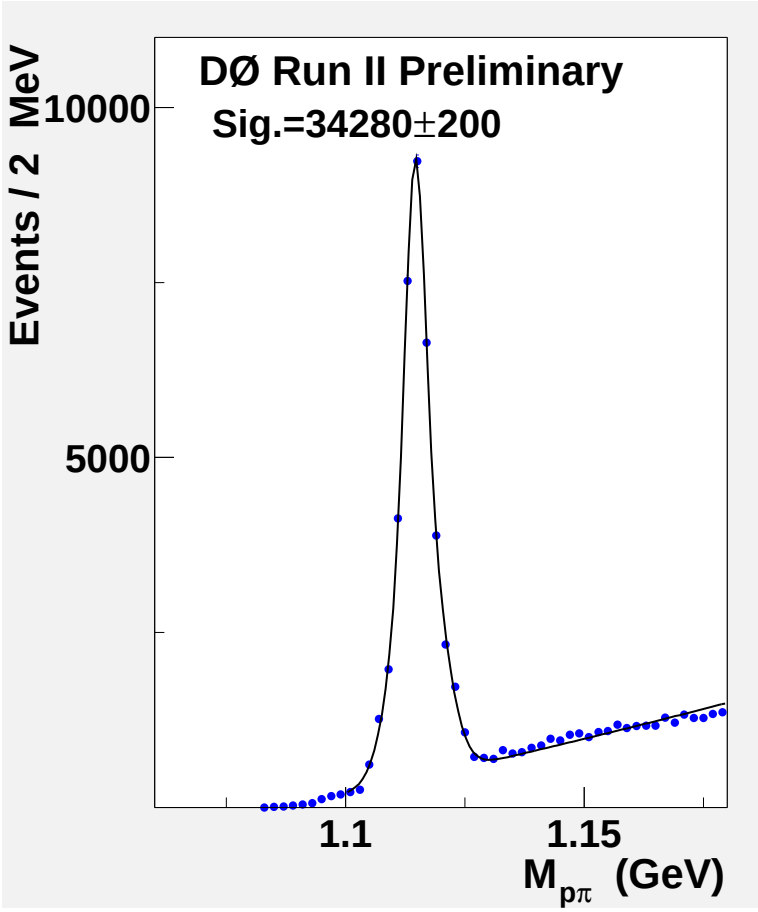

Figure 9.3: Invariant mass distribution of the (p, π) system for all the events containing a J/ψ candidate. The signal is described by a double Gaussian function and the background by a second order polynomial. The signal mean is 1115.3 ± 0.1 MeV and the fitted widths are $\sigma_1 = 4.6 \pm 0.1$ MeV and $\sigma_2 = 2.0 \pm 0.1$ MeV for a double Gaussian function.

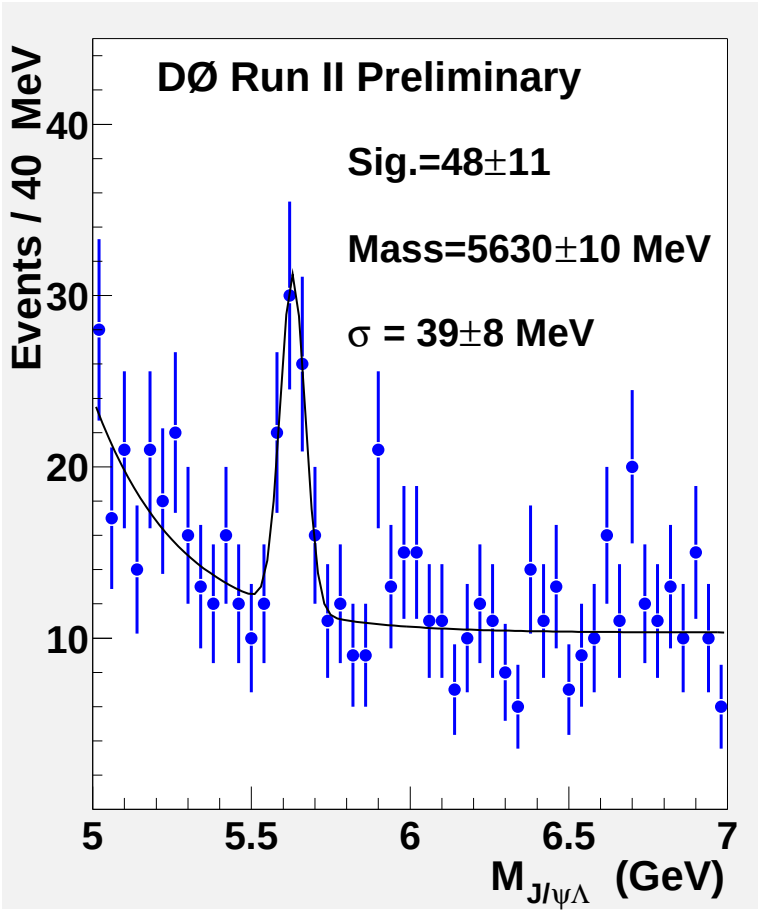

Figure 9.4: Invariant mass distribution of the $(J/\psi, \Lambda)$ system for all Λ_b^0 candidates. The signal is described by a Gaussian function and the background by a constant plus an exponential function.

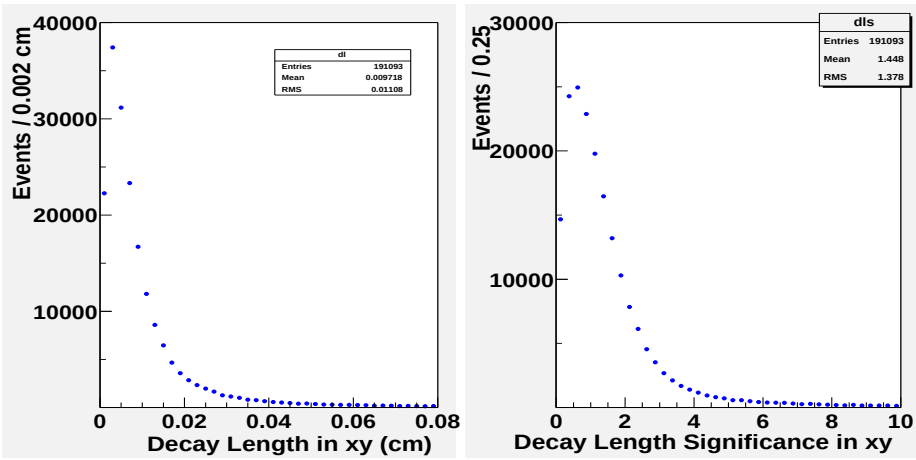

Figure 9.5: Top: decay length distribution; and bottom: decay length significance distribution for data.

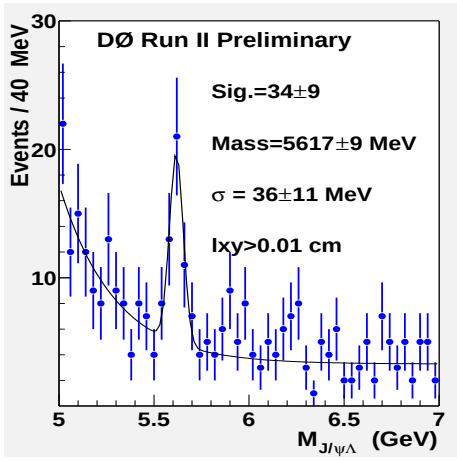

Figure 9.6: Invariant mass distribution of the $(J/\psi, \Lambda)$ system for all Λ_b^0 candidates plus the requirement $L_{xy} > 0.01$ cm. The signal is described by a Gaussian function and the background by a constant plus an exponential function.

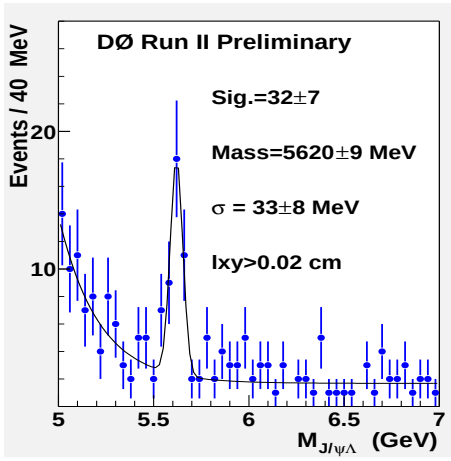

Figure 9.7: Invariant mass distribution of the $(J/\psi, \Lambda)$ system for all Λ_b^0 candidates plus the requirement $L_{xy} > 0.02$ cm. The signal is described by a Gaussian function and the background by a constant plus an exponential function.

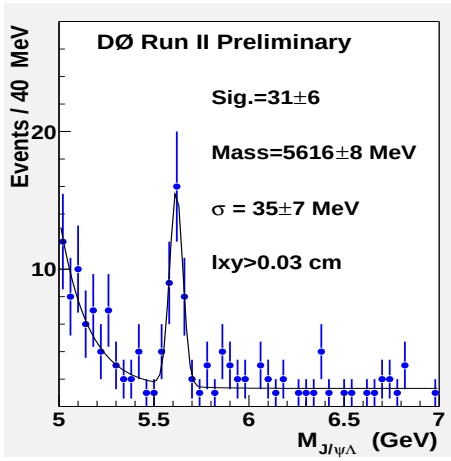

Figure 9.8: Invariant mass distribution of the $(J/\psi, \Lambda)$ system for all Λ_b^0 candidates plus the requirement $L_{xy} > 0.03$ cm. ehe signal is described by a Gaussian function and the background by a constant plus an exponential function.

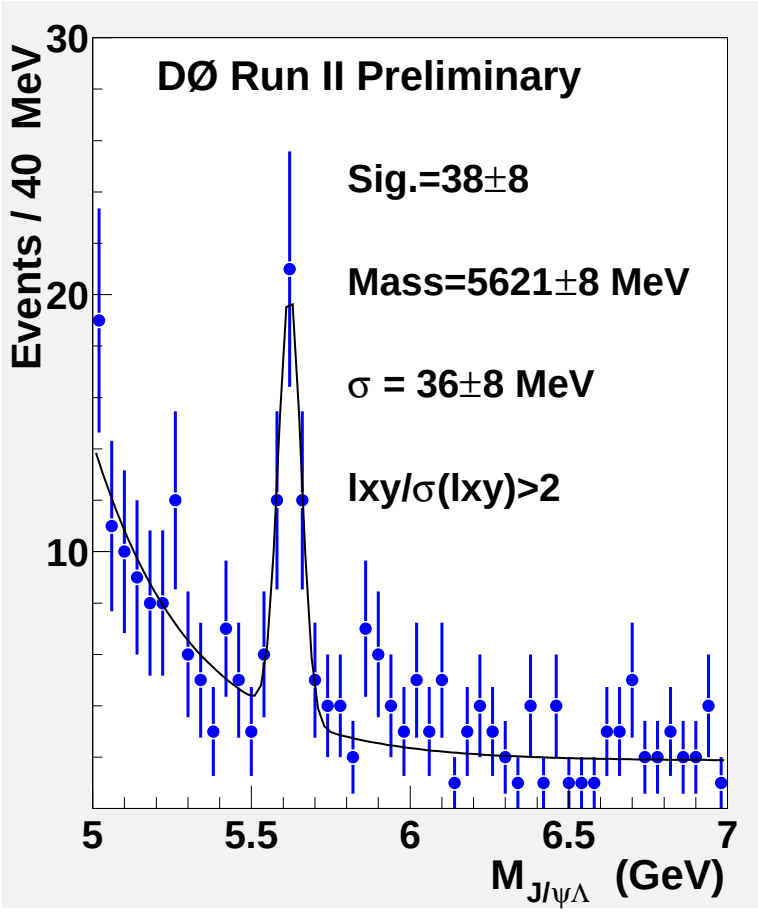

Figure 9.9: Invariant mass distribution of the $(J/\psi, \Lambda)$ system for all Λ_b^0 candidates plus the requirement $L_{xy}/\sigma(L_{xy}) > 2$. The signal is described by a Gaussian function and the background by a constant plus an exponential function.

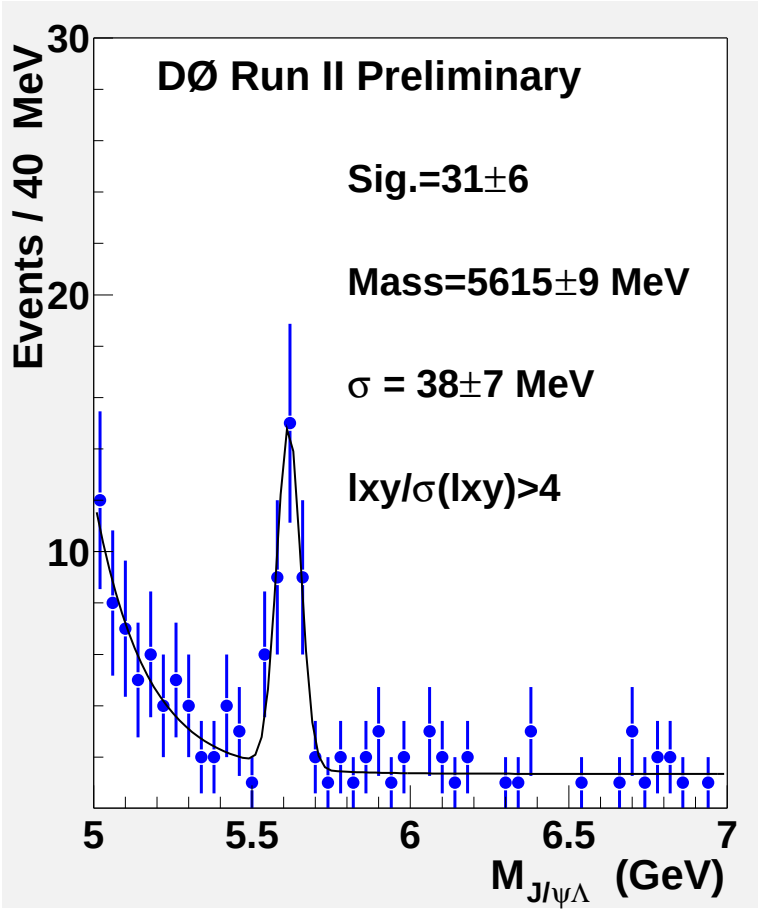

Figure 9.10: Invariant mass distribution of the $(J/\psi, \Lambda)$ system for all Λ_b^0 candidates plus the requirement $L_{xy}/\sigma(L_{xy}) > 4$. The signal is described by a Gaussian function and the background by a constant plus an exponential function.

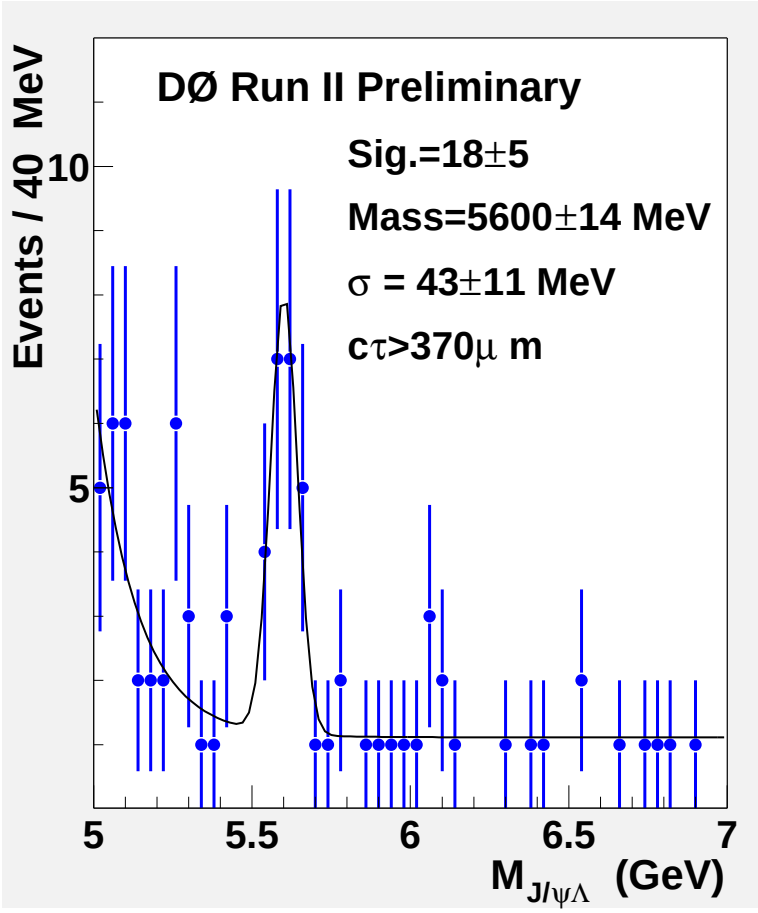

Figure 9.11: Invariant mass distribution of the $(J/\psi, \Lambda)$ system for all Λ_b^0 candidates plus the requirement $c\tau > 370$ μm. The signal is described by a Gaussian function and the background by a constant plus an exponential function.

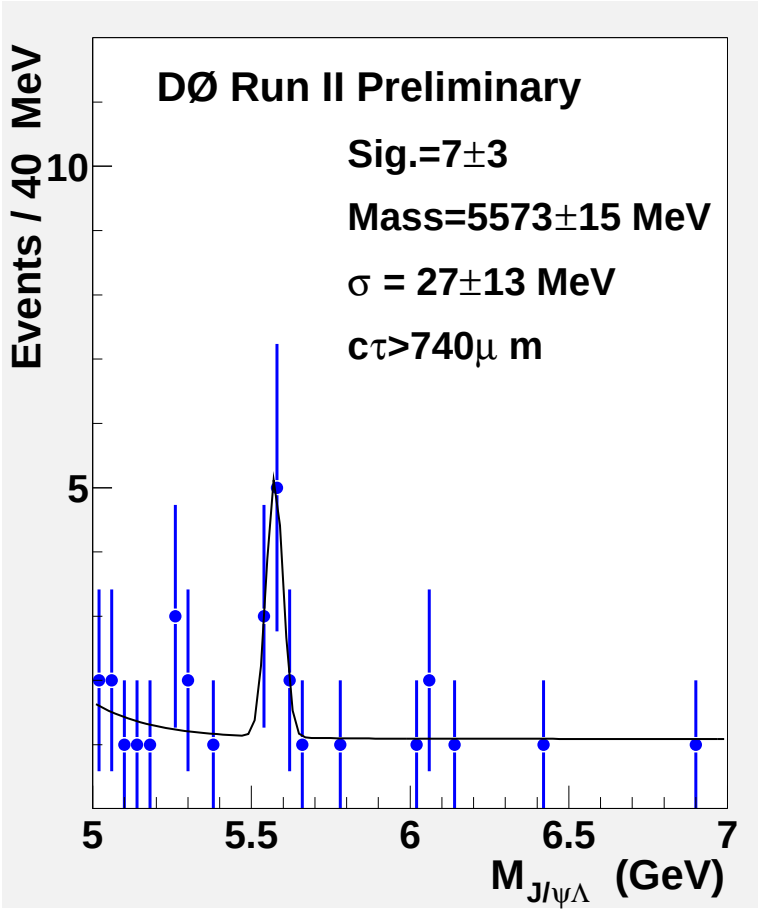

Figure 9.12: Invariant mass distribution of the $(J/\psi, \Lambda)$ system for all Λ_b^0 candidates plus the requirement $c\tau > 740$ μm. The signal is described by a Gaussian function and the background by a constant plus an exponential function.

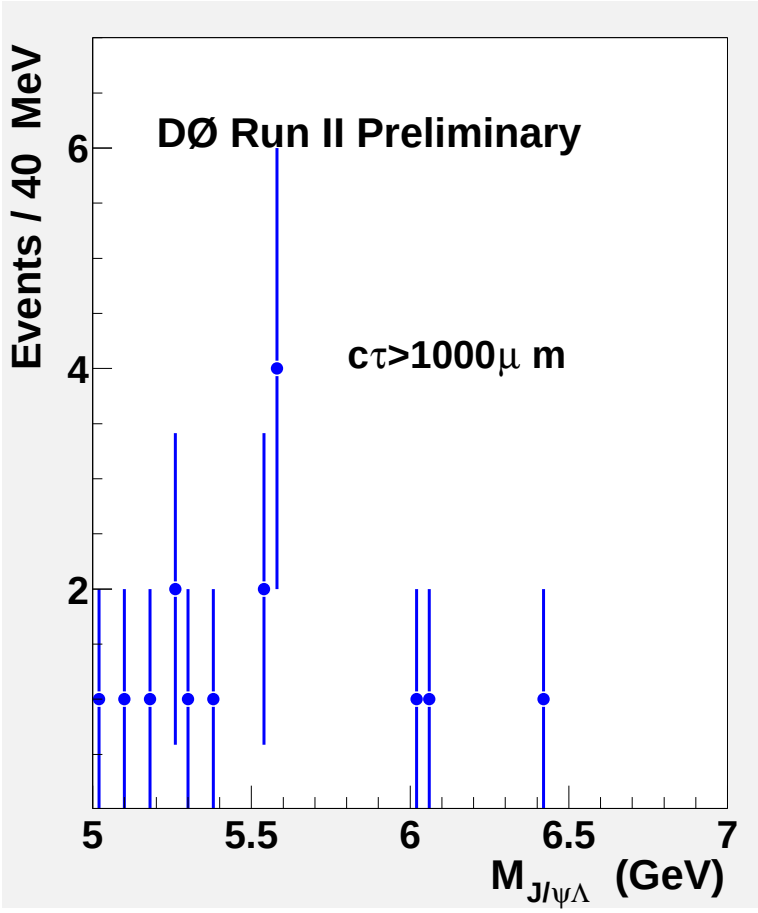

Figure 9.13: Invariant mass distribution of the $(J/\psi, \Lambda)$ system for all Λ_b^0 candidates plus the requirement $c\tau > 1000$ μm. The signal is described by a Gaussian function and the background by a constant plus an exponential function.

9.1.5 Monte Carlo event samples

9.1.6 MC Signal $\Lambda_b^0 \to J/\psi\Lambda$

To simulate the decay chain $\Lambda_b^0 \to J/\psi\Lambda$, $J/\psi \to \mu^+\mu^-$, $\Lambda \to p\pi^-$, we use the `evtgen` decay model and the pythia generation program [65]. Below we show the decay file used.

```
;
DECAY  LAMB
CHANNEL  0 1.000 PSI   LAM
ENDDECAY
;
DECAY  PSI
ANGULAR_HELICITY  -1   1.  0.  1.
ANGULAR_HELICITY   0   1.  0. -1.
ANGULAR_HELICITY   1   1.  0.  1.
CHANNEL  40 1.000 MU+   MU-
ENDDECAY
;
DECAY  LAM
CHANNEL  0 1.000  P+    PI-
ENDDECAY
;
```

Before passing the generated events through the suite of programs for the detector simulation, hit simulation, trigger simulation, and track and particle reconstruction, we apply the following "pre-GEANT" selection cuts using the d0mess package [66]:

- presence of the decay chain $\overline{\Lambda_b^0} \to J/\psi\overline{\Lambda}$.
- $p_T(\mu) > 1.5$ GeV and $0.8 < |\eta| < 2.0$ or $p_T(\mu) > 3$ GeV and $0.8 < |\eta|$.

"GEANT" is a detector simulation tool, and is described in detail in Ref. [67].

We apply the kinematic and quality cuts as described in the previous section. After kinematic cuts, we end up with 50000 events. Since the Λ is a long-lived particle, it decays at the GEANT processing stage, so out of 50000 events, 31500 events contain the decay $\Lambda \to p\pi^-$. The same analysis cuts as data are applied. The number of events passing all event selection criteria is 315. The reconstruction efficiency after the kinematic cuts is $\epsilon = (1.0 \pm 0.06)\%$. Figure 9.14 shows the invariant mass of the combination $(\Lambda, J/\psi)$ for the Monte Carlo sample. The mass and the width observed in MC are M$(\Lambda, J/\psi)$ =5642 $\pm$ 2 MeV and $\sigma = 35 \pm 2$ MeV respectively. The mass is slightly lower in data compared to MC due to uncertainty in DØ momentum scale, and the fitted width observed in data is consistent with that obtained in the MC.

Figure 9.15 shows the decay length and decay length significance distribution from the MC within the mass window of Λ_b^0. These distributions clearly indicate that the signal candidates have a long lifetime component, as expected.

9.2 B_d^0 Event Selections

The decay $B_d^0 \to J/\psi K_S^0$ has similar topology to $\Lambda_b^0 \to J/\psi\Lambda$ decay and has higher statistics, making it a good test sample. Both decays are reconstructed the same way, the only difference is K_S^0 is that a reconstructed $K_S^0 \to \pi^+\pi^-$ is combined with the J/ψ instead of a Λ. To select $K_S^0 \to \pi^+\pi^-$ candidates, we require:

- two oppositely charged tracks forming a vertex;
- limited number of track measurements downstream (< 1) of the vertex;
- number of CFT hits ≥ 1 for each track;
- 0.465 GeV $<$ Mass$(\pi^+\pi^-) <$ 0.52 GeV;

- $p_T(K_S^0) > 0.4$ GeV.

Figure 9.16 shows the invariant mass of $(\pi\pi)$ for all events containing a J/ψ candidate.

Once good J/ψ and K_S^0 candidates have been found in the same event, the two muons from J/ψ are combined with the reconstructed neutral K_S^0 track to form a B_d^0 vertex. Further requirements are made on the vertex:

- vertex $\chi^2(B_d) < 25$;
- $p(B_d^0) > 5$ GeV;
- collinearity of $B_d^0 > 0.99$, where collinearity is defined as the cosine of the angle between the momentum of B_d^0 in the xy plane and the direction from primary to secondary vertex in the xy plane.

Figure 9.17 shows the invariant mass of $\mu^+\mu^-K_S^0$ subject to the above cuts. The signal is modeled with a Gaussian function, and the background by a second-order polynomial. The number of signal events extracted from the fit is 300 ± 39 with a mean of 5270 ± 5 MeV and a width of $\sigma = 38 \pm 5$ MeV.

Figures 9.18, 9.19, and 9.20 show the invariant mass of the μ^+, μ^-, K_S^0 system subject to the above cuts and adding $L_{xy} > 0.01$ cm, $L_{xy} > 0.02$ cm, and $L_{xy} > 0.03$ cm requirements, respectively. The number of signal events extracted from the fit in each case is 299 ± 30, 298 ± 25, and 278 ± 22, respectively.

Figures 9.21 and 9.22 show the invariant mass of the μ^+, μ^-, K_S^0 system subject to the above cuts and adding $L_{xy}/\sigma(L_{xy}) > 2$ and > 4, respectively. The number of signal events extracted from each fit is 300 ± 27 and 259 ± 21, respectively.

Figures 9.23, 9.24, and 9.25 show the invariant mass of the μ^+, μ^-, K_S^0 system subject to the above cuts and adding $c\tau > 460$ μm, $c\tau > 920$ μm, and $c\tau > 1320$ μm requirements,

respectively. The number of signal events extracted from the fit in each case is 153 ± 16, 60 ± 10, and 22 ± 7, respectively. These numbers are consistent with an exponentially falling B lifetime.

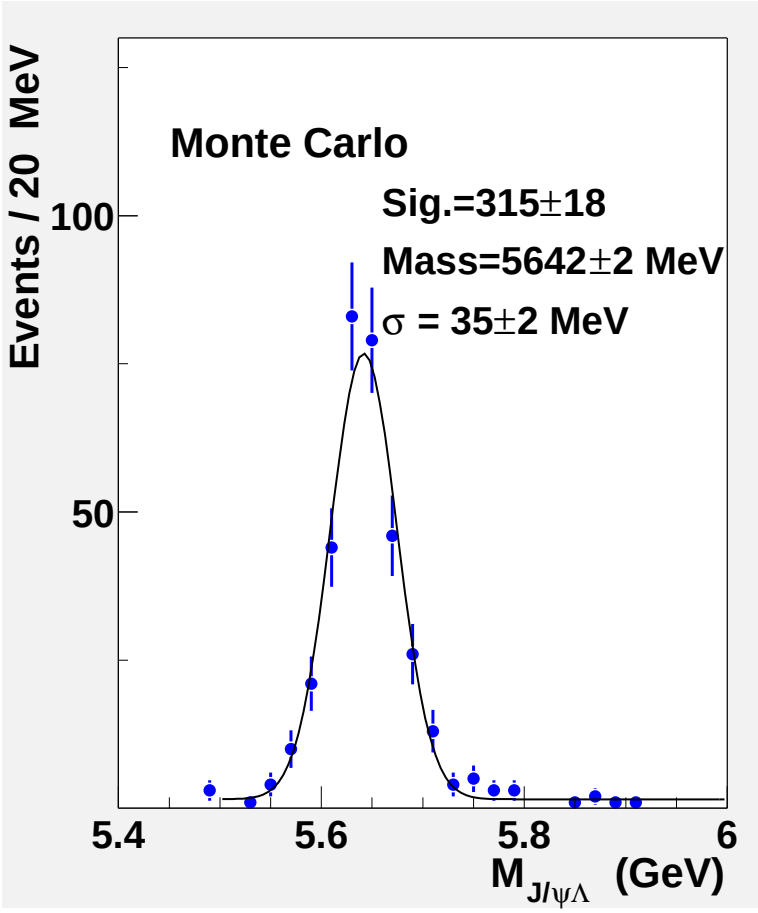

Figure 9.14: Invariant mass distribution of Λ_b^0 candidates in MC simulated events. A double Gaussian function was used to model the signal, and a constant plus an exponential function was used for the background.

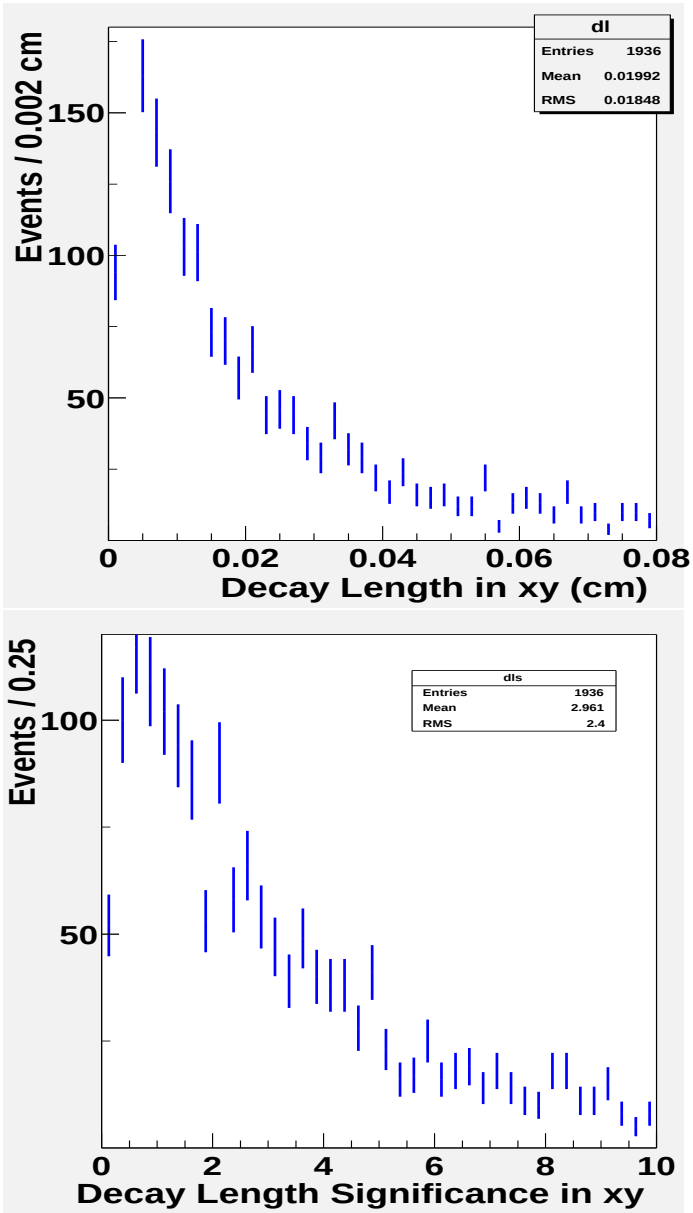

Figure 9.15: Top: decay length distribution; bottom: decay length significance distribution for MC simulated events.

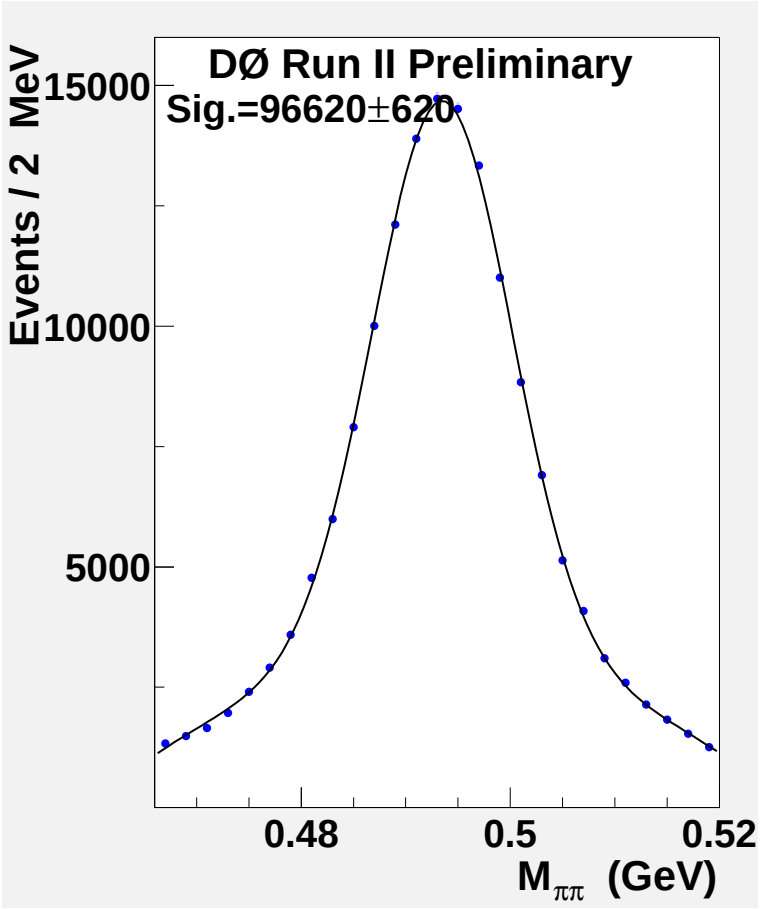

Figure 9.16: Invariant mass distribution of the $(\pi^+\pi^-)$ system for all the events with a J/ψ candidate. The signal is described by a double Gaussian function and the background by a second order polynomial. The signal mean is 493.5 ± 0.1 MeV and the fitted widths are $\sigma_1 = 5.9 \pm 0.1$ MeV and $\sigma_2 = 11.7 \pm 0.1$ MeV.

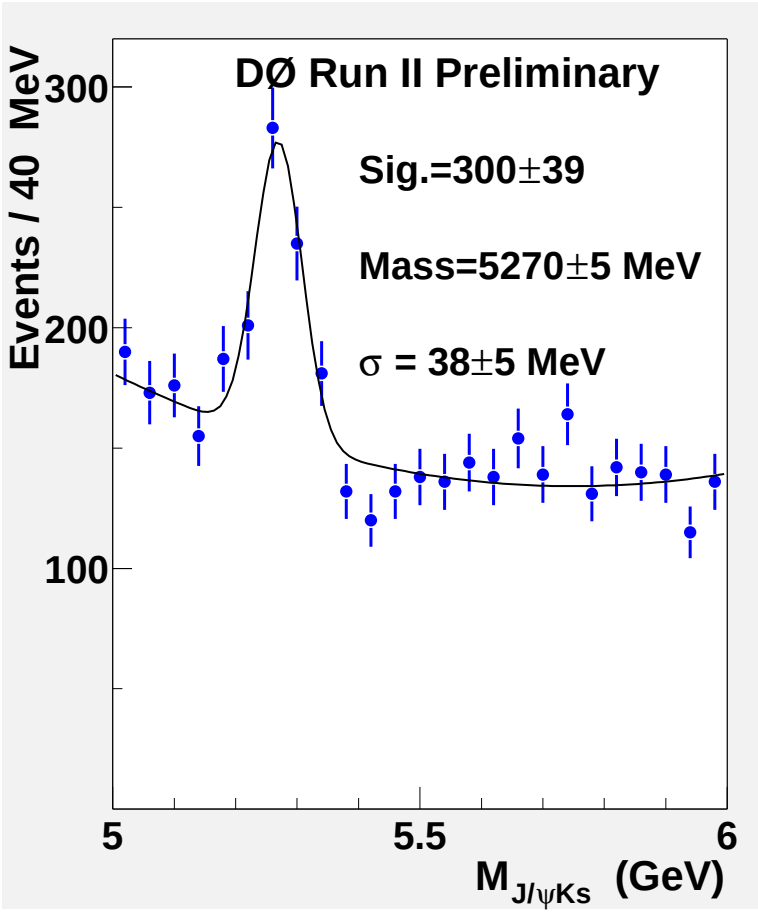

Figure 9.17: Invariant mass distribution of the $(J/\psi, K_S^0)$ system for all B_d^0 candidates. The signal is described by a Gaussian function and the background by a second order polynomial.

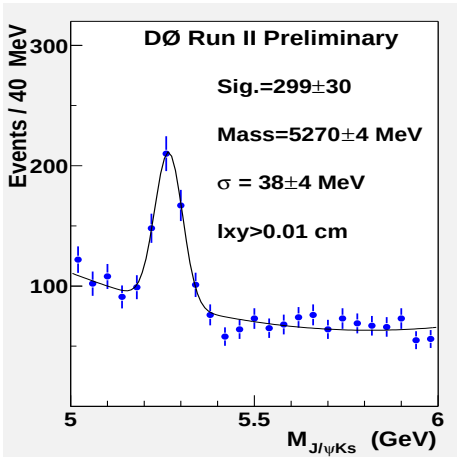

Figure 9.18: Invariant mass distribution of the $(J/\psi, K_S^0)$ system for all B_d^0 candidates plus the requirement $L_{xy} > 0.01$ cm. The signal is described by a Gaussian function and the background by a second order polynomial.

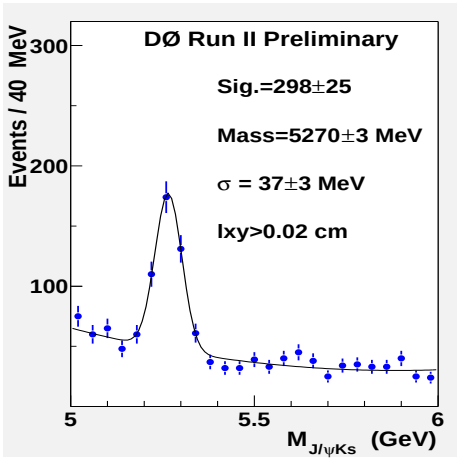

Figure 9.19: Invariant mass distribution of the $(J/\psi, K_S^0)$ system for all B_d^0 candidates plus the requirement $L_{xy} > 0.02$ cm. The signal is described by a Gaussian function and the background by a second order polynomial.

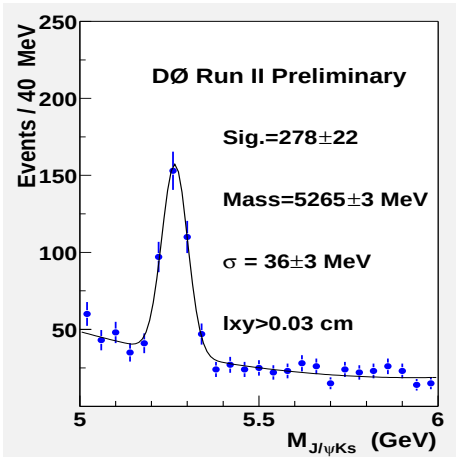

Figure 9.20: Invariant mass distribution of the $(J/\psi, K_S^0)$ system for all B_d^0 candidates plus the requirement $L_{xy} > 0.03$ cm. The signal is described by a Gaussian function and the background by a second order polynomial.

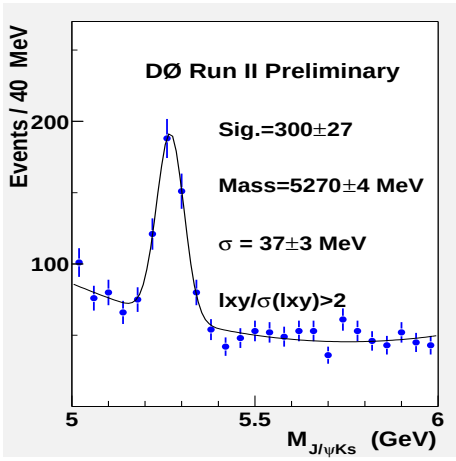

Figure 9.21: Invariant mass distribution of the $(J/\psi, K_S^0)$ system for all B_d^0 candidates plus the requirement $L_{xy}/\sigma(L_{xy}) > 2$. The signal is described by a Gaussian function and the background by a second order polynomial.

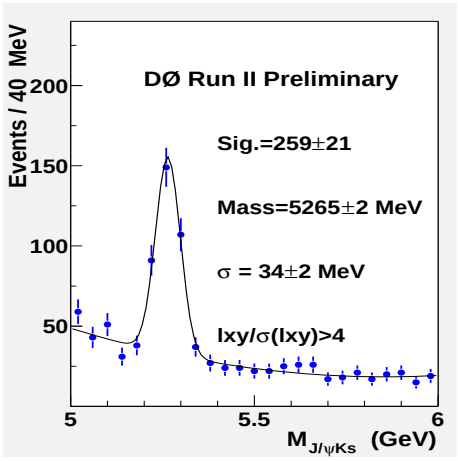

Figure 9.22: Invariant mass distribution of the $(J/\psi, K_S^0)$ system for all B_b^0 candidates plus the requirement $L_{xy}/\sigma(L_{xy}) > 4$. The signal is described by a Gaussian function and the background by a second order polynomial.

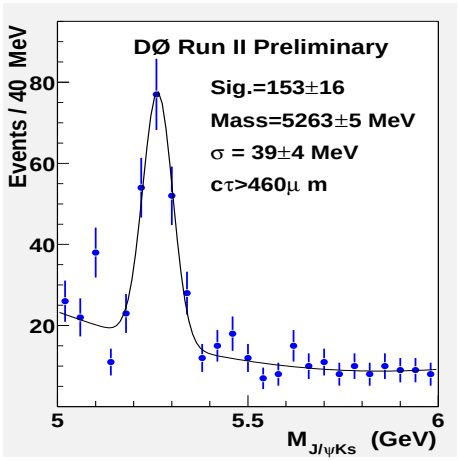

Figure 9.23: Invariant mass distribution of the $(J/\psi, K_S^0)$ system for all B_d^0 candidates plus the requirement $c\tau > 460$ μm. The signal is described by a Gaussian function and the background by a second order polynomial.

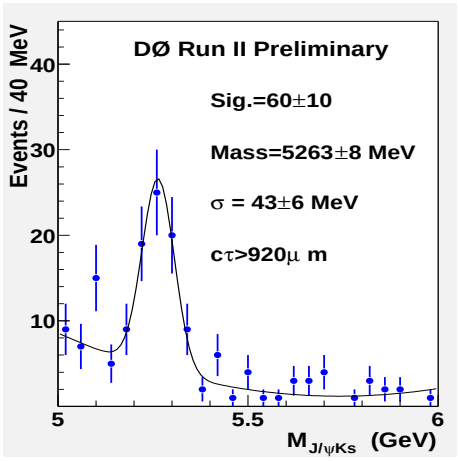

Figure 9.24: Invariant mass distribution of the $(J/\psi, K_S^0)$ system for all B_d^0 candidates plus the requirement $c\tau > 920$ μm. The signal is described by a Gaussian function and the background by a second order polynomial.

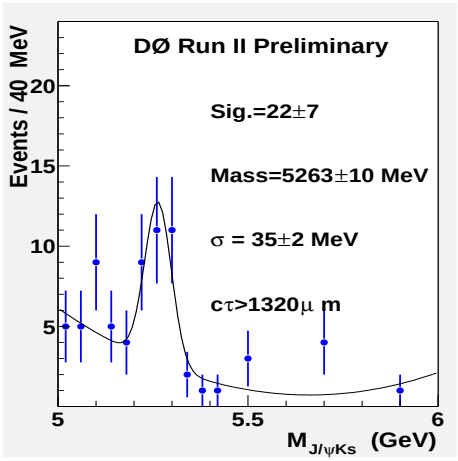

Figure 9.25: Invariant mass distribution of the $(J/\psi, K_S^0)$ system for all B_d^0 candidates plus the requirement $c\tau > 1320$ μm. The signal is described by a Gaussian function and the background by a second order polynomial.

Chapter 10

Λ_b^0 and B_d Lifetime Measurement

10.1 Proper Decay Length

We define the signed decay length of a Λ_b^0 baryon as the vector pointing from the primary vertex to the decay vertex projected on the Λ_b^0 momentum in the transverse plane:

$$L_{xy}^{\Lambda_b^0} = (\vec{x}_{\Lambda_b^0} - \vec{x}_{prim}) \cdot \vec{p}_T / p_T, \tag{10.1}$$

where $\vec{p}_T$ is the measured transverse momentum vector and p_T is its magnitude. The primary vertex is reconstructed individually for each event as described earlier.

The proper lifetime, τ, and the proper decay length, $c\tau$, are then defined by the relation:

$$c\tau = L_{xy}^{\Lambda_b^0} \cdot M_{\Lambda_b^0} / p_T, \tag{10.2}$$

where $M_{\Lambda_b^0} = 5624 \pm 9$ MeV is the world average mass of the Λ_b^0 baryon [29].

10.1.1 Proper Decay Time Distributions

We divide the Λ_b^0 mass range into three bands: "low side", $5.37 < M(\Lambda_b^0) < 5.5$ GeV; "middle", $5.5 < M(\Lambda_b^0) < 5.73$ GeV; and "high side", $5.73 < M(\Lambda_b^0) < 5.87$ GeV. The middle mass band includes the signal; all three contain comparable numbers of background events. The proper lifetime distributions in the three mass bands are compared in Fig. 10.1.

The distributions are normalized to the number of events in the signal region. The low and high sidebands are dominated by physics background, such as B meson background. We assume the same parametrization of the background shape in the entire mass region.

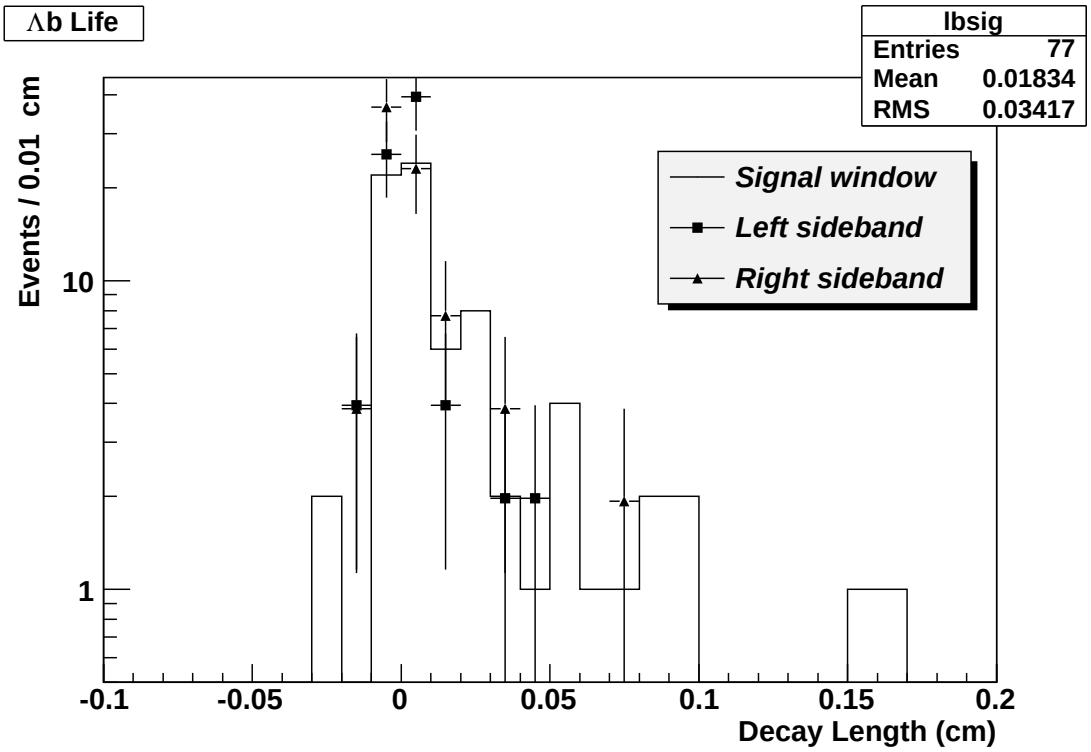

Figure 10.1: The proper lifetime distribution in three mass bands (see text).

10.2 Fitting Procedure for Λ_b^0

We use the MINUIT minimization program in root (TMinuit class). The source code and user tips are available at [71].

The proper decay length and invariant mass distribution of the Λ_b^0 candidates are fit

simultaneously using an unbinned maximum log-likelihood method. The likelihood function $\mathcal{L}$ is given by:

$$\mathcal{L} = \prod_{i=1}^{N}[f_{sig}\mathcal{F}_{sig}^{i} + (1 - f_{sig})\mathcal{F}_{bck}^{i}], \tag{10.3}$$

where N=353 is the total number of events, $\mathcal{F}_{sig}^{i}$ is the product of the signal mass and proper decay-length probability density functions, $\mathcal{F}_{bck}^{i}$ is the product of the background mass and proper decay-length probability density functions, and f_{sig} is the fraction of signal.

We use a range of 5.0 GeV $<$ M(Λ_b^0) $<$ 6.3 GeV for the Λ_b^0 mass window. Previously we implemented lifetime related cuts (collinearity and decay length related cuts), which were used to solidly establish the signal. However, for lifetime purposes we have to remove these cuts. We will use the signal with no lifetime cuts as shown in Fig 10.2. The cuts used for selecting these events are:

- vertex $\chi^2(\Lambda_b) < 12$;
- $p(\Lambda_b^0) > 5$ GeV;
- xy distance from J/ψ vertex to Λ vertex > 0.9 cm;
- $p_T(\Lambda) > 2.4$ GeV; and
- $\sigma(c\tau) < 100$ fs.

These are the events used to extract the lifetime. Figure 10.2 shows the invariant mass of $\mu^+\mu^-\Lambda$ subject to the above cuts. The signal is modeled with a Gaussian function, and the background by a constant plus a second order polynomial. The number of signal events extracted from the fit is 32 ± 10 with a mean of 5622 ± 12 MeV and a width of $\sigma = 36 \pm 10$ MeV.

The lifetime distribution of the signal is parameterized by an exponential convoluted with a Gaussian function. The lifetime resolution of background is approximated by a

Parameter	Central value ± error
Proper decay length, $c\tau$	$408 \pm 89\mu$**m**
Signal fraction, f_{sig}	0.091 ± 0.028
Mass of Λ_b, $M(\Lambda_b)$	5622±12 MeV
Width of Λ_b, $\sigma(\Lambda_b)$	36± 10 MeV
Mass Slope(0), a0	-0.31 ± 0.031
Mass Slope(1), a1	0.026 ± 0.028
Error scale factor, s	1.7 ± 0.1
$slope - bkg - neg$	88 ± 52 μm
$slope - bkg - pos$	423 ± 114 μm
$norm - bkg - neg$	0.02 ± 0.02
$norm - bkg - pos$	0.1 ± 0.02

Table 10.1: Unbinned maximum likelihood fitting results for the Λ_b^0 signal.

superposition of a Gaussian function centered at zero, one exponential for the negative $c\tau$ region and one exponential for the positive $c\tau$ region, with free slopes. The width of the Gaussian functions is taken from the event-by-event measurement of decay length error, σ_L. To allow for the possibility of the lifetime uncertainty to be systematically mis-estimated, we introduce a free scale factor s that multiplies the decay length error, i.e., $s \cdot \sigma_L$. The fraction of the signal is set to the central value obtained in the separate mass fit and allowed to vary within its statistical errors. This fraction is $f_{sig} = N_{signal}/N_{total}$ in the defined mass window.

Fit to the data

The fit results are summarized in Table 10.1.

The lifetime distribution with the fit results overlaid is shown in Fig. 10.3. In the figure, for illustration purposes, we assume a constant decay length resolution of 50 μm, which is the average value observed in the data.

In Fig. 10.4 we fit only the sidebands with the background functional form showing a

good fit as expected.

For the Λ_b^0 mean proper decay length we obtain:

$$c\tau(\Lambda_b^0) = 408 \pm 89 \text{ (stat) } \mu\text{m}. \tag{10.4}$$

The central value of Λ_b^0 mean proper decay length is larger than what has been reported previously [29] (367 ± 24 μm); however, it is consistent within statistical errors.

The fraction of signal in the sample is $f_{sig} = 0.091 \pm 0.028$. The fitted value of the lifetime resolution scale factor, $s = 1.7 \pm 0.1$, is inconsistent with unity which means that our errors in the data have been underestimated. This has been shown also in other lifetime analyses [36].

10.3 Fitting Procedure for B_d

We used the same fitting procedure for B_d as for Λ_b^0. The proper decay length and invariant mass distribution of the B_d candidates are fit simultaneously using an unbinned maximum log-likelihood method. The likelihood function $\mathcal{L}$ is given by:

$$\mathcal{L} = \prod_{i=1}^{N} [f_{sig}\mathcal{F}_{sig}^i + (1 - f_{sig})\mathcal{F}_{bck}^i], \tag{10.5}$$

where N=2409 is the total number of events, $\mathcal{F}_{sig}^i$ is the product of the signal mass and proper decay-length probability density functions, $\mathcal{F}_{bck}^i$ is the product of the background mass and proper decay-length probability density functions, and f_{sig} is the fraction of signal.

We use a range of 4.9 GeV $<$ M(B_d) $<$ 5.6 GeV for the B_d mass window. We will use the signal with no lifetime cuts as shown in Fig 10.5. The cuts used for selecting these events are:

- vertex $\chi^2(B_d) < 25$;

Parameter	Central value ± error
Proper decay length, $c\tau$	**428 ±35 μm**
Signal fraction, f_{sig}	0.135 ± 0.016
Mass of B_d, $M(B_d)$	5273 ± 6 MeV
Width of B_d, $\sigma(B_d)$	50 ± 6 MeV
Mass Slope (0), a0	-0.37 ± 0.003
Mass Slope (1), a1	0.034 ± 0.003
Error scale factor, s	1.56 ± 0.05
$slope - bkg - neg$	131 ± 19 μm
$slope - bkg - pos$	466 ± 35 μm
$norm - bkg - neg$	0.040 ± 0.008
$norm - bkg - pos$	0.18 ± 0.01

Table 10.2: Unbinned maximum likelihood fitting results for the B_d^0 signal.

- $p(B_d) > 5$ GeV;
- xy distance from J/ψ vertex to K_s vertex > 0.3 cm; and
- $p_T(K_S^0) > 1.8$ GeV.

These are the events used to extract the lifetime. Figure 10.5 shows the invariant mass of $(\mu^+\mu^-\Lambda^0)$ subject to the above cuts. The signal is modeled with a Gaussian function, and the background by a constant plus a second order polynomial. The number of signal events extracted from the fit is 330 ± 39 with a mean of 5622 ± 12 MeV and a width of $\sigma = 50 \pm 6$ MeV.

Signal and background are parametrized identically to Λ_b^0.

Fit to the data for B_d

The fit results are summarized in Table 10.2.

The lifetime distribution with the fit results overlaid is shown in Fig. 10.6. In the figure

for illustration purposes, we again assume a constant decay length resolution of 50 μm, which is the average value observed in the data.

For the B_d mean proper decay length we obtain:

$$c\tau(B_d) = 428 \pm 35 \text{ (stat) } \mu\text{m}. \tag{10.6}$$

The central value of B_d mean proper decay length is in a good agreement with previous measurements of this value [29] and the world average of $c\tau(B_d) = 460 \pm 4$ (stat) μm.

The fraction of signal in the sample is $f_{sig} = 0.135 \pm 0.016$. The fitted value of the lifetime resolution scale factor, $s = 1.56 \pm 0.05$, is consistent with that observed for the Λ_b^0 channel.

10.4 Systematic Errors for Λ_b and B_d Lifetime

We summarize the systematic errors for our measurements for Λ_b^0 and B_d lifetime in Table 10.3.

The contribution from the uncertainty in detector alignment is estimated by reconstructing the B^0 sample with the positions of the SMT sensors shifted outwards radially by the alignment error of 30 μm in the radial position of the sensors and then re-fitting for the lifetime.

To check the stability of the fits, we varied the fitted parameters other than $c\tau$ within $\pm\sigma$ of their nominal value, one at a time. This systematic turned out to be the dominant error for Λ_b^0 but, comparable with the other ones for B_d.

To estimate the uncertainity in the modeling, we used different background shapes to describe the background. We used one and two exponential PDF for the lifetime background. We also used an exponential and second order polynomial PDF for the mass.

We also fitted the background only separately and the fitted parameters from this fit are used as fixed parameters when we fit background plus signal. The difference in the results

Source	Λ_b (μ m)	B_d (μm)	Ratio
Alignment	5	5	0.016
Variation of Fitting Parameters	16	5	0.039
Modeling	11	3	0.026
Fixing the parameters from sideband fit	1	9	0.020
Total	**20**	**12**	**0.050**

Table 10.3: Summary of systematic uncertainties in the measurement of $c\tau$ for Λ_b^0 and B_d and their ratio. The total uncertainties are also given combining the individual uncertainties in quadrature.

between the lifetime we get when using fixed background and the unfixed background gives rise to only a small uncertainity.

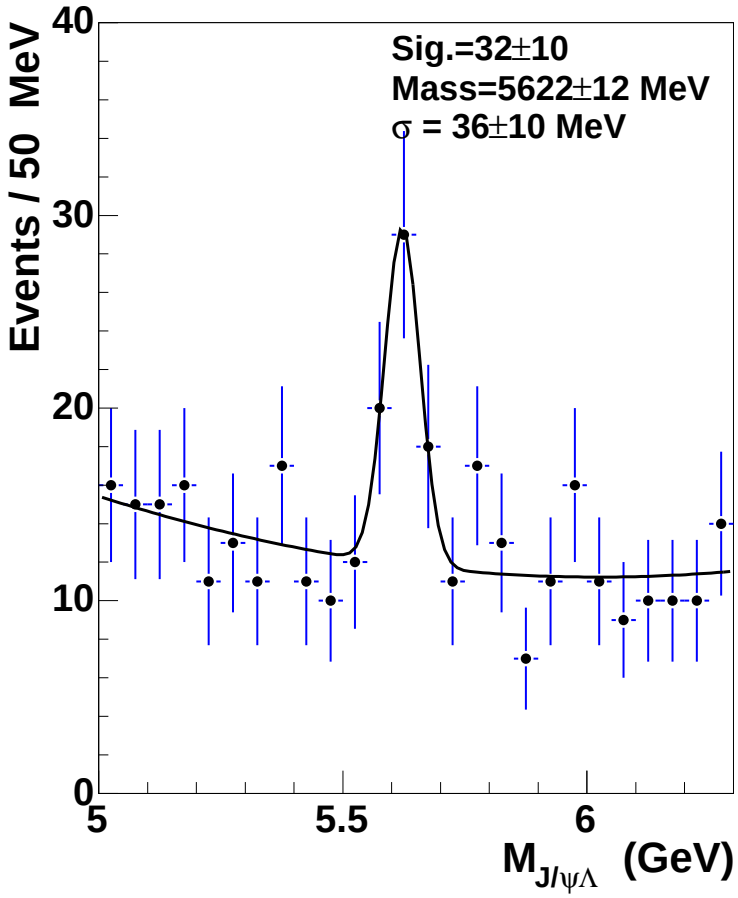

Figure 10.2: Invariant mass distribution of the $(J/\psi, \Lambda)$ system for all Λ_b^0 candidates without any lifetime cuts. The signal is described by a Gaussian function and the background by a second order polynomial.

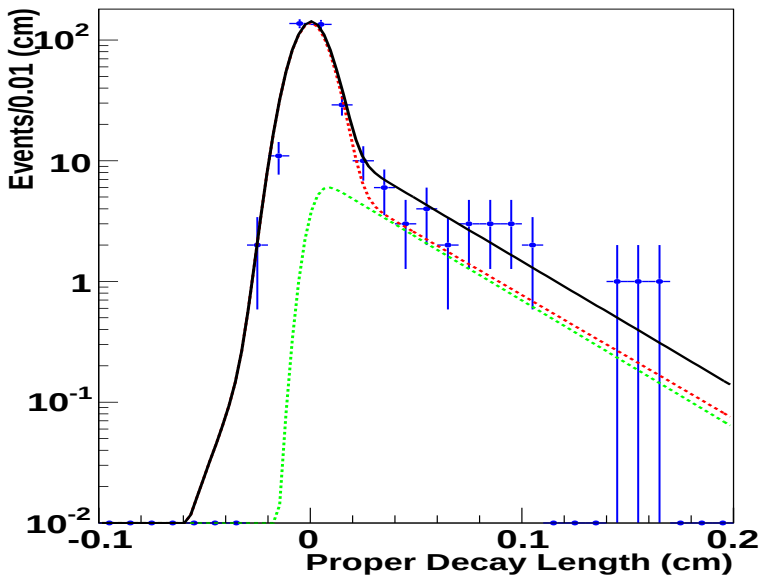

Figure 10.3: The proper decay length, $c\tau$, of the Λ_b^0 candidates. The curves show: the signal contribution, dotted (green); the background, dashed (red); and total, solid (black).

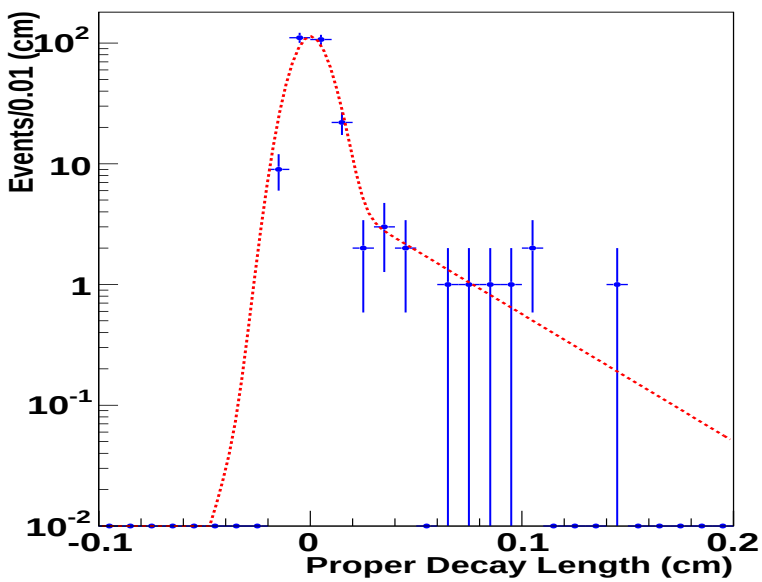

Figure 10.4: The proper decay length, $c\tau$, of the sidebands.

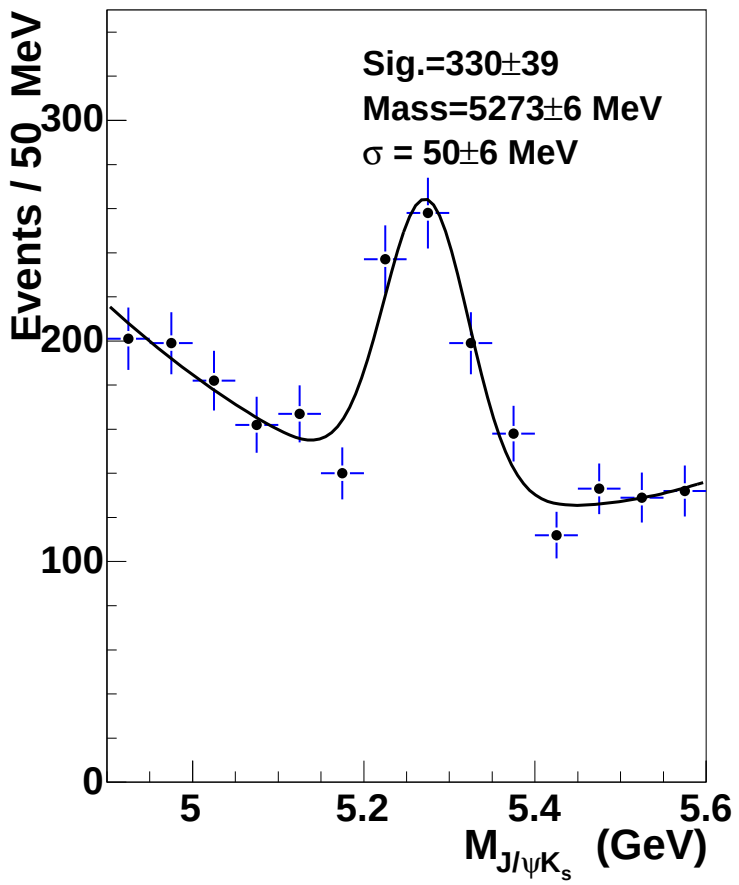

Figure 10.5: Invariant mass distribution of the $(J/\psi, K_S)$ system for all B_d candidates without lifetime cuts. The signal is described by a Gaussian function and the background by a second order polynomial.

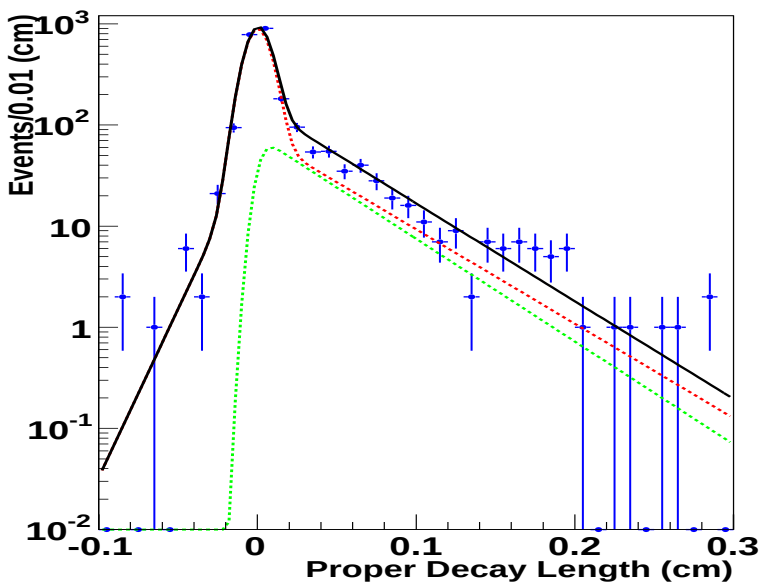

Figure 10.6: The proper decay length, $c\tau$, of the B_d candidates. The curves show: the signal contribution, dotted (green); the background, dashed (red); and total, solid (black).

Chapter 11

Discussion and Conclusion

11.1 Summary on Establishing the Λ_b^0 Signal

We observe evidence for the Λ_b^0 baryon using the exclusive decay $\Lambda_b^0 \to J/\psi\Lambda$ followed by $J/\psi \to \mu^+\mu^-$ and $\Lambda \to p\pi^-$. The data sample corresponds to an integrated luminosity of approximately 225 pb^{-1}. We find 48±10 Λ_b^0 candidates and determine the mass of Λ_b^0 baryon to be 5630 ± 10 (stat) MeV. This result is consistent with previous Λ_b^0 baryon mass measurements [29]. The Λ_b^0 yield following lifetime-related cuts also indicates that the signal contains a lifetime distribution different from background. The decay $B_d^0 \to J/\psi K_S^0$ is used as a test sample, so for completenness, we also show the results for B_d^0 meson. We find 300±39 B_d^0 candidates and determine the mass of the B_d^0 meson to be 5270 ± 5 (stat) MeV.

11.2 Summary of Preliminary Lifetimes

We were able to extract the lifetimes of $\Lambda_b^0 \to J/\psi\Lambda$ and $B_d^0 \to J/\psi K_S^0$. The lifetime of the Λ_b^0 baryon has been measured to be

$$c\tau(\Lambda_b^0) = 408 \pm 89 \text{ (stat)} \pm 20 \text{ (syst) } \mu\text{m}. \tag{11.1}$$

$$\tau(\Lambda_b^0) = 1.36 \pm 0.30 \text{ (stat)} \pm 0.07 \text{ (syst) ps}. \tag{11.2}$$

This result is consistent with the world average [29] of $\tau(\Lambda_b^0) = 1.229 \pm 0.080$ ps.

The lifetime of the B_d baryon has been measured for completeness:

$$c\tau(B_d) = 428 \pm 35 \text{ (stat)} \pm 12 \text{ (syst) } \mu\text{m}. \tag{11.3}$$

$$\tau(B_d) = 1.43 \pm 0.12 \text{ (stat)} \pm 0.04 \text{ (syst) ps}. \tag{11.4}$$

This result is in agreement with the world average [29] of $\tau(B_d) = 1.536 \pm 0.014$ ps. Finally we report the ratio $\tau(\Lambda_b)/\tau(B_d)$:

$$\frac{\tau(\Lambda_b)}{\tau(B_d)}|_{exp} = 0.95 \pm 0.22 \text{ (stat)} \pm 0.05 \text{ (syst)}, \tag{11.5}$$

which is consistent with previous world measurements and with the theoretical predictions. Although the data used in this study are limited we look forward to adding more data and should be able to carry out a competitive measurement of the Λ_b^0 lifetime via this exclusive decay channel.

Appendix A

Further Details on Systematics Error Determination

We will show here a case study for systematics: we assume the mixing parameters x and y are 5% and Im $\xi = 0$, and investigate Re ξ. We previously observed that MC corrections were very small in what we call the standard FOCUS absorption model. It includes $\bar{D}^0$ and D^0 cross sections half the pion cross section, Moliere scattering and the absorbed particles having no byproducts. While interactions of pions and kaons with matter have been measured, no such measurement exist for intereactions of charm particles with matter. We assumed that $\sigma(D^0) = \sigma(\bar{D}^0) = 1/2 \times \sigma(\pi)$ and even though this is a good assumption we want to examine the sensitivity of CPT parameters when cross sections are not equal. In Fig. A.1(a) several variations from standard absorption are shown. We observe that we are not very sensitive to the difference between the cross sections of $\bar{D}^0$ versus D^0. For instance, increasing the $\bar{D}^0$ cross section by 20% relative to D^0, results in a 4% decrease in Re ξ. In reality these cross sections should be closely equal which results in systematic effect of less than 1% associated with typical uncertainties in charm cross sections.

Fig. A.1(b) shows the stability of Re ξ versus split samples. Some momentum dependence is observed but the variations are not very significant.

We vary $\frac{L}{\sigma}$ and Kaonicity $(W_\pi - W_K)$ requirements. We observe in Fig.A.2(b) the fitted Reξ versus 16 combinations of $\frac{L}{\sigma}$ and $(W_\pi - W_K)$ for x and y mixing of 5%. We saw that the corrections remain small independent of the set of cuts we used. From the way these cuts are applied there is a correlation of the data from one set to the other one but the underlying systematic effect is small.

We also investigated bin and sideband variations to check for any systematic effect.

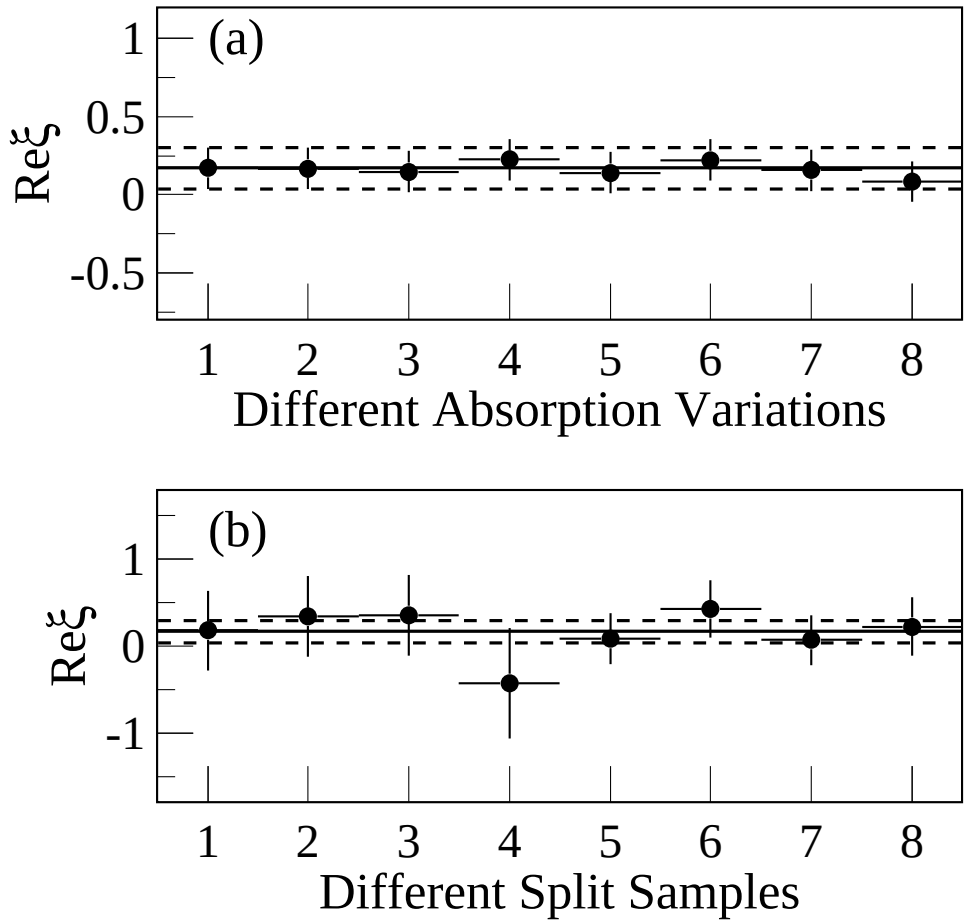

Figure A.1: Re ξ for different MC absorption models. The order of each point from left to right is 1) uncorrected 2) standard FOCUS (baseline): 3) baseline and byproducts 4) baseline and charm absorption zero 5) baseline, charm absorption zero and byproducts, 6) baseline, $\sigma(\bar{D}^0) = 1/2 \times \sigma(\pi^+) = 11.5mb$ and $\sigma(D^0) = 1/2 \times \sigma(\pi^-) = 13mb$, 7) baseline and $\sigma(D^0) = 3/2 \times \sigma(\bar{D}^0)$, 8) baseline and $\sigma(D^0) = 3 \times \sigma(\bar{D}^0)$ (a). Different split samples (b).

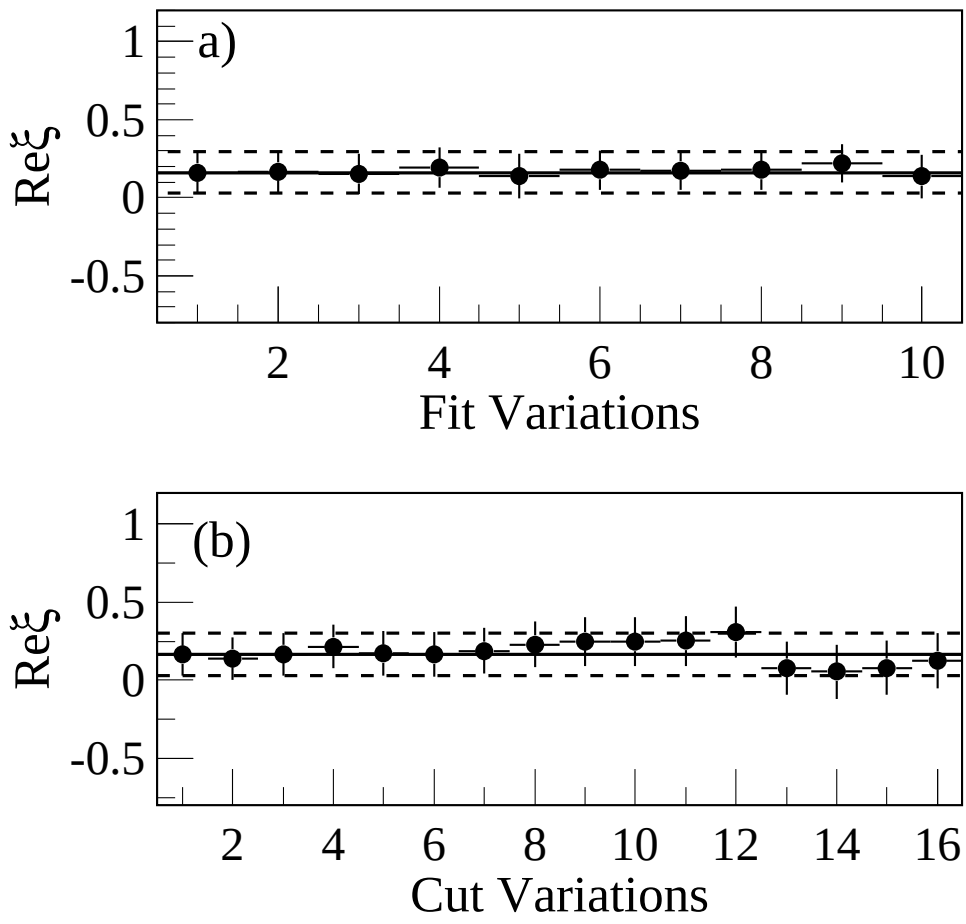

Figure A.2: Stability of $Re\xi$ for (a) different fit variants and (b) cut variants ($\frac{L}{\sigma}$,Kaonicity)

Fig.A.2(a) shows five different sideband methods and two different bin widths. The five different sidebands are ($\pm 2\sigma$,$\pm 3\sigma$,$\pm 7\sigma$), ($\pm 2\sigma$,$\pm 4\sigma$,$\pm 8\sigma$), ($\pm 2\sigma$,$\pm 3\sigma$,$\pm 9\sigma$), ($\pm 2\sigma$,3σ,7σ) and ($\pm 2\sigma$,-3σ,-7σ) and two bins are 500 fs and 300 fs. In Fig.A.2a), the first 5 points correspond to 500fs bin width and the last five points correspond to 300 fs bin width.

References

[1] S. Weinberg, *Phys. Rev. Lett.* **19**, 1264 (1967).

[2] *Atmospheric Neutrino Results From Super Kamiokande and Kamiokande; Evidence of Neutrino Oscillations.*, *Nucl. Phys. Proc. Suppl.* **77**, 123 (1999).

[3] Zoltan Kunszt, "Bread and Butter standard model", hep-ph/0004103.

[4] Ch. Quigg, *The Electroweak Theory*, hep-ph/0204104.

[5] V.A. Kostelecký, R. Potting, *Phys. Rev.* D **51**, 3923 (1995).

[6] V.A. Kostelecký, *Phys. Rev.* D **64**, 076001 (2001). *Section 2 of the paper gives relationships between formalisms.*

[7] V. A. Kostelecký, *CPT and Lorentz Symmetry II*; Singapore, World Scientific Publishing Co. Pte. Ltd. (2002).

[8] V.A. Kostelecký, *Phys. Rev.* D **61**, 016002 (1999).

[9] Y.B. Hsiung for the KTeV Collaboration, Proc. QCD Euroconference 99, Montpellier, France, July 7-13, 1999. Also available as FERMILAB-Conf-99/338-E (KTeV).

[10] H. Nguyen, *CPT results from KTeV*, hep-ex/0112046.

[11] OPAL Collaboration (K. Ackerstaff *et al.*), *Z. Phys.* C **76**, 401 (1997).

[12] Belle Collaboration (K. Abe, *et al.*), *Phys. Rev. Lett.* **86**, 3228 (2001).

[13] FOCUS Collaboration (J. Link *et al.*), *Phys. Lett.* B **485**, 62 (2000).

[14] Belle Collaboration (K. Abe *et al.*), *Phys. Rev. Lett.* **88**, 162001 (2002).

[15] BaBar Collaboration (B. Aubert *et al.*), *Search for a Lifetime Difference in D^0 Decays*, hep-ex/0109008.

[16] CLEO Collaboration (R. Godang *et al.*), *Phys. Rev. Lett.* **84**, 5038 (2000).

[17] FOCUS Collaboration (J. Link *et al.*), *Phys. Rev. Lett.* **86**, 2955 (2001).

[18] FOCUS Collaboration (J. Link *et al.*), *Phys. Lett.* B **556**, 7 (2003).

[19] D. Colladay and V.A. Kostelecký, *Phys. Rev.* D **55**, 67600 (1997); *Phys. Rev.* D **58**, 116002 (1998); V.A. Kostelecký, *Phys. Rev.* D **69**, 105009 (2004).

[20] V.A. Kostelecký, *Phys. Rev. Lett.* **80**, 1818 (1998).

[21] Jean Meeus, Astronomical Algorithms First English Edition (1991).

[22] E687 Collaboration (P.L.Frabetti *et al*), *Nucl. Inst. and Meth.* A **320**, 519 (1992).

[23] P. Kasper, R. Currier, P. Garbincius, and J. Butler, Wide band to double band upgrade. Technical Report TM-1552, Fermilab, 1988.

[24] FOCUS Collaboration (J. M. Link *et al.*), *Nucl. Inst. and Meth.* A **484**, 174 (2002).

[25] E. Vaandering, Ph.D. thesis, University of Colorado, Boulder, January 2000.

[26] J. M. Link, Ph.D. thesis, University of California, Davis, March 2001.

[27] J. M. Link *et al.*, *Nucl. Inst. and Meth.* A **516**, 364 (2004).

[28] FOCUS Collaboration (J. M. Link *et al.*), *Nucl. Inst. and Meth.* A **484**, 270 (2002).

[29] Review of Particle Properties, S. Eidelman *et al.*, *Phys. Lett.* B **592**, 1 (2004).

[30] E687 Collaboration (P.L. Frabetti *et al.*), *Phys. Lett.* B **370**, 222 (1996).

[31] T. Sjöstrand *et al.*, *Comput. Phys. Commun.* **135**, 238 (2001).

[32] C. Albajar *et al.*, *Phys. Rev.* D **273**, 540 (1991).

[33] ALEPH Collaboration (D. Buskulic *et al.*), *Phys. Lett.* B **380**, 442 (1996).

[34] DELPHI Collaboration (P. Abreu *et al.*), *Phys. Lett.* B **374**, 351 (1996).

[35] CDF Collaboration (F. Abe *et al.*), *Phys. Rev.* D **55**, 1142 (1997).

[36] DØ Collaboration (V .M. Abazov *et al.*), *Measurement of* Λ_b^0 *lifetime in the decay* $\Lambda_b^0 \to J/\psi\Lambda$ *with DØ detector*, hep-ex/0410054. Submitted to *Phys. Rev. Lett.*.

[37] G. Kane, Modern Elementary Particle Physics, Addision-Wesley, 1993

[38] S. Eidelman *et al.*, *Phys. Lett.* B **592**, 1 (2004); E. Barberio, presented at the Workshop on the CKM Unitary Triangle, http://ckm-workshop.web.cern.ch; M. Battaglia *et al.*, hep-ph/0304132.

[39] LEP B Lifetime Working Group, http://lepbosc.web.cern.ch/LEPBOSC/lifetimes/lepblife.html.

[40] M. Ciuchini, E. Franco, V. Lubicz and F. Mescia, *Nucl. Phys.* B **625**, 211 (2002); E. Franco, V. Lubicz, F. Mescia and C. Tarantino, *Nucl. Phys.* B **633**, 212 (2002).

[41] F. Gabbiani, A. I. Onishchencko and A. A. Petrov, *Phys. Rev.* D **68**, 114006 (2003)

[42] F. Gabbiani, A. I. Onishchencko and A. A. Petrov, *Spectator Effects and Lifetimes of Heavy Hadrons*, hep-ph/0407004.

[43] C. Tarantino, *Eur. Phys. J.* C **33**, 895 (2004).

[44] I. Bigi *et al.*, hep-ph/0001003, hep-ph/9401298; M. B. Voloshin, hep-ph/0004257.

[45] M. B. Voloshin, Phys. Rep. **320**, 275 (1999); B. Guberina, B. Melic, and H. Stefancic, *Phys. Lett.* B **469**, 253 (1999); M. Neubert and C. T. Sachrajda, *Nucl. Phys.* B **483**, 339 (1997).

[46] M. A. Shifman and M. B. Voloshin, *Sov. J. Nucl. Phys.* **41**, 120 (1985).

[47] B. Guberina *et al.*, *Phys. Lett.* B **89**, 111 (1979); N. Bilic *et al.*, *Nucl. Phys.* B **248**, 261 (1984); B. Guberina *et al.*, *Z. Phys.* C **33**, 297 (1986).

[48] T. LeCompte, H. T. Diehl, "The CDF and DØ Upgrades for Run II"; Fermilab Annual Review (2000).

[49] S. D. Holmes, *Part. Accel.* **58**, 39 (1997), Fermilab-Conf-97/038.

[50] G. P. Jackson, "The Fermilab Recycler Ring Technical Design Report", Fermilab-TM-1991 (1996).

[51] DØ Collaboration (S. Abachi *et al.*), "The DØ Upgrade: Detector and its Physics", Fermilab-Pub-96/357-E (1996); "The DØ Upgrade Forward Preshower, Muon System, and Level 2 Trigger", Fermilab-FN-639 (1996).

[52] DØ Collaboration (S. Abachi *et al.*), *Nucl. Instr. Methods Phys. Res.* A **338**, 185 (1994).

[53] R. Lipton for the DØ Collaboration, *Nucl. Instr. Methods* A **418**, 85 (1998).

[54] R. Yarema *et al.*, "A beginners Guide to the SVX II Chip", Fermilab-TM-1892 (1994).

[55] M. Wayne for the DØ Collaboration, *Nucl. Instr. Methods* A **408**, 103 (1998).

[56] T. Zimmermann *et al.*, *Nucl. Instr. Methods Phys. Res.* A **409**, 1 (1998).

[57] B. S. Acharya *et al*, *Nucl. Instr. Methods* A **401**, 45 (1997).

[58] V. Abramov *it* al., *Nucl. Instr. Methods* A **419**, 660 (1998).

[59] O. Eroshin, D. Denisov, "Status of forward muon reconstruction program", DØ Note 3714 (1999).

[60] DØ Collaboration "The DØ Upgrade", DØ internal technical documentation (1995).

[61] `http://d0server1.fnal.gov/users/nomerot/Run2A/BANA/Dskim.html.`

[62] DELPHI Collaboration (J. Abdallah *et al.*), *Eur. Phys. J.* C **32**, 184 (2004).

[63] `http://d0server1.fnal.gov/users/nomerot/Run2A/BANA.html` .

[64] A. Ryd, D. Lange, http://www.slac.stanford.edu/∼lange/EvtGen/ .

[65] H. U. Bengtsson and T. Sjostrand, *Comput. Phys. Commun.* **46**, 43 (1987).

[66] `http://www-d0.fnal.gov/computing/MonteCarlo/generator_tools/d0_mess.html`.

[67] `http://wwwasdoc.web.cern.ch/wwwasdoc/pdfdir/geant.pdf`.

[68] Abaz Kryemadhi, Rick Van Kooten, *A Measurement of the* Λ_b^0 *Baryon Lifetime Using the* $\Lambda_b^0 \to J/\psi\Lambda$ *Decay Mode*, DØ Note 4232, 15 Aug. 2003.

[69] Abaz Kryemadhi, Rick Van Kooten, *(Re)Establishing the* Λ_b^0 *signal via the* $\Lambda_b^0 \to J/\psi\Lambda$ *Decay Mode*, DØ Note 4355, 23 Feb. 2004.

[70] Daria Zieminska, *Do We Understand the* Λ_b *Signal?*, DØ Note 4269, 1 Oct. 2003.

[71] Chunhui Luo, Ph.D. thesis, Indiana University, Bloomington, July 2003.

Curriculum Vitae

Personal

Name:	Abaz Kryemadhi
Date of birth	March 31, 1973
Citizenship	Albanian

Education

1998-2004	**Ph.D.**, Indiana University, Bloomington, IN
1998-1999	**M.Sc.** Indiana University, Bloomington, IN
1996-1998	**Diplom Physik.** Siegen University, Siegen, Germany
1991-1996	**B.Sc.** University of Tirana, Tirana, Albania

Research Experience

Indiana University, DØ, FNAL	Measuring the Lifetime of Λ_b^0 baryon
Indiana University, E831, FNAL	Tests of CPT in charm mesons

Work Experience

1999-2004	Research Assistant – Department of Physics, Indiana University
1998-1999	Teaching Assistant – Department of Physics, Indiana University

Honors

1997	Heinrich Hertz Foundation Fellowship